

# Warming does not delay the start of autumnal leaf coloration but slows its progress rate

Nan Jiang

<https://orcid.org/0000-0001-5151-5715>

Miaogen Shen (✉ [shen.miaogen@gmail.com](mailto:shen.miaogen@gmail.com))

Philippe Ciais

Matteo Campioli

Josep Peñuelas

Christian Körner

Ruyin Cao

Shilong Piao

Licong Liu

Shiping Wang

Eryuan Liang

Nicolas Delpierre

Kamel Soudani

Yuhan Rao

Leonardo Montagnani

Lukas Hörtnagl

Eugénie Paul-Limoges

Ranga Myneni

Georg Wohlfahrt

Yongshuo Fu

Ladislav Šigut

Andrej Varlagin

Jin Chen

Yanhong Tang

Wenwu Zhao

---

## Research Article

**Keywords:** autumnal leaf senescence, global warming, leaf coloration onset, Northern Hemisphere, photoperiod

**Posted Date:** February 15th, 2022

**DOI:** <https://doi.org/10.21203/rs.3.rs-1352963/v1>

**License:**  This work is licensed under a Creative Commons Attribution 4.0 International License.

[Read Full License](#)

---

1   **Warming does not delay the start of autumnal leaf coloration but slows its progress rate**

2

3   **ABSTRACT**

4   **Aim:** Initiation of autumnal leaf senescence is critical for plant overwintering and ecosystem  
5   dynamics. Previous studies focused solely on the advanced stages of autumnal leaf senescence  
6   and claimed that climatic warming delays senescence, despite the fundamental differences  
7   among the stages of senescence. However, the timing of onset of leaf coloration ( $D_{LCO}$ ), the  
8   earliest visual sign of senescence, has been rarely studied. Our aim is to assess the response of  
9    $D_{LCO}$  to temperature across the Northern Hemisphere.

10   **Location:** 30–75°N in the Northern Hemisphere.

11   **Time period:** 2000–2018.

12   **Major taxa studied:** Deciduous vegetation.

13   **Methods:** We retrieved  $D_{LCO}$  from high temporal-resolution satellite data, which was then  
14   validated by PhenoCam observations. We then investigated the temporal changes in  $D_{LCO}$  and  
15   the relationship between  $D_{LCO}$  and temperature by using  $D_{LCO}$  from satellite data and ground  
16   phenological observations. We further estimated the timing of onset of autumnal decline in  
17   maximum canopy photosynthetic capacity, an indicator of leaf senescence earlier than  $D_{LCO}$ ,  
18   from FLUXNET CO<sub>2</sub> fluxes data, and assessed its response to temperature.

19   **Results:**  $D_{LCO}$  was not significantly ( $P < 0.05$ ) delayed between 2000 and 2018 in 94% of the  
20   area.  $D_{LCO}$  was positively correlated with pre- $D_{LCO}$  mean daily minimum temperature ( $T_{min}$ ) in  
21   only 9% of the area, likely because of the overriding photoperiodic control, particularly for  
22   woody vegetation, whereas the end of leaf coloration ( $D_{LCE}$ ) was positively correlated with  
23   pre- $D_{LCE}$  mean  $T_{min}$  over a larger area (34%).

24   **Main conclusions:** The coloration progress rate is more sensitive than its start date to  
25   temperature, indicating an extension of the duration of leaf senescence under warming. This  
26   study indicates that the leaf coloration onset was not responsive to climate warming and  
27   provides observational evidence of photoperiod control of autumnal leaf senescence at biome  
28   and continental scales.

29

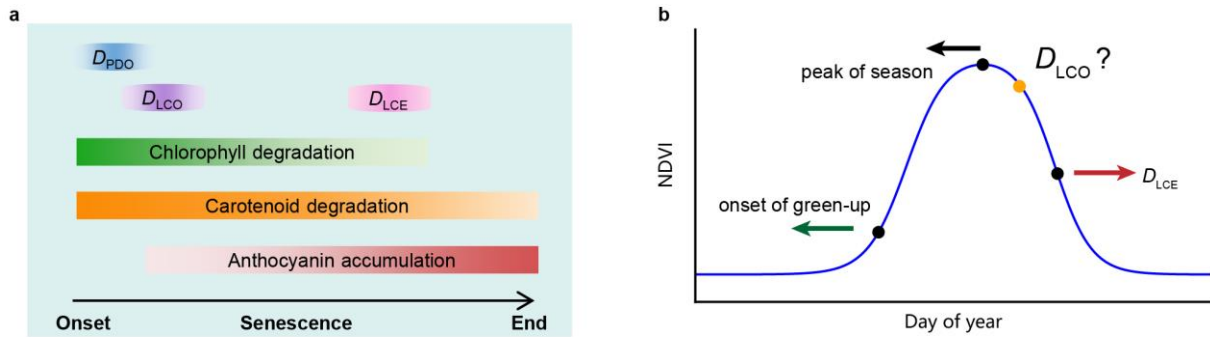
30   **Keywords:** autumnal leaf senescence, global warming, leaf coloration onset, Northern  
31   Hemisphere, photoperiod

32

33   **1 | INTRODUCTION**

34       In contrast to the leaves of evergreen conifers, those of northern deciduous plants are not  
35   sufficiently tolerant of freezing to survive cold periods and, therefore, are shed before the onset  
36   of winter. This autumnal senescence process is controlled by changes in gene expression and  
37   metabolic adjustments that include the degradation of macromolecules (e.g., chlorophyll), a  
38   decrease in photosynthesis, and, importantly, the recycling and reallocation of nutrients (Thomas  
39   & Stoddart, 1980; Gan & Amasino, 1997). Without timely leaf senescence and abscission, early  
40   frost would lead to a loss of leaf resources. In parallel to leaf senescence, carbon sink activity  
41   ceases progressively, and plants switch to nutrient recovery and resorption processes (Keskitalo  
42   *et al.*, 2005; Estiarte & Peñuelas, 2015). Changes in the timing of key steps of leaf senescence  
43   extensively influence ecosystem structure and functions, and this could further affect the climate  
44   system (Peñuelas *et al.*, 2009; Richardson *et al.*, 2013). Senescence starts as a cryptic  
45   phenological process before any visible symptoms become apparent (Körner & Basler, 2010).  
46   The timing of the start of the leaf coloration following senescence varies, depending on the rate  
47   of the senescence process, which is related to environmental conditions (e.g., temperature)  
48   (Fracheboud *et al.*, 2009). Hence, the process of autumnal leaf senescence has two phases (Fig.  
49   1a): (1) a visually indistinguishable ontogenetic stage that precedes (2) a visible change in leaf  
50   color (Tang *et al.*, 2016). The timing of leaf coloration is the focus of *in situ* phenological  
51   observations and has been the main concern of most autumnal phenological studies to date.

52



53

54 **Fig. 1** Conceptual graphs illustrating (a) the developmental processes in pigments during leaf  
 55 senescence that are related to photosynthetic capacity and leaf color; and (b) phenological  
 56 changes retrieved from normalized difference vegetation index (NDVI) data in the last few  
 57 decades. In (a),  $D_{\text{PDO}}$  and  $D_{\text{LCO}}$  are the timings of the onsets of the decrease in maximum canopy  
 58 photosynthetic capacity and leaf coloration in autumn, respectively;  $D_{\text{LCE}}$  is the timing of the  
 59 end of leaf coloration. In (b) the onset of green-up corresponds to a 20% increase in NDVI, the  
 60 peak of the season corresponds to the maximum NDVI, and  $D_{\text{LCO}}$  and  $D_{\text{LCE}}$  correspond to 10%  
 61 and 50% decreases, respectively, in NDVI. The leftward and rightward arrows indicate advance  
 62 of onset of green-up and peak of season and delay of  $D_{\text{LCE}}$  over the past few decades. The  
 63 question mark indicates a research gap regarding temporal changes in  $D_{\text{LCO}}$  and their drivers.

64

65 Satellite and ground-based observations indicate that climate warming in the last several  
 66 decades has substantially advanced the onset of spring green-up and the peak of the growing  
 67 season, and it has slightly delayed the timing of the end of leaf coloration ( $D_{\text{LCE}}$ , the time when  
 68 the normalized difference vegetation index [NDVI] decreases by 50% of its annual amplitude in  
 69 the second half of a year in satellite-based studies (White *et al.*, 1997; Ganguly *et al.*, 2010;  
 70 Nagai *et al.*, 2010; Yu *et al.*, 2010; Melaas *et al.*, 2013; Lukasová *et al.*, 2019)) in the Northern  
 71 Hemisphere (Fig. 1b) (Jeganathan *et al.*, 2014; Fu *et al.*, 2015; Gill *et al.*, 2015; Xu *et al.*, 2016;  
 72 Piao *et al.*, 2019; Menzel *et al.*, 2020). In addition to temperature, an increase in precipitation  
 73 also delays  $D_{\text{LCE}}$  in temperate dry grasslands in the northern middle latitudes (Liu *et al.*, 2016).  
 74 Besides these abiotic factors, temporal changes in  $D_{\text{LCE}}$  are also associated with the onset of  
 75 green-up in some temperate tree species (Keenan & Richardson, 2015) and in boreal ecosystems

76 (Liu *et al.*, 2016). In contrast to  $D_{LCE}$ , the timing of onset of leaf coloration ( $D_{LCO}$ ) has been  
77 inadequately studied (Fig. 1b). In particular, it is not known whether  $D_{LCO}$  is sensitive to climate  
78 and whether it has been responsive to recent climate change.  $D_{LCO}$  is of key importance because  
79 it indicates when leaf senescence becomes apparent and its progress accelerates (Fig. 1b). As  
80 shown by experiments on young trees, some temperate and boreal woody species use the  
81 shortening of the photoperiod as a signal for the onset of leaf senescence (Table S1), but many  
82 *in situ* and satellite observations indicate that increased temperature induces delays in the  
83 advanced stages of senescence such as  $D_{LCE}$  (Estrella & Menzel, 2006; Delpierre *et al.*, 2009;  
84 Jeong *et al.*, 2011; Ge *et al.*, 2015; Gill *et al.*, 2015; Liu *et al.*, 2016).

85 The dominant photoperiodic control of early senescence implies that  $D_{LCO}$  should not be  
86 delayed, even if the temperature increases, because its timing is controlled only by daylength  
87 (Hypothesis 1). On the other hand, without photoperiodic control, shifts in  $D_{LCO}$  are expected in  
88 the case of climatic warming (Hypothesis 2). Alternatively, if  $D_{LCO}$  is influenced by both  
89 photoperiod and temperature, the relationships between  $D_{LCO}$  and temperature should vary  
90 among different areas because the strength of the photoperiod signal varies (Hypothesis 3). We  
91 tested these hypotheses by investigating temporal changes in  $D_{LCO}$  and the interannual  
92 relationships between  $D_{LCO}$  and pre- $D_{LCO}$   $T_{min}$  (the mean of monthly average daily minimum  
93 temperature for an optimized period preceding  $D_{LCO}$ ) for northern vegetation (30°N–75°N,  
94 cropland pixels excluded) during the period 2000–2018. Since only a few *in situ* observational  
95 programs or networks have monitored  $D_{LCO}$ , we determined  $D_{LCO}$  from a 5-day composite time  
96 series of the NDVI derived from daily surface spectral reflectance (MOD09CMG) at a spatial  
97 resolution of 0.05°, provided by the spaceborne Moderate Resolution Imaging  
98 Spectroradiometer (MODIS) (Vermote, 2015). We defined  $D_{LCO}$  as the first date when daily  
99 NDVI, fitted from 5-day NDVI, decreased by 10% of its annual amplitude during the  
100 descending period of each year (Fig. 1b). To complement the NDVI data, we also used 332 time  
101 series of  $D_{LCO}$  observed by professional observers according to standard observation guidelines  
102 (China Meteorological Administration, 1993) in the field in China (Fig. S1a; Table S2) and the  
103 timing of onset of autumnal decline in maximum canopy photosynthetic capacity ( $D_{PDO}$ ) derived  
104 from eddy covariance CO<sub>2</sub> flux observations (Gu *et al.*, 2009; Shen *et al.*, 2014) at 36 sites from

105 in the FLUXNET2015 dataset (Pastorello *et al.*, 2017) (Fig. S1b and Table S3).

## 106 **2 | MATERIALS AND METHODS**

### 107 **2.1 | $D_{LCO}$ estimated from satellite observations of NDVI time series**

108       The NDVI is a proxy for vegetation greenness and has been widely used for phenological  
109 studies at large spatial scales (Myneni *et al.*, 1997). NDVI has also been proved capable of  
110 detecting the onset of leaf coloration (Soudani *et al.*, 2012; Yang *et al.*, 2014; Mariën *et al.*, 2019;  
111 Soudani *et al.*, 2020; Zhao *et al.*, 2020). Previous studies have usually used half-month/16-day  
112 composite NDVI time series to retrieve phenological metrics. However, because the color of  
113 leaves often changes abruptly (Wang & Zhu, 2019), NDVI time-series data with higher temporal  
114 resolution are required. We estimated phenological metrics (i.e., the timing of the onset and the  
115 advanced stages of leaf coloration and the onset of green-up) for 2000–2018 from a 5-day  
116 composite NDVI time series produced from the MODIS reflectance product (MOD09CMG  
117 Collection 6, available at <https://ladsweb.modaps.eosdis.nasa.gov>, accessed on 29 January 2019)  
118 (Vermote, 2015). MOD09CMG provides an estimate of daily surface spectral reflectance at a  
119 spatial resolution of 0.05°. The quality of the daily surface reflectance data from MOD09CMG  
120 is unsatisfactory owing to cloud and snow contamination (Vermote, 2015), so we used the 5-day  
121 maximum value composite approach (Zhang, 2015), combined with a Savitzky-Golay filter  
122 (Cao *et al.*, 2018), to produce a high-quality NDVI time series before determining  $D_{LCO}$ . First,  
123 NDVI values that were lower than the uncontaminated winter (December–February) mean  
124 NDVI were replaced by the latter (Beck *et al.*, 2006; Zhang *et al.*, 2007). After that,  
125 cloud-contaminated and irregularly high and low NDVI values were identified and reconstructed  
126 by using a Savitzky-Golay filter (Cao *et al.*, 2018). Details for preparing the high-quality NDVI  
127 time series are given in Section 1 of the Supplementary Methods.

128       We focused on natural vegetation by excluding pixels dominated by cropland, artificial  
129 surfaces, permanent snow or ice, and water bodies on the basis of the MODIS land-cover map  
130 for the middle year of the time series (2009) (MCD12C1 Version 6) (Friedl & Sulla-Menashe,  
131 2015) <https://ladsweb.modaps.eosdis.nasa.gov>, accessed on 20 August 2018). Some pixels were  
132 also excluded from analysis because of sparse vegetation coverage, weak seasonality, or NDVI

133 peaking in October–April. We adopted three criteria for pixel exclusion: mean annual NDVI  
134 must be  $> 0.10$ , NDVI should peak between May and September in the multiyear mean NDVI  
135 time series, and a pixel should be discarded if the mean NDVI for July and August is  $< 1.15$   
136 times the mean NDVI for December or for January–February in any year.

137 Two types of method can generally be used to estimate the parameters of vegetation  
138 phenology (Chen *et al.*, 2016), including  $D_{LCO}$  from annual NDVI profiles. One is based on  
139 thresholds (White *et al.*, 1997), whereas the other is based on inflection points (Zhang *et al.*,  
140 2003). We applied the threshold-based method by first using a generalized sigmoid function to  
141 fit the NDVI annual profile [Equation (7) in Klosterman *et al.* (2014)] and then determined  $D_{LCO}$   
142 as the first date when NDVI decreased by 10% of its annual amplitude in the descending period  
143 (Leblans *et al.*, 2017; Richardson *et al.*, 2018). Though a smaller decrease in NDVI corresponds  
144 to an earlier stage of leaf coloration, consideration of it would introduce more uncertainty. The  
145 advanced stages of leaf coloration were determined as the dates when NDVI decreases by 20%,  
146 30%, 40%, and 50% (corresponding to the timing of the end of leaf coloration,  $D_{LCE}$ ),  
147 respectively. We defined the timing of the onset of green-up as the date when NDVI increased  
148 by 20% (Yu *et al.*, 2010). We also determined  $D_{LCO}$  by using the algorithm based on inflection  
149 points owing to the slight difference between the methods for detecting phenological parameters.  
150 We defined  $D_{LCO}$  as the date when the rate of change of the curvature of a double logistic  
151 function (Beck *et al.*, 2006; Elmore *et al.*, 2012) fitted to the NDVI time series reached its first  
152 local minimum in the descending period (Zhang *et al.*, 2003).

153 It is unreasonable to validate the satellite derived  $D_{LCO}$  by comparing it with  $D_{LCO}$  of a few  
154 plant individuals from ground observation because of mismatch in spatial coverage, different  
155 definitions of phenological metrics, and the spatial heterogeneity in phenological phases among  
156 individuals for a pixel. Fortunately, pairs of field observations of NDVI and leaf coloration  
157 showed well consistency between the start of NDVI decrease and leaf coloration onset (Soudani  
158 *et al.*, 2012; Soudani *et al.*, 2020). Moreover, the comparison between start of autumn from  
159 satellite observed NDVI and field observations of leaf coloration onset for the entire area  
160 covered by the pixel also showed little difference between them (Zhao *et al.*, 2020). Those

161 studies suggest that NDVI is capable to detect the onset of leaf coloration if the observed leaves  
162 or individuals are identical between ground and satellite observations. However, there are very  
163 limited pairs of compatible observations of NDVI and leaf coloration that can be used for the  
164 validation. Considering the high capability of PhenoCam in capturing the variations in leaf  
165 coloration onset (Klosterman *et al.*, 2014; Wingate *et al.*, 2015; Klosterman & Richardson, 2017;  
166 Nezval *et al.*, 2020), we used the PhenoCam Dataset V2.0 (Richardson *et al.*, 2018;  
167 Seyednasrollah *et al.*, 2019a; Seyednasrollah *et al.*, 2019b) to assess the relationships between  
168 satellite  $D_{LCO}$  and the  $D_{LCO}$  derived from GCC (green chromatic coordinate) and VCI  
169 (vegetation contrast index) observed by PhenoCam (Section 2 of the Supplementary Methods).

## 170 **2.2 | $D_{LCO}$ from *in situ* phenological observations**

171  $D_{LCO}$  was extracted at the species level from datasets of *in situ* phenological observations  
172 in China provided by the Chinese Academy of Sciences (CAS). The CAS dataset uses the date  
173 of first leaf coloring as  $D_{LCO}$ . For a given species at a given site, the date of first leaf coloring  
174 was identified as the day when the first batch (about 5%) of leaves on more than half of three to  
175 five marked individuals started to change color (China Meteorological Administration, 1993).  
176 The *in situ* phenological observations were performed according to standard observation  
177 guidelines (China Meteorological Administration, 1993) every other day by professional  
178 observers trained well by CAS. The CAS dataset is available from National Earth System  
179 Science Data Sharing Infrastructure, National Science and Technology Infrastructure of China  
180 (<http://www.geodata.cn>, accessed on 25 July 2018).

## 181 **2.3 | $D_{PDO}$ estimated from maximum canopy photosynthetic capacity**

182 The timing of the onset of the decrease in maximum canopy photosynthetic capacity in  
183 autumn (in day of year,  $D_{PDO}$ ) is defined as the date when the capacity decreases by 10% of its  
184 annual amplitude after the data have been fitted to a generalized sigmoid function [Equation (7)  
185 in Klosterman et al.(2014)]. The capacity was calculated from half-hourly or hourly gross  
186 primary productivity (GPP\_NT\_CUT\_MEAN) based on eddy covariance measurements in the  
187 FLUXNET2015 dataset (<http://fluxnet.fluxdata.org/data/fluxnet2015-dataset/>, accessed on 10  
188 March 2018) (Pastorello *et al.*, 2017). We followed the procedure of Shen et al.(2014) to

189 estimate daily canopy photosynthetic capacity, except that the parameters in the rectangular  
190 hyperbolic function were estimated by using half-hourly/hourly GPP and incident shortwave  
191 radiation calculated by using 15-day moving windows throughout a year. We used data from the  
192 sites in non-Mediterranean (Köppen-Geiger climate classification) and non-cultivated  
193 (International Geosphere–Biosphere Programme classification) regions at middle and high  
194 northern latitudes ( $30^{\circ}\text{N}$ – $75^{\circ}\text{N}$ ). In a similar way to the pixel exclusion process that was applied  
195 to the satellite retrievals, we discarded sites where weak seasonality (i.e., the mean maximum  
196 canopy photosynthesis for June–August was  $<1.15$  times that for December or for January and  
197 February) was detected in any year and sites where capacity did not peak in May–September.

198 **2.4 | Cold events before  $D_{\text{LCO}}$  (or  $D_{\text{PDO}}$ )**

199 A sudden drop of nighttime temperature to the freezing point can induce leaf coloration in  
200 a few days (Körner, 2007), and this could have interfered with our partial correlation analysis  
201 between  $D_{\text{LCO}}$  (or  $D_{\text{PDO}}$ ) and temperature. In our study, such sudden drops in temperature before  
202  $D_{\text{LCO}}$  (or  $D_{\text{PDO}}$ ) that induce rapid leaf senescence, named cold events, were determined from  
203 daily minimum air temperature ( $T_{\min}$ ). First, we determined the  $T_{\min}$  threshold below which there  
204 could potentially be a cold event for each pixel; this was the lowest  $T_{\min}$  during the 6 to 35 days  
205 before  $D_{\text{LCO}}$  for all years. If the lowest  $T_{\min}$  was higher than  $0^{\circ}\text{C}$ , the  $T_{\min}$  threshold was set to  
206  $0^{\circ}\text{C}$ . Second, for a given pixel, a year was determined as a candidate cold event year if the  
207 lowest  $T_{\min}$  in the period 1 to 5 days before  $D_{\text{LCO}}$  was lower than the above-mentioned  $T_{\min}$   
208 threshold. Then, from the years that were not candidate cold event years, we determined the  
209 latest  $D_{\text{LCO}}$  that was not caused by a cold event for that pixel. Finally, a  $D_{\text{LCO}}$  was recognized as  
210 caused by a cold event if it was both in the candidate cold event years and earlier than the latest  
211  $D_{\text{LCO}}$  that was not caused by a cold event. This empirical approach may have overestimated the  
212 number of years with cold events before  $D_{\text{LCO}}$ , but our objective was to exclude as many cold  
213 events as possible. On clear nights, the temperature of the canopy surface could be lower than  
214 the air temperature, so we also evaluated the first step by using  $2^{\circ}\text{C}$  as the  $T_{\min}$  threshold. The cold event years accounted  
215 for a very small fraction of years with phenological data (Table S4).

217 Here, the daily minimum temperature used to determine cold events for satellite-derived  
218  $D_{LCO}$  was extracted from the CRU-NCEP dataset (Version 7.2, <https://vesg.ipsl.upmc.fr>,  
219 assessed on 10 January 2019), which provides 6-hourly data at a spatial resolution of  $0.5^\circ \times 0.5^\circ$   
220 through 2016 (Viovy, 2018). The CRU-NCEP 7.2 is a combination of two datasets: the CRU  
221 TS3.2  $0.5^\circ \times 0.5^\circ$  monthly data covering the period 1901 to 2002 and the NCEP reanalysis  $2.5^\circ$   
222  $\times 2.5^\circ$  6-hourly data covering the period 1948 to 2016. We determined daily  $T_{min}$  as the  
223 minimum value of the four 6-hourly minimum temperature values for each day. The  
224 CRU-NCEP data were resampled at  $0.05^\circ \times 0.05^\circ$  by replication to match the  $D_{LCO}$  data. Daily  
225  $T_{min}$  for *in situ* observations in China was extracted from the “Daily Surface Climate Variables  
226 of China” catalog (a dataset named SURF\_CLI\_CHN\_MUL\_DAY\_V3.0), which includes daily  
227 climate data for 2474 sites in China from January 1951 to July 2014, provided by the Chinese  
228 Meteorological Administration via an offline request on 18 January 2015. The distance between  
229 phenological and meteorological stations was less than 25 km. Daily  $T_{min}$  for  $D_{PDO}$  was  
230 calculated from the half-hourly temperature dataset provided by FLUXNET2015.

## 231 2.5 | Analyses

232 Temporal trends in  $D_{LCO}$  were quantified as the slopes of linear regressions between a  
233 variable and year by using OLSR. To complement the temporal changes assessed by using  
234 OLSR, a non-parametric approach (the Theil-Sen estimator (Sen, 1968; Theil, 1992)) was also  
235 used to calculate the trends in  $D_{LCO}$ . The temporal trend was calculated for each time series for  
236 the ground-based observations and for each pixel for the satellite observations. We focused only  
237 on the temporal trends for the pixels and time series of *in situ* phenological observations with a  
238 multiyear mean of  $D_{LCO}$  occurring after the summer solstice. Phenological records were not  
239 available for some of the years of the time series for calculating more trends or correlations,  
240 because the time series may have had missing values owing to a lack of observation. However,  
241 the time series used for the regressions contained at least 10 years of observational records and  
242 at least one record for any 3 consecutive years. If two or more parts of the time series met these  
243 criteria, the most recent part was used.

244  $T_{min}$  has long been recognized as the indicator of the thermal condition that induces  
245 autumnal leaf coloration (Tang *et al.*, 2016). We investigated the impacts of temperature and  
246 precipitation, respectively, on the satellite-derived  $D_{LCO}$  by calculating the  $R_{TN}$  values between

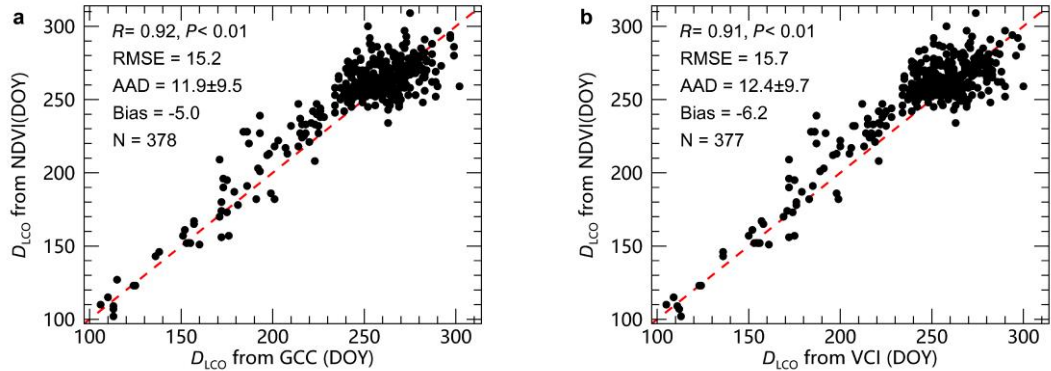
247  $D_{LCO}$  and the mean of monthly average daily minimum temperature ( $T_{min}$ ) for the pre- $D_{LCO}$   
248 period, with concurrent total precipitation as the control variable, and between  $D_{LCO}$  and  
249 pre- $D_{LCO}$  total precipitation ( $R_{PRE}$ ), with concurrent  $T_{min}$  as the control variable for 2000–2018.  
250 The pre- $D_{LCO}$  period for  $T_{min}$  (Fig. S2) was defined as the period preceding the multiyear mean  
251  $D_{LCO}$  for which  $T_{min}$  had the strongest interannual partial correlation with  $D_{LCO}$ , with concurrent  
252 total precipitation as a control variable. The candidate period had the earliest start in June and a  
253 fixed end at the multiyear mean  $D_{LCO}$ , at steps of 1 month. If the multiyear mean  $D_{LCO}$  was in  
254 the first half of a month, then the pre- $D_{LCO}$  period ended at the month preceding the multiyear  
255 mean  $D_{LCO}$ . Otherwise, the pre- $D_{LCO}$  period ended at the month of the multiyear mean  $D_{LCO}$ .  
256 The pre- $D_{LCO}$  period for precipitation was defined similarly. The impacts of climatic factors on  
257 the advanced stages of leaf coloration were investigated similarly. The data for  $T_{min}$  and  
258 precipitation were extracted from the Climatic Research Unit (CRU) Time-Series (TS) 4.03  
259 dataset (<http://data.ceda.ac.uk>, accessed on 11 June 2019), which provided monthly data at a  
260 spatial resolution of  $0.5^\circ \times 0.5^\circ$  until 2018. It should be noted that  $T_{min}$  in the dataset is an  
261 approximation of the mean of daily minimum temperature for a calendar month, which is  
262 arithmetically calculated from gridded monthly mean temperature and the diurnal temperature  
263 range (Harris *et al.*, 2014) and does not exactly reflect the interannual variations in the absolute  
264 minimum temperature (Körner & Hiltbrunner, 2018) experienced by plants before  $D_{LCO}$ . The  
265 CRU data were resampled at  $0.05^\circ \times 0.05^\circ$  by replication to match the  $D_{LCO}$  data. We also  
266 investigated the impact of  $T_{min}$  and precipitation on  $D_{LCO}$  from ground-based observations in  
267 China and on  $D_{PDO}$  from eddy-covariance sites as complementary to satellite-derived of  $D_{LCO}$ .  
268 Climatic data from the nearest meteorological station (<25 km), provided by the Chinese  
269 Meteorological Administration, were used for *in situ*  $D_{LCO}$  in China.

## 270 3 | RESULTS

### 271 3.1 | Comparison of satellite $D_{LCO}$ with PhenoCam $D_{LCO}$

272 The satellite  $D_{LCO}$  explained about 80% of the variations in PhenoCam derived  $D_{LCO}$  ( $N =$   
273 378 and 377 for GCC and VCI) (Fig. 2). The difference between the satellite  $D_{LCO}$  and the  
274 PhenoCam  $D_{LCO}$  are caused by the mismatch between the annual NDVI and GCC (or VCI)  
275 trajectories due to difference in spatial coverage between the PhenoCam and satellite pixel in the

276 cases of phenologically heterogeneous land surface (Zhang *et al.*, 2018).



277

278 **Fig. 2** Comparison between satellite  $D_{LCO}$  and PhenoCam  $D_{LCO}$ . The PhenoCam  $D_{LCO}$  was  
279 determined from GCC (a) and VCI (b), respectively.  $R$ : Pearson's correlation coefficient; RMSE:  
280 root mean square error; AAD: average absolute difference; bias is defined as the difference  
281 between the mean of satellite  $D_{LCO}$  and the mean of PhenoCam  $D_{LCO}$ , and negative bias means  
282 the PhenoCam  $D_{LCO}$  is earlier than satellite  $D_{LCO}$ .

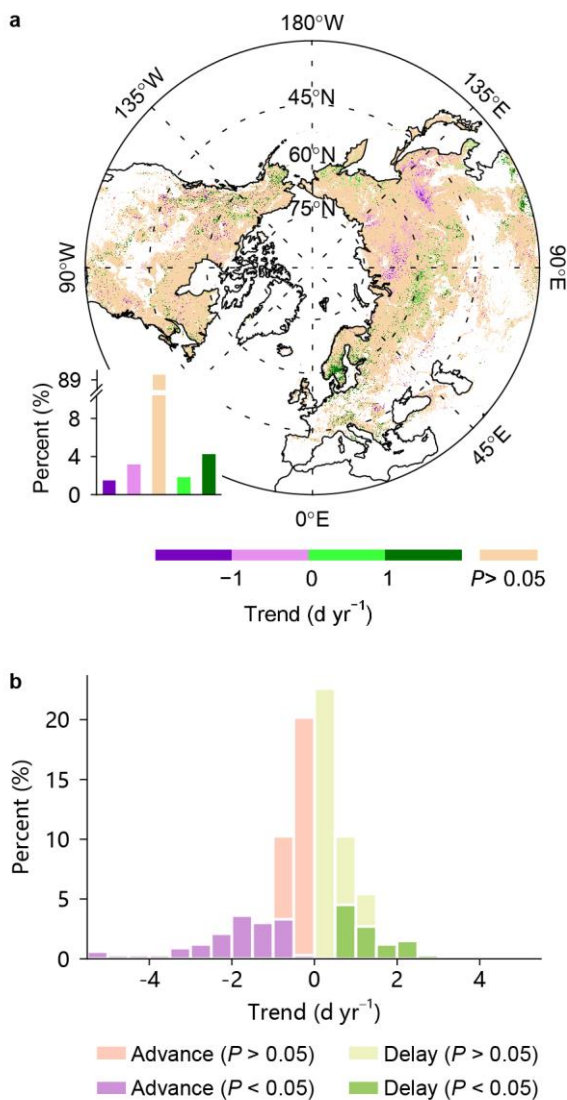
283

### 284 3.2 |Temporal trends in $D_{LCO}$

285  $D_{LCO}$  was not significantly delayed in 94% of the area during the study period, as assessed  
286 by ordinary least squares regression (OLSR) between satellite-derived  $D_{LCO}$  and respective years.  
287 The few pixels with a significant delay trend (6%;  $P < 0.05$ ,  $t$ -test) were scattered across the  
288 Northern Hemisphere (Fig. 3a). Leaf color often changes rapidly owing to cold events in autumn;  
289 these rapid changes introduced noise to the  $D_{LCO}$  time series and trends. Excluding years with  
290 cold events before  $D_{LCO}$  produced similar results (Fig. S3 and Table S5). Because the sample  
291 size (i.e., the number of years in the  $D_{LCO}$  time series) for calculating the trend was small, we  
292 also used the Theil-Sen estimator to determine temporal  $D_{LCO}$  trends. This method generated  
293 results supporting the lack of changes in  $D_{LCO}$  (no significant delay in 96% of the area;  $P < 0.05$ ,  
294 Mann-Kendall test; Fig. S4a and Table S6). When we redefined  $D_{LCO}$  as the date when the rate  
295 of change of curvature of a double logistic curve (Beck *et al.*, 2006) fitted to the NDVI series  
296 reached its first local minimum in the descending period (Zhang *et al.*, 2003), we obtained  
297 similar results (Fig. S4b and c). Complementary to satellite-derived  $D_{LCO}$ , we also examined the  
298 temporal changes of  $D_{LCO}$  by using ground-based leaf coloration data from China.  $D_{LCO}$  was not

299 significantly delayed for 90% and 94% of the 332 time series as shown by OLSR (Fig. 3b) and  
300 the Theil-Sen method (Table S6), respectively. As with the remotely sensed data, excluding cold  
301 events from the ground-based data revealed only a few significant delays of  $D_{LCO}$  (Table S5).

302



303

304 **Fig. 3** Temporal trends in the timing of the onset of leaf coloration ( $D_{LCO}$ ), as retrieved from  
305 satellite and *in situ* observations. a, Satellite-derived  $D_{LCO}$  trends over 2000–2018. The bar chart  
306 in the bottom-left corner shows the percentage of area within each interval of the significant  
307 temporal trends and the percentage of area with nonsignificant trends, indicated by the color  
308 scale at the bottom. Positive and negative trend values refer to significantly delayed and  
309 advanced  $D_{LCO}$ , respectively.  $D_{LCO}$  is defined as the date when NDVI decreases by 10% of its

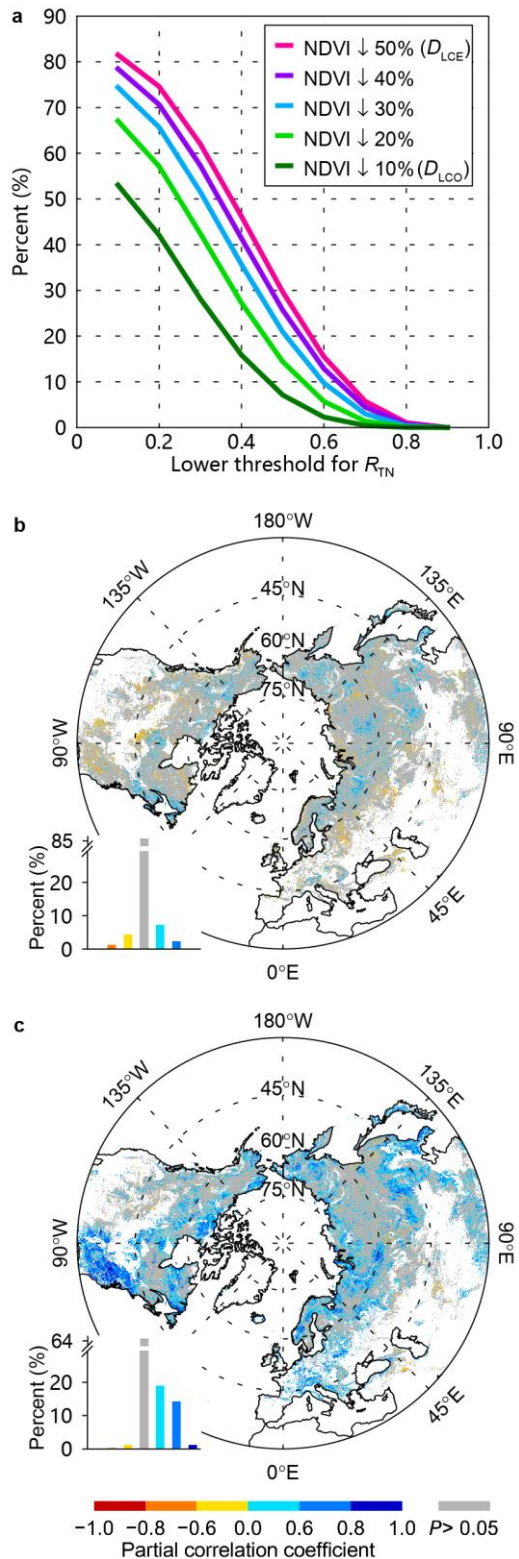
310 annual amplitude in autumn, based on a generalized sigmoid function fitted from the annual  
311 NDVI profile. Pixels dominated by croplands or with low vegetation coverage, weak seasonality,  
312 or peak NDVI in October–April were discarded. b, Ground-observed  $D_{LCO}$  trends derived over  
313 1971–1997 from *in situ* leaf coloration observations in China. Significant temporal trends were  
314 determined by using *t*-tests at  $P < 0.05$  and OLSR between  $D_{LCO}$  and respective years.

315

### 316 **3.3 |Correlation between $D_{LCO}$ and temperature**

317 With the same data that were used for  $D_{LCO}$  assessment, we verified that a delay in  $D_{LCE}$   
318 was correlated with an increase in temperature for the period preceding  $D_{LCE}$  (Estrella & Menzel,  
319 2006; Delpierre *et al.*, 2009; Gill *et al.*, 2015; Liu *et al.*, 2016; Fu *et al.*, 2018) (Fig. 4a and c). In  
320 addition, since in a few studies(Ren *et al.*, 2017; Berman *et al.*, 2020), end of leaf coloration was  
321 defined as the dates when NDVI drops by 60% or 90% of its annual amplitude, we also  
322 calculated the partial correlations between each of those dates and the temperature, respectively,  
323 and the correlations were similar to the that between  $D_{LCE}$  and the pre- $D_{LCE}$  temperature (Fig.  
324 S5).  $D_{LCO}$ , however, was not correlated with pre- $D_{LCO}$   $T_{min}$ , with only 9% of the area in scattered  
325 pixels showing a significant positive correlation and 5% showing a significant negative  
326 correlation (Fig. 4b).  $D_{LCO}$  was positively partially correlated with pre- $D_{LCO}$  total precipitation  
327 in 13% of the area, mainly in the temperate grassland of Northern America and in the middle  
328 latitudes of Eurasia, sub-arctic grassland, and alpine steppe of the Tibetan Plateau (Fig. S6).  
329 Therefore, neither pre- $D_{LCO}$   $T_{min}$  nor precipitation was a useful predictor of  $D_{LCO}$  in most areas.  
330 We obtained similar results when using a pre- $D_{LCO}$  period with a fixed length (1 month  
331 preceding  $D_{LCO}$ ) to calculate pre- $D_{LCO}$   $T_{min}$  (Fig. S7). Moreover, a shorter pre- $D_{LCO}$  period (15  
332 days preceding  $D_{LCO}$ ) showed similar results, with only 5% of the area showing a significant  
333 positive correlation between  $D_{LCO}$  and pre- $D_{LCO}$   $T_{min}$  (Fig. S8). We also investigated the  
334 relationship between  $D_{LCO}$  and the lowest daily minimum temperature during the 15 days before  
335 the multiyear mean  $D_{LCO}$ . We found that only 3% of the area showed a significant positive  
336 correlation (Fig. S9). A few studies have suggested that the date of onset of green-up may affect  
337 leaf coloration through legacy effects (Fu *et al.*, 2014; Keenan & Richardson, 2015; Liu *et al.*,  
338 2016), but including this date as an extra control variable in the partial correlation analyses did

339 not affect the results (Fig. S10). The *in situ* phenological records in China indicated that  
340 ground-observed  $D_{LCO}$  was positively partially correlated with pre- $D_{LCO}$   $T_{min}$  for 13% of the time  
341 series and was not correlated with pre- $D_{LCO}$   $T_{min}$  for 82% of the time series (Table 1). Excluding  
342  $D_{LCO}$  caused by cold events produced similar results (Fig. S11 and Table S7). Overall, these  
343 results suggest that an increase in pre- $D_{LCO}$   $T_{min}$  is not likely to delay  $D_{LCO}$  in most areas in the  
344 middle and high northern latitudes.



345

346 **Fig. 4** Relationships between the timing of different stages of leaf coloration (retrieved from  
 347 satellite images) and the mean daily minimum temperature ( $T_{\min}$ ) for an optimized period  
 348 preceding the respective stage over the period 2000–2018. a, Percentage of area for which the  
 349 partial correlation coefficient ( $R_{TN}$ ) between the timing of a given stage of leaf coloration

350 (defined by NDVI decrease) and  $T_{\min}$  for an optimized period preceding the stage is higher than  
 351 a given threshold indicated by the horizontal axis. For example,  $R_{TN}$  for the onset of leaf  
 352 coloration ( $D_{LCO}$ , 10% decrease in NDVI) is higher than 0.2 in about 40% of the area. b, Spatial  
 353 pattern of the partial correlation coefficient between  $D_{LCO}$  and pre- $D_{LCO}$   $T_{\min}$ . c, Spatial pattern  
 354 of the partial correlation coefficient between timing of the end of leaf coloration ( $D_{LCE}$ , 50%  
 355 decrease in NDVI) and pre- $D_{LCE}$   $T_{\min}$ . The bar charts in (b) and (c) show the percentage of area  
 356 for each interval of the partial correlation coefficient ( $P < 0.05$ ), with the coefficient indicated  
 357 by the color scale at the bottom. Non-significant correlations ( $P > 0.05$ ) are in gray. Pixels  
 358 dominated by croplands or with low vegetation coverage, weak seasonality, or peak NDVI in  
 359 October–April were discarded.

360  
 361 **Table 1.** Percentage of correlations between  $D_{LCO}$  or  $D_{PDO}$  and each climate factor for each  
 362 interval of the partial correlation coefficient.

Metric	Number of time series	Climate factor	Interval of the partial correlation coefficient ( $P < 0.05$ )						$P > 0.05$
			[-1.0, -0.8]	[-0.8, -0.6]	[-0.6, 0)	(0, 0.6]	(0.6, 0.8]	(0.8, 1.0]	
<i>in situ</i> $D_{LCO}$	332	Temperature	0	2	3	4	8	1	82
		Precipitation	0	3	3	4	5	0	85
FLUXNET2015	36	Temperature	0	5	3	0	3	0	89
		Precipitation	0	6	0	8	3	5	78

363  $D_{PDO}$ , timing of the onset of the decrease in maximum canopy photosynthetic capacity in autumn;  $D_{LCO}$ , timing of  
 364 the onset of leaf coloration in autumn. The relationships between  $D_{LCO}$  (or  $D_{PDO}$ ) and temperature were determined  
 365 by using a partial correlation analysis between  $D_{LCO}$  (or  $D_{PDO}$ ) and pre- $D_{LCO}$  (or pre- $D_{PDO}$ ) mean daily minimum  
 366 temperature, with concurrent total precipitation as the control variable. The relationships between  $D_{LCO}$  (or  $D_{PDO}$ )  
 367 and pre- $D_{LCO}$  (or pre- $D_{PDO}$ ) precipitation were determined similarly. The data in the farthest right column indicate  
 368 the percentages of area or time series with non-significant correlations.

369  
 370 In previous analyses of *in situ* and satellite observations (Garonna *et al.*, 2014; Gill *et al.*,  
 371 2015; Liu *et al.*, 2016), the advanced stage of autumnal leaf senescence, indicated by  $D_{LCE}$ , was  
 372 significantly delayed in a larger proportion of areas, or time series, than was  $D_{LCO}$  in our study.

In the current study,  $D_{LCE}$  was also significantly delayed in more areas than  $D_{LCO}$  (Fig. S12), probably because the timings of the earlier stages of leaf coloration determined from satellite data were less affected by  $T_{min}$  than the later stages (Fig. 4a and Fig. S13). Evidence for photoperiodic control of the start of leaf senescence (Keskitalo *et al.*, 2005; Fracheboud *et al.*, 2009) suggests that the early phases of leaf senescence are insensitive to warming, in contrast to the later phases. Since the degradation of chlorophyll starts earlier than leaf coloration (Lim *et al.*, 2007; Tang *et al.*, 2016), the timing of autumnal phenological metrics that closely follow chlorophyll degradation before  $D_{LCO}$  should be less delayed by temperature increase than  $D_{LCO}$  if chlorophyll degradation is triggered by the photoperiod. To test this deduction, we analyzed the relationship between  $D_{PDO}$  in autumn and pre- $D_{PDO}$   $T_{min}$  (determined in a similar way to pre- $D_{LCO}$   $T_{min}$ ), since  $D_{PDO}$  is notably strongly controlled by chlorophyll concentration. Indeed,  $D_{PDO}$  was positively correlated with pre- $D_{PDO}$   $T_{min}$  in 3% of the 36 eddy-covariance towers and was not correlated with pre- $D_{PDO}$   $T_{min}$  in 89% of the eddy-covariance records (Table 1). Excluding  $D_{PDO}$  caused by cold events produced similar results (Table S7). Moreover,  $D_{PDO}$  and pre- $D_{PDO}$   $T_{min}$  were less positively correlated than were NDVI-derived  $D_{LCO}$  and pre- $D_{LCO}$   $T_{min}$  at the same sites during the same periods (3% and 6% of the sites for  $D_{PDO}$  and  $D_{LCO}$ , respectively, Table S8), probably because the start of autumnal chlorophyll degradation was controlled by photoperiod and was not delayed by higher temperature (Keskitalo *et al.*, 2005; Fracheboud *et al.*, 2009; Bauerle *et al.*, 2012).

## 4 | DISCUSSION

### 4.1 | Whether summer NDVI decline contributed to the absence of $D_{LCO}$ delay and $D_{LCO}$ -temperature relationship

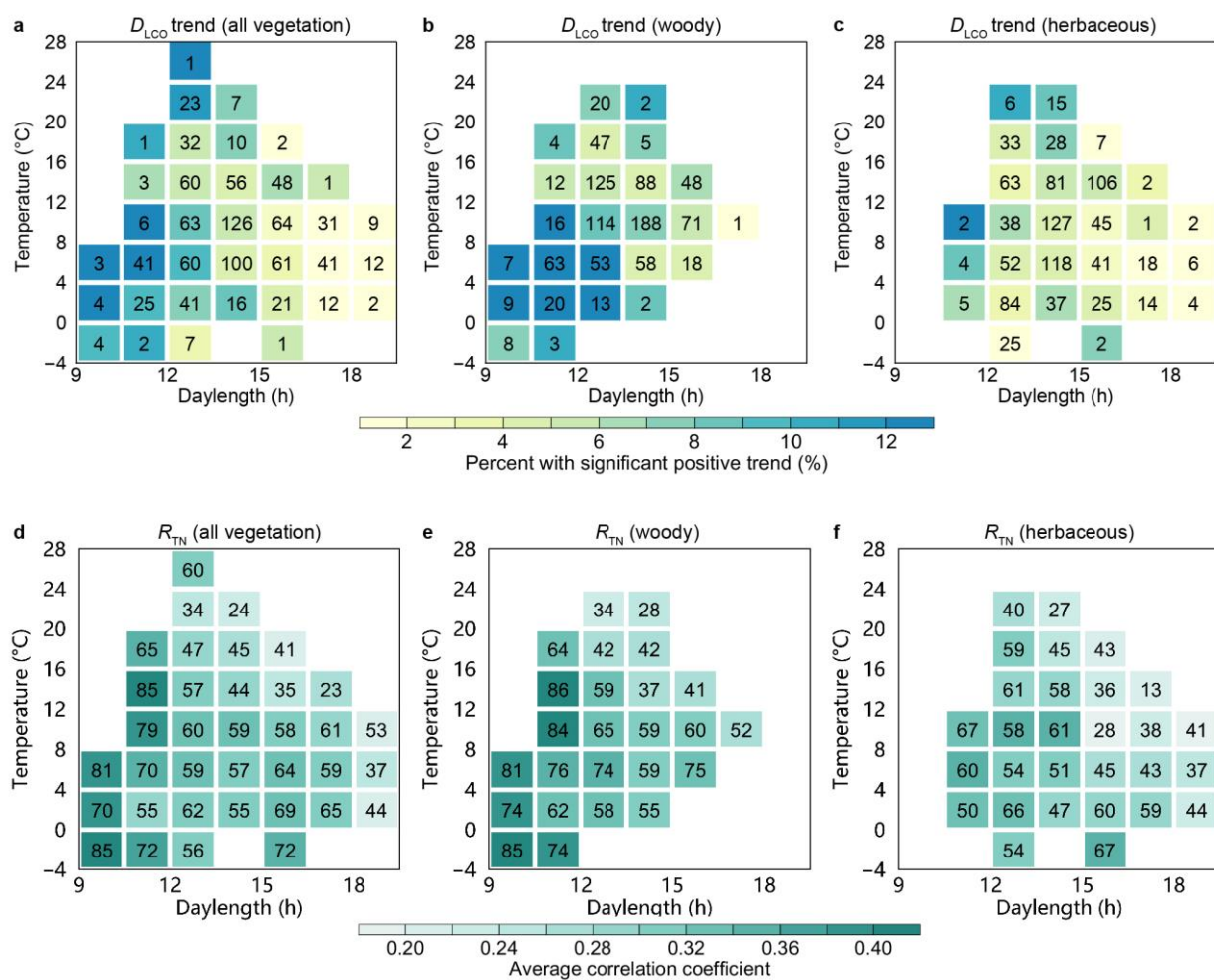
Our findings are mainly based on  $D_{LCO}$  determined on the annual trajectory of NDVI. In some deciduous forest, NDVI may decline in early summer (i.e., late May–July) before leaf coloration, and this may potentially interfere with the determination of  $D_{LCO}$  to some extent (Elmore *et al.*, 2012). To test whether early summer NDVI decline would affect the results in our study, for the pixels classified as deciduous broadleaf forest in the MODIS land-cover product in 2009, we redefined independently  $D_{LCO}$  in three different ways: (1) We used a modified double logistic model that considers early summer NDVI decline (Elmore *et al.*, 2012)

402 to fit the NDVI time series instead of the original double logistic function for the pixels  
403 classified as deciduous broadleaf forest.  $D_{LCO}$  was then determined as the date when the rate of  
404 change of the curvature of a double logistic function fitted to the NDVI time series reached its  
405 first local minimum in the descending period; (2)  $D_{LCO}$  was defined as the date when NDVI  
406 decreased by 10% of its annual amplitude from 1 August. The maximum value used to  
407 determine the annual amplitude was the mean value of the upper quartile of the fitted NDVI  
408 values in August; and (3)  $D_{LCO}$  was defined as the date when NDVI decreased by 10% of its  
409 annual amplitude from 16 August. The maximum value used to determine the annual amplitude  
410 was the mean value of the upper quartile of the fitted NDVI values in the second half of August.  
411 The results with deciduous broadleaf forest pixels redefined in these three ways (Figs. S14–S22)  
412 were similar to those calculated without considering the effect of early summer NDVI decline  
413 (Figs. 3–6; Fig. S4).

#### 414 **4.2 | Dependence of leaf senescence on daylength**

415 Overall, these results suggest that temperature does not initiate senescence in autumn in  
416 most areas; rather, it influences the speed of senescence after it starts (Fracheboud *et al.*, 2009).  
417 The lack of a positive correlation between  $D_{LCO}$  (or  $D_{PDO}$ ) and pre- $D_{LCO}$  (or pre- $D_{PDO}$ )  
418 temperature suggests an overriding photoperiodic control that makes the timing of the onset of  
419 leaf senescence stable. In the areas with longer daylengths (calculated for each pixel/location at  
420 multiyear mean  $D_{LCO}$  over 2000–2018), there were proportionally fewer significant  $D_{LCO}$  delays  
421 during 2000–2018 (Fig. 5a and Fig. S23a), and the positive relationship between  $D_{LCO}$  and  
422 pre- $D_{LCO}$   $T_{min}$  was slightly weaker, as indicated by the smaller partial correlation coefficient  
423 between them (Fig. 5d). Such patterns were more prominent for woody vegetation than for  
424 herbaceous vegetation (Fig. 5b, c, e and f; Fig. S23b and c), in agreement with experimental  
425 findings suggesting that the initiation of leaf senescence in woody plants is likely controlled by  
426 photoperiod (Keskitalo *et al.*, 2005; Fracheboud *et al.*, 2009). These findings indicate stronger  
427 photoperiodic control in areas where daylength at  $D_{LCO}$  is longer (i.e., shorter nights), possibly  
428 because plants respond to the length of uninterrupted darkness rather than daylength (Hamner,  
429 1940; Borthwick & Hendricks, 1960; Paus *et al.*, 1986; Howe *et al.*, 1995). Interestingly, for  
430 vegetation with a daylength at  $D_{LCO}$  of more than 13.5 h,  $D_{LCO}$  was more positively correlated

431 with pre- $D_{LCO}$   $T_{min}$  in colder areas at a given daylength (Fig. 5d–f), indicating a stronger effect  
 432 of temperature in areas with harsh temperature conditions, consistent with experimental studies  
 433 (Zohner *et al.*, 2016; Ford *et al.*, 2017). Therefore, although for these types of vegetation the  
 434 correlation between  $D_{LCO}$  and temperature is weak, probably because of stronger photoperiodic  
 435 control, there is still a signal of temperature influence on  $D_{LCO}$ , reflecting a stronger selection  
 436 pressure in harsher temperature environments. The correlation between  $D_{LCO}$  and pre- $D_{LCO}$  total  
 437 precipitation was independent of photoperiod and was slightly stronger for the areas with a  
 438 higher daily minimum temperature before  $D_{LCO}$ , mostly because of the stronger effect of  
 439 precipitation in delaying  $D_{LCO}$  in herbaceous vegetation (Figs. S5 and S24). The dependences of  
 440  $D_{LCO}$  trends on photoperiod and of the correlation between  $D_{LCO}$  and pre- $D_{LCO}$   $T_{min}$  on  
 441 photoperiod were also found when years with cold events before  $D_{LCO}$  were excluded (Fig.  
 442 S25).



443  
 444 **Fig. 5** Dependence of temporal trends in the timing of the onset of leaf coloration ( $D_{LCO}$ , a–c)

and of the partial correlation coefficient ( $R_{TN}$ , d–f) between  $D_{LCO}$  and pre- $D_{LCO}$  mean daily minimum temperature ( $T_{min}$ ) on daylength and temperature at  $D_{LCO}$  over the period 2000–2018. Daylength (indicated by the horizontal axis) was calculated for each pixel (location) at multiyear mean  $D_{LCO}$  over 2000–2018 ( $D_{LCO-MEAN}$ ), and temperature (indicated by the vertical axis) is the mean of daily minimum temperature in the month preceding  $D_{LCO-MEAN}$ . a, All vegetation. Color indicates the percentage of area with significant ( $P < 0.05$ )  $D_{LCO}$  delays in each cell (i.e., a specific temperature  $\times$  daylength combination), as indicated in the scale at the bottom. The number in each cell indicates the ratio (unit: %) of the area in each cell to the total area with  $D_{LCO}$  retrieval (i.e., Northern Hemisphere from 30°N–75°N). The temporal trends and their significances were determined with ordinary least squares regression and  $t$ -tests. b and c, The same as (a) but for woody and herbaceous vegetation, respectively. d, All vegetation. Color indicates the average of the positive  $R_{TN}$ , as indicated in the scale at the bottom. The number in each cell indicates the percentage of area with a positive correlation in each cell. e and f, The same as (d) but for woody and herbaceous vegetation, respectively. Each cell represents 4 °C of temperature and 1.5 h of daylength. Only cells where the ratio of the area of the cell to the total area is  $>1\%$  are represented. Woody and herbaceous vegetation are merged from Classes 1–6 and Class 10, respectively, in the MODIS land-cover product (MCD12C1, Version 6) for 2009.

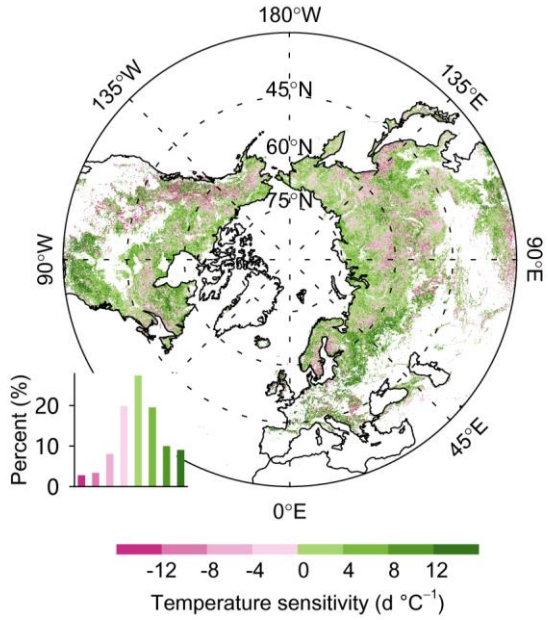
462

Although observational evidence is limited, experimental results have been reported for the photoperiodic induction of leaf senescence in several, mostly woody, species (Table S1). However, in those manipulative experiments, daylength was altered by several hours ( $>4$  h, Table S1), which is more extreme than the natural conditions plants are likely to experience. Daylength depends only on the day of year and location. Because of the inter-annual limited variations in the timings of leaf coloration or senescence onset, the fluctuation in daylength under natural conditions is far less than that in manipulative experiments. Therefore, the role of photoperiod in leaf senescence identified under such experimental conditions does not necessarily apply to plants under natural conditions. The results in this study support experimental findings in wild plants at the biome and continental scales and show that

473 photoperiod influences the onset of leaf coloration, which closely follows the initial of leaf  
474 senescence.

475 **4.3 | Implications**

476 Autumnal leaf senescence in preparation for overwintering is an evolutionary trade-off  
477 between the reallocation of leaf nutrients before leaf shed to reduce the risk of frost damage and  
478 the assimilation of carbon (Estiarte & Peñuelas, 2015). The response of leaf senescence to an  
479 increase in temperature in autumn influences this trade-off. The absence of delays over time in  
480 the onset of leaf coloration and in the onset of decrease in maximum canopy photosynthetic  
481 capacity in response to climate warming, as observed in our study, may limit the detrimental  
482 effects of frost in autumn (Liu *et al.*, 2018) and may also pose limited impacts on the start of the  
483 remobilization and resorption of nutrients (Estiarte & Peñuelas, 2015). The stronger positive  
484 correlation between the advanced stage of leaf coloration and the  $T_{\min}$  for an optimized period  
485 preceding that stage (Fig. 4 and Fig. S13), implies that climatic warming may help to extend the  
486 period from the onset to the end of leaf coloration in extensive areas across the middle and high  
487 northern latitudes (Fig. 6); this in turn may increase the efficiency of nitrogen resorption  
488 (Rennenberg *et al.*, 2010) and increase the vegetation greenness in this period, which will  
489 modify on the surface energy balance through biophysical processes (Shen *et al.*, 2015). The  
490 extended period of leaf coloration may also prolong the plant transpiration time and increase soil  
491 water consumption. The impact of autumn warming on net ecosystem productivity is dual,  
492 increasing both respiratory flux to the atmosphere (Piao *et al.*, 2008) and forest gross primary  
493 photosynthesis (Keenan *et al.*, 2014). The relatively static onset date of leaf coloration and its  
494 weak response to temperature would preclude the vegetation from fully using the potential  
495 increase in CO<sub>2</sub> assimilation in early autumn induced by warming (Stinziano & Way, 2017).  
496 Combined with a delay in the end of the season and a respiration increase due to warming, this  
497 suggests that additional warming will probably not result in a continuous increase in autumn  
498 CO<sub>2</sub> assimilation.



499

500 **Fig. 6** Difference in temperature sensitivity between the end and onset of leaf coloration ( $D_{LCE}$   
501 and  $D_{LCO}$ ) over the period 2000–2018. The temperature sensitivity of  $D_{LCO}$  is defined as the  
502 coefficient for pre- $D_{LCO}$  mean daily minimum temperature ( $T_{min}$ ) in a linear regression in which  
503  $D_{LCO}$  is set as the dependent variable and pre- $D_{LCO}$   $T_{min}$  and pre- $D_{LCO}$  total precipitation are  
504 independent variables. The temperature sensitivity of  $D_{LCE}$  is calculated in a similar way.  $D_{LCO}$   
505 and  $D_{LCE}$  are determined as the dates when NDVI decreases by 10% and 50%, respectively, of  
506 its annual amplitude, based on a generalized sigmoid function fitted from the annual NDVI  
507 profile. The bar chart in the bottom-left corner shows the percentage of area for each interval of  
508 the temperature sensitivity indicated by the color scale at the bottom. Positive values (green)  
509 indicate that  $D_{LCE}$  is more sensitive to temperature than  $D_{LCO}$ , whereas negative values (pink)  
510 indicate that  $D_{LCO}$  is more sensitive to temperature than  $D_{LCE}$ .

511 **4.4 | Concluding remarks**

512 In summary, satellite NDVI time series and ground-based phenological observations  
513 indicated no significant delay in the start of autumnal leaf coloration for most areas covered by  
514 natural vegetation over middle and high northern latitudes. Neither pre- $D_{LCO}$  temperature nor  
515 pre- $D_{LCO}$  precipitation significantly affected the interannual variations of the start of leaf  
516 coloration in most areas, indicating that the start of leaf senescence is triggered by photoperiod.  
517 Interestingly, there was a weaker positive correlation between the start of autumnal leaf

coloration and pre- $D_{LCO}$   $T_{min}$  for vegetation in regions with longer daylength, indicating strong photoperiodic control of the start of leaf senescence. For vegetation with a given daylength at  $D_{LCO}$  longer than 13.5 h, the positive correlation between  $D_{LCO}$  and pre- $D_{LCO}$   $T_{min}$  was slightly stronger in colder areas, suggesting that there is strong selection pressure in harsher temperature environments on the timing of leaf coloration onset and that autumn warming could have a stronger delaying effect on leaf coloration onset in colder areas than in warmer areas. This study suggests that autumnal warming will not change the start date of leaf senescence, but it might slow the rate of senescence. A slower senescence speed possibly could extend the period of senescence and provide more time to reallocate nutrients and prepare for overwintering. Such changes could substantially affect carbon and nutrient cycles. Our study provides a foundation for understanding the complex relationships among nutrient cycling, vegetation growth, energy exchange, and climate change in autumn in temperate and boreal regions dominated by winter deciduous vegetation.

### 531 **Data Availability**

532 The data supporting the findings of this study are available through the links given in the paper.

### 533 **References**

- 534 Bauerle, W.L., Oren, R., Way, D.A., Qian, S.S., Stoy, P.C., Thornton, P.E., Bowden, J.D., Hoffman, F.M. &  
535 Reynolds, R.F. (2012) Photoperiodic regulation of the seasonal pattern of photosynthetic capacity  
536 and the implications for carbon cycling. *Proceedings of the National Academy of Sciences*, **109**,  
537 8612-7.
- 538 Beck, P.S.A., Atzberger, C., Høgda, K.A., Johansen, B. & Skidmore, A.K. (2006) Improved monitoring of  
539 vegetation dynamics at very high latitudes: A new method using MODIS NDVI. *Remote Sensing  
540 of Environment*, **100**, 321-334.
- 541 Berman, E.E., Graves, T.A., Mikle, N.L., Merkle, J.A., Johnston, A.N. & Chong, G.W. (2020) Comparative  
542 Quality and Trend of Remotely Sensed Phenology and Productivity Metrics across the Western  
543 United States. *Remote Sensing*, **12**
- 544 Borthwick, H.A. & Hendricks, S.B. (1960) Photoperiodism in Plants. *Science*, **132**, 1223-1228.
- 545 Cao, R., Chen, Y., Shen, M., Chen, J., Zhou, J., Wang, C. & Yang, W. (2018) A simple method to improve  
546 the quality of NDVI time-series data by integrating spatiotemporal information with the  
547 Savitzky-Golay filter. *Remote Sensing of Environment*, **217**, 244-257.
- 548 Chen, J., Rao, Y., Shen, M., Wang, C., Zhou, Y., Ma, L., Tang, Y. & Yang, X. (2016) A simple method for  
549 detecting phenological change from time series of vegetation index. *IEEE Transactions on  
550 Geoscience and Remote Sensing*, **54**, 3436-3449.
- 551 China Meteorological Administration (1993) *Observation criterion of agricultural meteorology*. China  
552 Meteorological Press, Beijing (in Chinese).

- 553 Delpierre, N., Dufrêne, E., Soudani, K., Ulrich, E., Cecchini, S., Boé, J. & François, C. (2009) Modelling  
554 interannual and spatial variability of leaf senescence for three deciduous tree species in France.  
555 *Agricultural and Forest Meteorology*, **149**, 938-948.
- 556 Elmore, A.J., Guinn, S.M., Minsley, B.J. & Richardson, A.D. (2012) Landscape controls on the timing of  
557 spring, autumn, and growing season length in mid-Atlantic forests. *Global Change Biology*, **18**,  
558 656-674.
- 559 Estiarte, M. & Peñuelas, J. (2015) Alteration of the phenology of leaf senescence and fall in winter  
560 deciduous species by climate change: effects on nutrient proficiency. *Global Change Biology*, **21**,  
561 1005-1017.
- 562 Estrella, N. & Menzel, A. (2006) Responses of leaf colouring in four deciduous tree species to climate and  
563 weather in Germany. *Climate Research*, **32**, 253-267.
- 564 Ford, K.R., Harrington, C.A. & Clair, J.B.S. (2017) Photoperiod cues and patterns of genetic variation limit  
565 phenological responses to climate change in warm parts of species' range: Modeling  
566 diameter-growth cessation in coast Douglas-fir. *Global Change Biology*, **23**, 3348-3362.
- 567 Fracheboud, Y., Luquez, V., Björkén, L., Sjödin, A., Tuominen, H. & Jansson, S. (2009) The control of  
568 autumn senescence in European aspen. *Plant Physiology*, **149**, 1982-1991.
- 569 Friedl, M. & Sulla-Menashe, D. (2015) MCD12C1 MODIS/Terra+Aqua Land Cover Type Yearly L3 Global  
570 0.05Deg CMG V006 In: *NASA EOSDIS Land Processes DAAC*.  
571 <http://doi.org/10.5067/MODIS/MCD12C1.006>
- 572 Fu, Y.H., Piao, S., Delpierre, N., Hao, F., Hänninen, H., Liu, Y., Sun, W., Janssens, I.A. & Campioli, M.  
573 (2018) Larger temperature response of autumn leaf senescence than spring leaf-out phenology.  
574 *Global Change Biology*, **24**, 2159-2168.
- 575 Fu, Y.H., Zhao, H., Piao, S., Peaucelle, M., Peng, S., Zhou, G., Ciais, P., Huang, M., Menzel, A., Penuelas,  
576 J., Song, Y., Vitasse, Y., Zeng, Z. & Janssens, I.A. (2015) Declining global warming effects on the  
577 phenology of spring leaf unfolding. *Nature*, **526**, 104-107.
- 578 Fu, Y.S.H., Campioli, M., Vitasse, Y., De Boeck, H.J., Van den Berge, J., AbdElgawad, H., Asard, H., Piao,  
579 S., Deckmyn, G. & Janssens, I.A. (2014) Variation in leaf flushing date influences autumnal  
580 senescence and next year's flushing date in two temperate tree species. *Proceedings of the  
581 National Academy of Sciences*, **111**, 7355-7360.
- 582 Gan, S.S. & Amasino, R.M. (1997) Making sense of senescence - Molecular genetic regulation and  
583 manipulation of leaf senescence. *Plant Physiology*, **113**, 313-319.
- 584 Ganguly, S., Friedl, M.A., Tan, B., Zhang, X. & Verma, M. (2010) Land surface phenology from MODIS:  
585 Characterization of the Collection 5 global land cover dynamics product. *Remote Sensing of  
586 Environment*, **114**, 1805-1816.
- 587 Garonna, I., De Jong, R., De Wit, A.J.W., Mücher, C.A., Schmid, B. & Schaepman, M.E. (2014) Strong  
588 contribution of autumn phenology to changes in satellite-derived growing season length estimates  
589 across Europe (1982-2011). *Global Change Biology*, **20**, 3457-3470.
- 590 Ge, Q.S., Wang, H.J., Rutishauser, T. & Dai, J.H. (2015) Phenological response to climate change in  
591 China: a meta-analysis. *Global Change Biology*, **21**, 265-274.
- 592 Gill, A.L., Gallinat, A.S., Sanders-DeMott, R., Rigden, A.J., Short Gianotti, D.J., Mantooth, J.A. & Templer,  
593 P.H. (2015) Changes in autumn senescence in northern hemisphere deciduous trees: a  
594 meta-analysis of autumn phenology studies. *Annals of Botany*, **116**, 875-888.
- 595 Gu, L., Post, W.M., Baldocchi, D.D., Black, T.A., Suyker, A.E., Verma, S.B., Vesala, T. & Wofsy, S.C. (2009)  
596 Characterizing the seasonal dynamics of plant community photosynthesis across a range of  
597 vegetation types. *Phenology of Ecosystem Processes* (ed. by A. Noormets), pp. 35-58. Springer,

- 598                  New York, NY.
- 599 Hamner, K.C. (1940) Interrelation of light and darkness in photoperiod. *Botanical Gazette*, **101**, 658-687.
- 600 Harris, I., Jones, P.D., Osborn, T.J. & Lister, D.H. (2014) Updated high-resolution grids of monthly climatic  
601 observations – the CRU TS3.10 Dataset. *International Journal of Climatology*, **34**, 623-642.
- 602 Howe, G.T., Hackett, W.P., Fournier, G.R. & Klevorn, R.E. (1995) Photoperiodic responses of a northern  
603 and southern ecotype of black cottonwood. *Physiologia Plantarum*, **93**, 695-708.
- 604 Jeganathan, C., Dash, J. & Atkinson, P.M. (2014) Remotely sensed trends in the phenology of northern  
605 high latitude terrestrial vegetation, controlling for land cover change and vegetation type. *Remote  
606 Sensing of Environment*, **143**, 154-170.
- 607 Jeong, S.J., Ho, C.H., Gim, H.J. & Brown, M.E. (2011) Phenology shifts at start vs. end of growing season  
608 in temperate vegetation over the Northern Hemisphere for the period 1982–2008. *Global Change  
609 Biology*, **17**, 2385-2399.
- 610 Keenan, T.F. & Richardson, A.D. (2015) The timing of autumn senescence is affected by the timing of  
611 spring phenology: implications for predictive models. *Global Change Biology*, **21**, 2634-2641.
- 612 Keenan, T.F., Gray, J., Friedl, M.A., Toomey, M., Bohrer, G., Hollinger, D.Y., Munger, J.W., O'Keefe, J.,  
613 Schmid, H.P., Wing, I.S., Yang, B. & Richardson, A.D. (2014) Net carbon uptake has increased  
614 through warming-induced changes in temperate forest phenology. *Nature Climate Change*, **4**,  
615 598-604.
- 616 Keskitalo, J., Bergquist, G., Gardeström, P. & Jansson, S. (2005) A cellular timetable of autumn  
617 senescence. *Plant Physiol*, **139**, 1635-1648.
- 618 Klosterman, S. & Richardson, A.D. (2017) Observing Spring and Fall Phenology in a Deciduous Forest  
619 with Aerial Drone Imagery. *Sensors (Basel)*, **17**
- 620 Klosterman, S.T., Hufkens, K., Gray, J.M., Melaas, E., Sonnentag, O., Lavine, I., Mitchell, L., Norman, R.,  
621 Friedl, M.A. & Richardson, A.D. (2014) Evaluating remote sensing of deciduous forest phenology  
622 at multiple spatial scales using PhenoCam imagery. *Biogeosciences*, **11**, 4305-4320.
- 623 Körner, C. (2007) Significance of temperature in plant life. *Plant Growth and Climate Change* (ed. by J.I.L.  
624 Morison and M.D. Morecroft), pp. 48-69.
- 625 Körner, C. & Basler, D. (2010) Response-warming, photoperiods, and tree phenology. *Science*, **329**,  
626 278-278.
- 627 Körner, C. & Hiltbrunner, E. (2018) The 90 ways to describe plant temperature. *Perspectives in Plant  
628 Ecology, Evolution and Systematics*, **30**, 16-21.
- 629 Leblans, N.I.W., Sigurdsson, B.D., Vicca, S., Fu, Y.S., Penuelas, J. & Janssens, I.A. (2017) Phenological  
630 responses of Icelandic subarctic grasslands to short-term and long-term natural soil warming.  
631 *Global Change Biology*, **23**, 4932-4945.
- 632 Lim, P.O., Kim, H.J. & Nam, H.G. (2007) Leaf Senescence. *Annual Review of Plant Biology*, **58**, 115-136.
- 633 Liu, Q., Fu, Y.H., Zhu, Z., Liu, Y., Liu, Z., Huang, M., Janssens, I.A. & Piao, S. (2016) Delayed autumn  
634 phenology in the Northern Hemisphere is related to change in both climate and spring phenology.  
635 *Global Change Biology*, **22**, 3702-3711.
- 636 Liu, Q., Piao, S., Janssens, I.A., Fu, Y., Peng, S., Lian, X., Ciais, P., Myneni, R.B., Penuelas, J. & Wang, T.  
637 (2018) Extension of the growing season increases vegetation exposure to frost. *Nature  
638 Communications*, **9**, 426.
- 639 Lukasová, V., Bucha, T., Škvareninová, J. & Škvarenina, J. (2019) Validation and Application of European  
640 Beech Phenological Metrics Derived from MODIS Data along an Altitudinal Gradient. *Forests*, **10**,  
641 60.
- 642 Mariën, B., Balzarolo, M., Dox, I., Leys, S., Lorène, M.J., Geron, C., Portillo-Estrada, M., AbdElgawad, H.,

- Asard, H., Campioli, M., Mariën, B., Balzarolo, M., Dox, I., Leys, S., Lorène, M.J., Geron, C., Portillo - Estrada, M., AbdElgawad, H., Asard, H. & Campioli, M. (2019) Detecting the onset of autumn leaf senescence in deciduous forest trees of the temperate zone. *New Phytologist*, **224**, 166-176.
- Melaas, E.K., Friedl, M.A. & Zhu, Z. (2013) Detecting interannual variation in deciduous broadleaf forest phenology using Landsat TM/ETM+ data. *Remote Sensing of Environment*, **132**, 176-185.
- Menzel, A., Yuan, Y., Matiu, M., Sparks, T., Scheifinger, H., Gehrig, R. & Estrella, N. (2020) Climate change fingerprints in recent European plant phenology. *Global Change Biology*, **26**, 2599-2612.
- Myneni, R.B., Keeling, C.D., Tucker, C.J., Asrar, G. & Nemani, R.R. (1997) Increased plant growth in the northern high latitudes from 1981 to 1991. *Nature*, **386**, 698-702.
- Nagai, S., Nasahara, K.N., Muraoka, H., Akiyama, T. & Tsuchida, S. (2010) Field experiments to test the use of the normalized-difference vegetation index for phenology detection. *Agricultural and Forest Meteorology*, **150**, 152-160.
- Nezval, O., Krejza, J., Světlík, J., Šigut, L. & Horáček, P. (2020) Comparison of traditional ground-based observations and digital remote sensing of phenological transitions in a floodplain forest. *Agricultural and Forest Meteorology*, **291**
- Pastorello, G.Z., Papale, D., Chu, H., Trotta, C., Agarwal, D.A., Canfora, E., Baldocchi, D.D. & Torn, M.S. (2017) A new data set to keep a sharper eye on land-air exchanges. In: *Eos*
- Paus, E., Nilsen, J. & Junntila, O. (1986) Bud dormancy and vegetative growth in *Salix-Polaris* as affected by temperature and photoperiod. *Polar Biology*, **6**, 91-95.
- Peñuelas, J., Rutishauser, T. & Filella, I. (2009) Phenology Feedbacks on Climate Change. *Science*, **324**, 887-888.
- Piao, S., Liu, Q., Chen, A., Janssens, I.A., Fu, Y., Dai, J., Liu, L., Lian, X., Shen, M. & Zhu, X. (2019) Plant phenology and global climate change: Current progresses and challenges. *Global Change Biology*, **25**, 1922-1940.
- Piao, S., Ciais, P., Friedlingstein, P., Peylin, P., Reichstein, M., Luyssaert, S., Margolis, H., Fang, J., Barr, A., Chen, A., Grelle, A., Hollinger, D.Y., Laurila, T., Lindroth, A., Richardson, A.D. & Vesala, T. (2008) Net carbon dioxide losses of northern ecosystems in response to autumn warming. *Nature*, **451**, 49-52.
- Ren, J., Campbell, J. & Shao, Y. (2017) Estimation of SOS and EOS for Midwestern US Corn and Soybean Crops. *Remote Sensing*, **9**
- Rennenberg, H., Wildhagen, H. & Ehltig, B. (2010) Nitrogen nutrition of poplar trees. *Plant Biology*, **12**, 275-291.
- Richardson, A.D., Hufkens, K., Milliman, T. & Frolking, S. (2018) Intercomparison of phenological transition dates derived from the PhenoCam Dataset V1.0 and MODIS satellite remote sensing. *Scientific Reports*, **8**
- Richardson, A.D., Keenan, T.F., Migliavacca, M., Ryu, Y., Sonnentag, O. & Toomey, M. (2013) Climate change, phenology, and phenological control of vegetation feedbacks to the climate system. *Agricultural and Forest Meteorology*, **169**, 156-173.
- Sen, P.K. (1968) Estimates of the Regression Coefficient Based on Kendall's Tau. *Journal of the American Statistical Association*, **63**, 1379-1389.
- Seyednasrollah, B., Young, A.M., Hufkens, K., Milliman, T., Friedl, M.A., Frolking, S. & Richardson, A.D. (2019a) Tracking vegetation phenology across diverse biomes using Version 2.0 of the PhenoCam Dataset. *Sci Data*, **6**, 222.
- Seyednasrollah, B., Young, A.M., Hufkens, K., Milliman, T., Friedl, M.A., Frolking, S., Richardson, A.D., Abraha, M., Allen, D.W., Apple, M., Arain, M.A., Baker, J., Baker, J.M., Baldocchi, D., Bernacchi,

- 688 C.J., Bhattacharjee, J., Blanken, P., Bosch, D.D., Boughton, R., Boughton, E.H., Brown, R.F.,  
689 Browning, D.M., Brunsell, N., Burns, S.P., Cavagna, M., Chu, H., Clark, P.E., Conrad, B.J.,  
690 Cremonese, E., Debinski, D., Desai, A.R., Diaz-Delgado, R., Duchesne, L., Dunn, A.L.,  
691 Eissenstat, D.M., El-Madany, T., Ellum, D.S.S., Ernest, S.M., Esposito, A., Fenstermaker, L.,  
692 Flanagan, L.B., Forsythe, B., Gallagher, J., Ganelle, D., Griffis, T., Groffman, P., Gu, L., Guillemot,  
693 J., Halpin, M., Hanson, P.J., Hemming, D., Hove, A.A., Humphreys, E.R., Jaimes-Hernandez, A.,  
694 Jaradat, A.A., Johnson, J., Keel, E., Kelly, V.R., Kirchner, J.W., Kirchner, P.B., Knapp, M.,  
695 Krassovski, M., Langvall, O., Lanthier, G., Maire, G.I., Magliulo, E., Martin, T.A., McNeil, B., Meyer,  
696 G.A., Migliavacca, M., Mohanty, B.P., Moore, C.E., Mudd, R., Munger, J.W., Murrell, Z.E., Nesic,  
697 Z., Neufeld, H.S., O'Halloran, T.L., Oechel, W., Oishi, A.C., Oswald, W.W., Perkins, T.D., Reba,  
698 M.L., Rundquist, B., Runkle, B.R., Russell, E.S., Sadler, E.J., Saha, A., Saliendra, N.Z.,  
699 Schmalbeck, L., Schwartz, M.D., Scott, R.L., Smith, E.M., Sonnentag, O., Stoy, P., Strachan, S.,  
700 Suvocarev, K., Thom, J.E., Thomas, R.Q., Van den berg, A.K., Vargas, R., Verfaillie, J., Vogel,  
701 C.S., Walker, J.J., Webb, N., Wetzel, P., Weyers, S., Whipple, A.V., Whitham, T.G., Wohlfahrt, G.,  
702 Wood, J.D., Wolf, S., Yang, J., Yang, X., Yenni, G., Zhang, Y., Zhang, Q. & Zona, D. (2019b)  
703 PhenoCam Dataset v2.0: Vegetation Phenology from Digital Camera Imagery, 2000-2018. In.  
704 ORNL Distributed Active Archive Center
- 705 Shen, M., Tang, Y., Desai, A.R., Gough, C. & Chen, J. (2014) Can EVI-derived land-surface phenology be  
706 used as a surrogate for phenology of canopy photosynthesis? *International Journal of Remote  
707 Sensing*, **35**, 1162-1174.
- 708 Shen, M.G., Piao, S.L., Jeong, S.J., Zhou, L.M., Zeng, Z.Z., Ciais, P., Chen, D.L., Huang, M.T., Jin, C.S.,  
709 Li, L.Z.X., Li, Y., Myneni, R.B., Yang, K., Zhang, G.X., Zhang, Y.J. & Yao, T.D. (2015) Evaporative  
710 cooling over the Tibetan Plateau induced by vegetation growth. *Proceedings of the National  
711 Academy of Sciences*, **112**, 9299-9304.
- 712 Soudani, K., Delpierre, N., Berveiller, D., Hmimina, G., Pontailler, J.-Y., Seureau, L., Vincent, G. & Dufrêne,  
713 É. (2020) A survey of proximal methods for monitoring leaf phenology in  
714 temperate deciduous forests. *Biogeosciences Discuss. [preprint]*,  
715 <https://doi.org/10.5194/bg-2020-389>, in review,
- 716 Soudani, K., Hmimina, G., Delpierre, N., Pontailler, J.Y., Aubinet, M., Bonal, D., Caquet, B., de Grandcourt,  
717 A., Burban, B., Flechard, C., Guyon, D., Granier, A., Gross, P., Heinesh, B., Longdoz, B., Loustau,  
718 D., Moureaux, C., Ourcival, J.M., Rambal, S., Saint André, L. & Dufrêne, E. (2012) Ground-based  
719 Network of NDVI measurements for tracking temporal dynamics of canopy structure and  
720 vegetation phenology in different biomes. *Remote Sensing of Environment*, **123**, 234-245.
- 721 Stinziano, J.R. & Way, D.A. (2017) Autumn photosynthetic decline and growth cessation in seedlings of  
722 white spruce are decoupled under warming and photoperiod manipulations. *Plant Cell and  
723 Environment*, **40**, 1296-1316.
- 724 Tang, J., Körner , C., Muraoka, H., Piao, S., Shen, M., Thackeray, S.J. & Yang, X. (2016) Emerging  
725 opportunities and challenges in phenology: a review. *Ecosphere*, **7**, e01436.
- 726 Theil, H. (1992) A rank-invariant method of linear and polynomial regression analysis. *Henri Theil's  
727 Contributions to Economics and Econometrics: Econometric Theory and Methodology* (ed. by B.  
728 Raj and J. Koerts), pp. 345-381. Springer Netherlands, Dordrecht.
- 729 Thomas, H. & Stoddart, J.L. (1980) Leaf Senescence. *Annual Review of Plant Physiology and Plant  
730 Molecular Biology*, **31**, 83-111.
- 731 Vermote, E.F. (2015) MOD09CMG MODIS/Terra Surface Reflectance Daily L3 Global 0.05Deg CMG  
732 V006. In: *NASA EOSDIS Land Processes DAAC*

- 733 Viovy, N. (2018) CRUNCEP Version 7 - Atmospheric Forcing Data for the Community Land Model. In:  
734        *Research Data Archive at the National Center for Atmospheric Research, Computational and*  
735        *Information Systems Laboratory*, Boulder CO.
- 736 Wang, C. & Zhu, K. (2019) Misestimation of growing season length due to inaccurate construction of  
737        satellite vegetation index time series. *IEEE Geoscience and Remote Sensing Letters*, **16**,  
738        1185-1189.
- 739 White, M.A., Thornton, P.E. & Running, S.W. (1997) A continental phenology model for monitoring  
740        vegetation responses to interannual climatic variability. *Global Biogeochemical Cycles*, **11**,  
741        217-234.
- 742 Wingate, L., Ogée, J., Cremonese, E., Filippa, G., Mizunuma, T., Migliavacca, M., Moisy, C., Wilkinson, M.,  
743        Moureaux, C., Wohlfahrt, G., Hammerle, A., Hörtnagl, L., Gimeno, C., Porcar-Castell, A.,  
744        Galvagno, M., Nakaji, T., Morison, J., Kolle, O., Knohl, A., Kutsch, W., Kolari, P., Nikinmaa, E.,  
745        Ibrom, A., Gielen, B., Eugster, W., Balzaro, M., Papale, D., Klumpp, K., Köstner, B., Grünwald,  
746        T., Joffre, R., Ourcival, J.M., Hellstrom, M., Lindroth, A., George, C., Longdoz, B., Genty, B.,  
747        Levula, J., Heinesch, B., Sprintsin, M., Yakir, D., Manise, T., Guyon, D., Ahrends, H.,  
748        Plaza-Aguilar, A., Guan, J.H. & Grace, J. (2015) Interpreting canopy development and physiology  
749        using a European phenology camera network at flux sites. *Biogeosciences*, **12**, 5995-6015.
- 750 Xu, C., Liu, H., Williams, A.P., Yin, Y. & Wu, X. (2016) Trends toward an earlier peak of the growing  
751        season in Northern Hemisphere mid-latitudes. *Global Change Biology*, **22**, 2852-2860.
- 752 Yang, X., Tang, J. & Mustard, J.F. (2014) Beyond leaf color: Comparing camera-based phenological  
753        metrics with leaf biochemical, biophysical, and spectral properties throughout the growing season  
754        of a temperate deciduous forest. *Journal of Geophysical Research: Biogeosciences*, **119**,  
755        181-191.
- 756 Yu, H., Luedeling, E. & Xu, J. (2010) Winter and spring warming result in delayed spring phenology on the  
757        Tibetan Plateau. *Proceedings of the National Academy of Sciences*, **107**, 22151-22156.
- 758 Zhang, X. (2015) Reconstruction of a complete global time series of daily vegetation index trajectory from  
759        long-term AVHRR data. *Remote Sensing of Environment*, **156**, 457-472.
- 760 Zhang, X., Tarpley, D. & Sullivan, J.T. (2007) Diverse responses of vegetation phenology to a warming  
761        climate. *Geophysical Research Letters*, **34**
- 762 Zhang, X., Friedl, M.A., Schaaf, C.B., Strahler, A.H., Hodges, J.C., Gao, F., Reed, B.C. & Huete, A. (2003)  
763        Monitoring vegetation phenology using MODIS. *Remote Sensing of Environment*, **84**, 471-475.
- 764 Zhang, X., Jayavelu, S., Liu, L., Friedl, M.A., Henebry, G.M., Liu, Y., Schaaf, C.B., Richardson, A.D. &  
765        Gray, J. (2018) Evaluation of land surface phenology from VIIRS data using time series of  
766        PhenoCam imagery. *Agricultural and Forest Meteorology*, **256-257**, 137-149.
- 767 Zhao, B., Donnelly, A. & Schwartz, M.D. (2020) Evaluating autumn phenology derived from field  
768        observations, satellite data, and carbon flux measurements in a northern mixed forest, USA.  
769        *International Journal of Biometeorology*, **64**, 713-727.
- 770 Zohner, C.M., Benito, B.M., Svenning, J.-C. & Renner, S.S. (2016) Day length unlikely to constrain  
771        climate-driven shifts in leaf-out times of northern woody plants. *Nature Climate Change*, **6**,  
772        1120-1123.
- 773

1

2                   **Supplementary Information for**

3

4     **Warming does not delay the start of autumnal leaf coloration but slows its progress rate**

5

6     **This PDF file includes:**

7

8               Figures S1 to S25

9               Tables S1 to S8

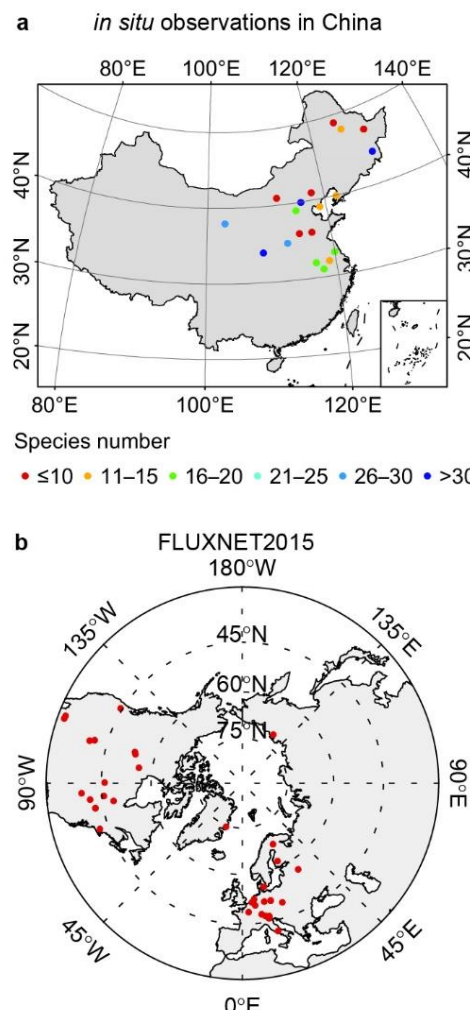
10              Supplementary Methods

11              Supplementary References

12

13    **Supplementary Figures**

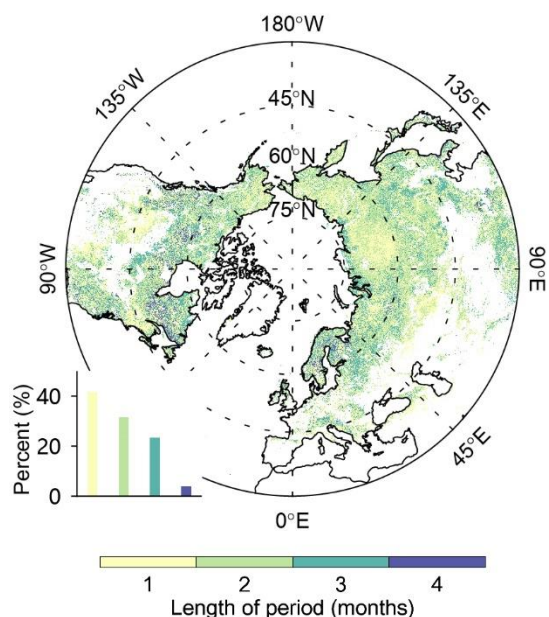
14  
15



16

17    **Figure S1.** Locations of the sites of *in situ* observations used in this study. a, phenological observation  
18    sites in China. b, FLUXNET2015 flux tower sites.

19



20  
21 **Figure S2.** Spatial pattern of the length of the pre- $D_{LCO}$  period for mean daily minimum temperature  
22 ( $T_{\min}$ ). The bar chart shows the percentage of area for each interval of the length of the pre- $D_{LCO}$  period,  
23 with the length indicated by the color scale at the bottom.

24

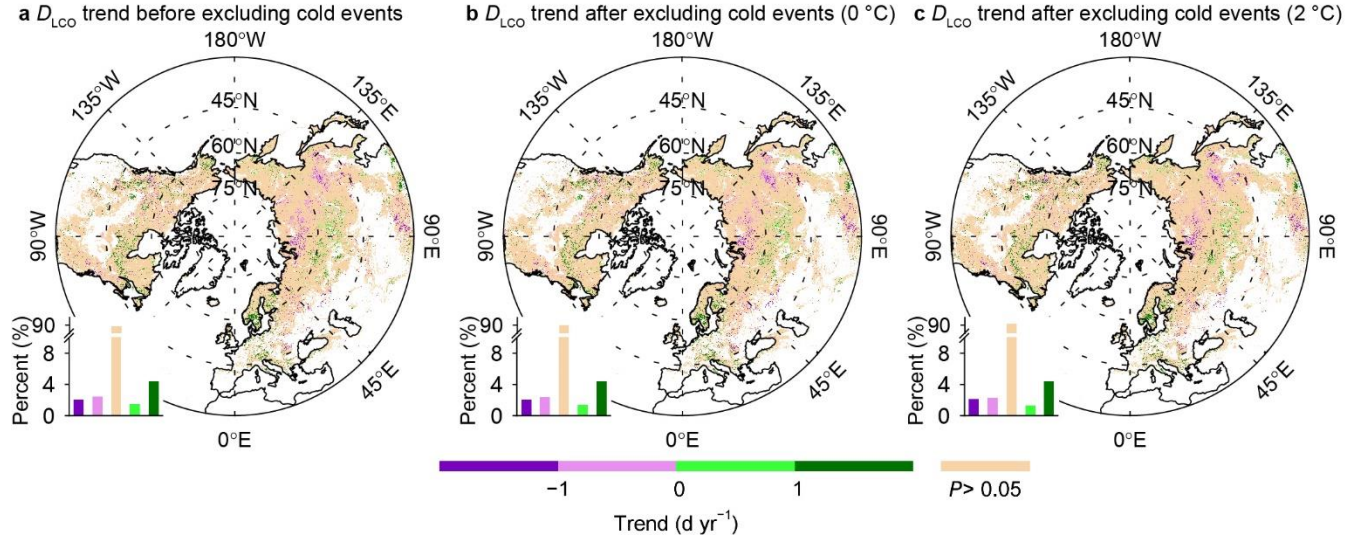
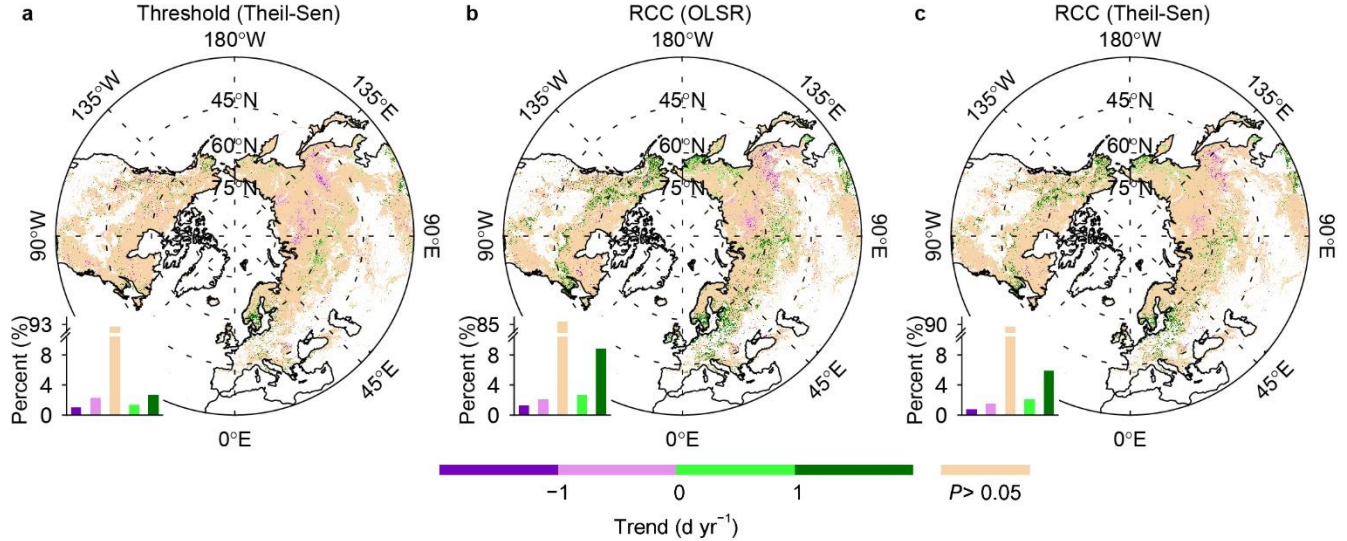
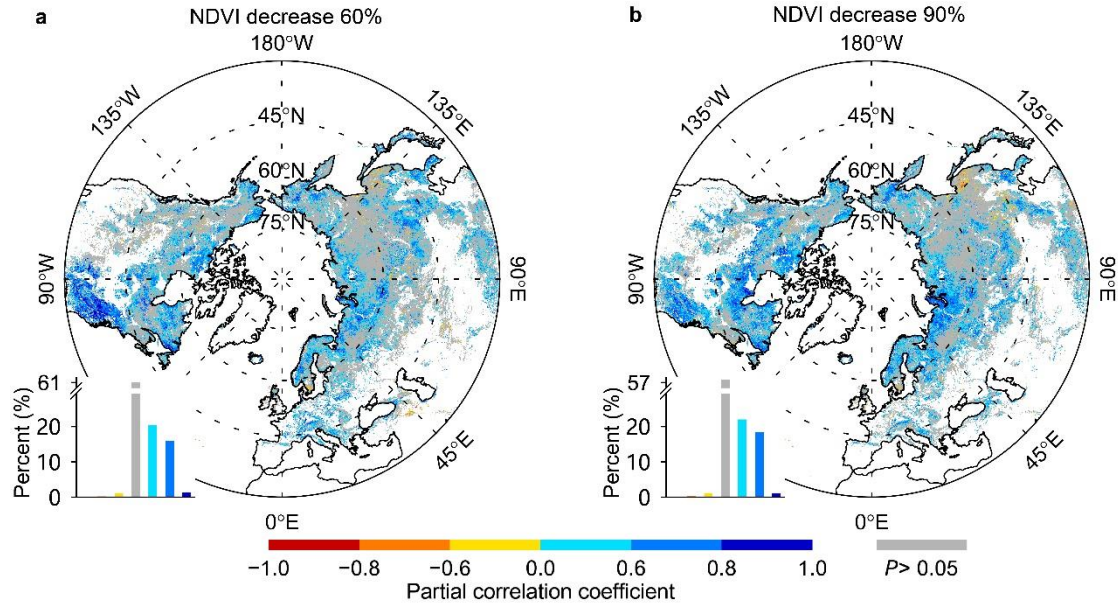


**Figure S3.** Temporal trends in timing of the onset of leaf coloration ( $D_{LCO}$ ), retrieved from satellite images over the period 2000–2016 before (a) and after (b and c) the exclusion of years with cold events before  $D_{LCO}$ . Cold events were determined mainly by using a threshold-based method with daily minimum temperatures of  $0\text{ }^{\circ}\text{C}$  (b) or  $2\text{ }^{\circ}\text{C}$  (c). The bar chart in each panel shows the percentage of area within each interval of the significant ( $P < 0.05$ ) temporal trends and the percentage of area with nonsignificant trends, indicated by the color scale at the bottom. The percentage for each interval of the trend (positive and negative trend values refer to significantly delayed and advanced  $D_{LCO}$ , respectively) is provided in Table S5.  $D_{LCO}$  is defined as the date when NDVI decreases by 10% of its annual amplitude in autumn, on the basis of a generalized sigmoid function fitted from the annual NDVI profile. Significant temporal trends were determined by using *t*-tests at  $P < 0.05$  and ordinary least squares regression between  $D_{LCO}$  and the respective years. Pixels dominated by croplands or with low vegetation coverage, weak seasonality, or peak NDVI in October–April were discarded.

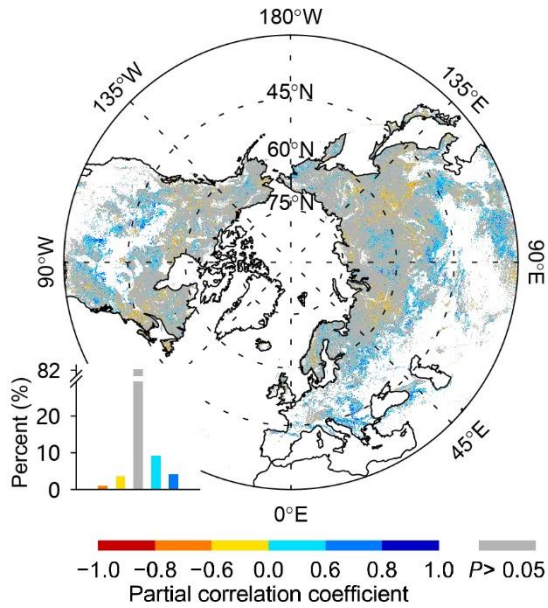


39

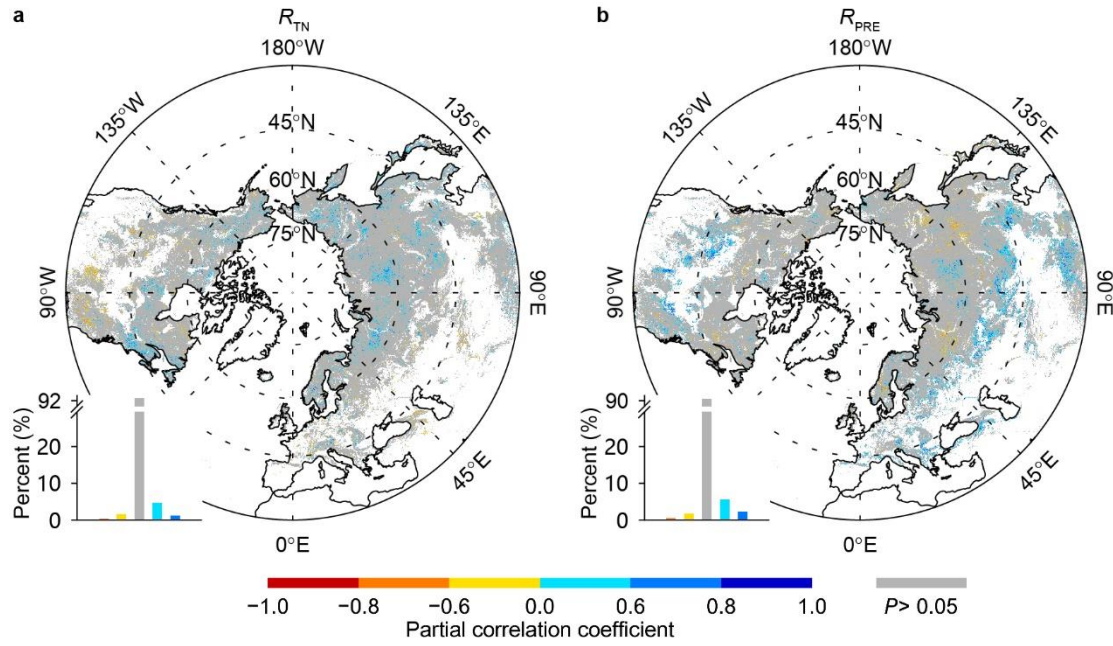
**Figure S4.** Temporal trends in timing of the onset of leaf coloration ( $D_{LCO}$ ), retrieved from satellite images over the period 2000–2018. The bar chart in each panel shows the percentage of area within each interval of the significant ( $P < 0.05$ ) temporal trends and the percentage of area with nonsignificant trends, indicated by the color scale at the bottom. Positive and negative trend values refer to significantly delayed and advanced  $D_{LCO}$ , respectively.  $D_{LCO}$  in (a) was defined as the date when NDVI decreased by 10% of its annual amplitude in each autumn (threshold), on the basis of a generalized sigmoid function fitted from the annual NDVI profile.  $D_{LCO}$  in (b) and (c) was determined as the date when the rate of change of the curvature (RCC) of a double logistic-function-fitted NDVI curve reached its first local minimum value in the descending period. In (a) and (c), significant temporal trends were determined by using Mann-Kendall tests at  $P < 0.05$  and a Theil-Sen estimator between  $D_{LCO}$  and the respective years; in (b), significant temporal trends were determined by using *t*-tests at  $P < 0.05$  and ordinary least squares regression (OLSRL) between  $D_{LCO}$  and respective years. Pixels dominated by croplands or with low vegetation coverage, weak seasonality, or peak NDVI in October–April were discarded.



53  
54 **Figure S5.** Spatial pattern of the partial correlation coefficient between the timing of the end of leaf  
55 coloration ( $D_{LCE}$ ) and pre- $D_{LCE}$   $T_{min}$  over the period 2000–2018.  $D_{LCE}$  was determined as the date when  
56 NDVI drops by 60% (a) and 90% (b), respectively. The bar chart in the bottom-left corner shows the  
57 percentage of area for each interval of the partial correlation coefficient, with the coefficient values  
58 indicated by the color scale at the bottom. Non-significant correlations ( $P > 0.05$ ) are in gray.  
59  
60



61  
62 **Figure S6.** Spatial pattern of the partial correlation coefficient between the timing of onset of leaf  
63 coloration ( $D_{LCO}$ ) and pre- $D_{LCO}$  total precipitation over the period 2000–2018. The bar chart in the  
64 bottom-left corner shows the percentage of area for each interval of the partial correlation coefficient,  
65 with the coefficient values indicated by the color scale at the bottom. Non-significant correlations ( $P >$   
66  $0.05$ ) are in gray, and the percentage for each interval is provided in Table 1.  
67



68

69

70

71

72

73

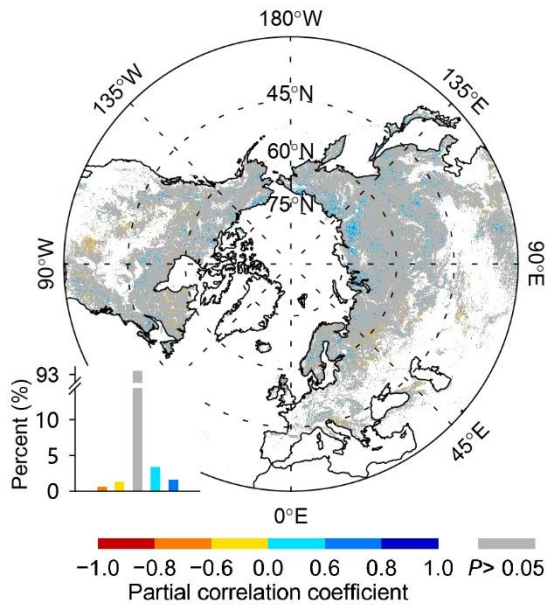
74

75

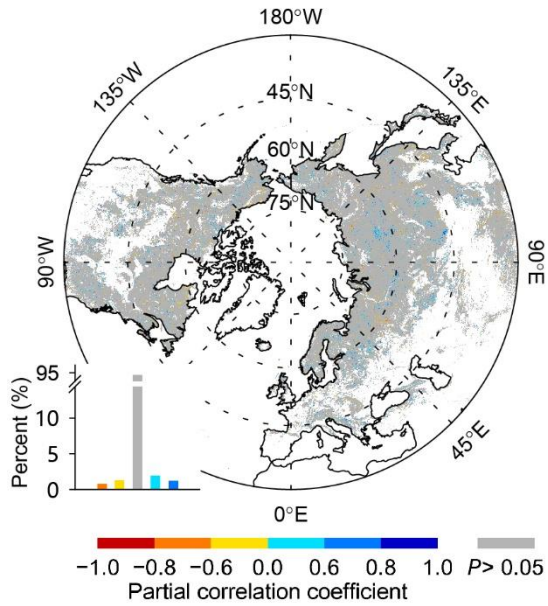
76

77

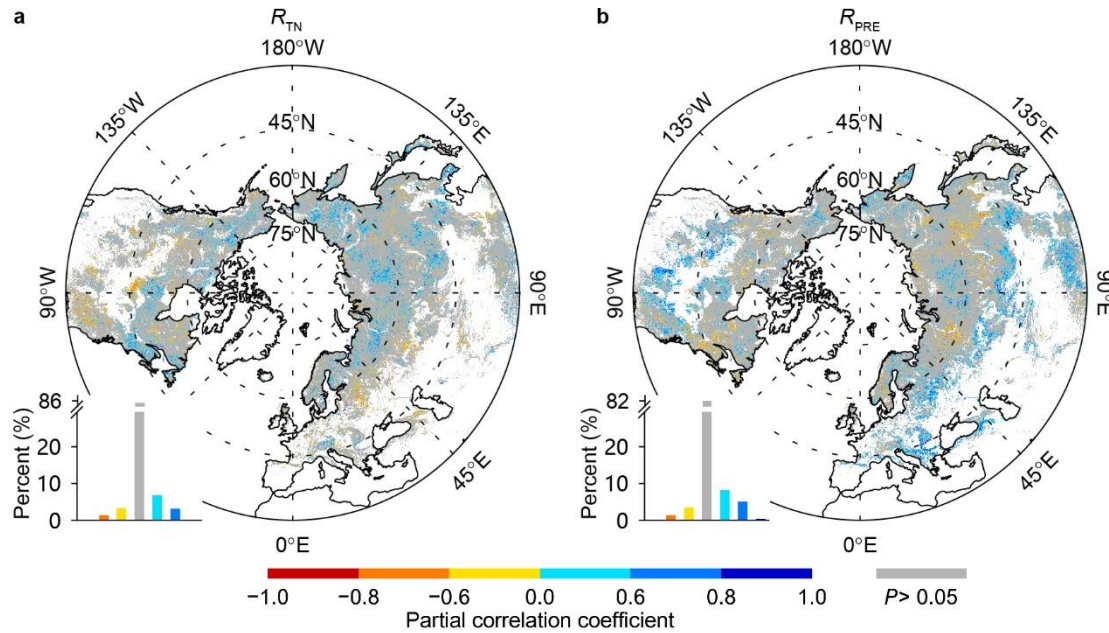
**Figure S7.** Spatial pattern of the partial correlation coefficient between the timing of onset of leaf coloration ( $D_{LCO}$ ) and pre- $D_{LCO}$  (1 month preceding the multiyear mean  $D_{LCO}$ ) climatic factors over the period 2000–2018. a, Spatial pattern of the partial correlation coefficient ( $R_{TN}$ ) between  $D_{LCO}$  and pre- $D_{LCO}$  mean daily minimum temperature ( $T_{min}$ ) while controlling for the corresponding total precipitation. b, Spatial pattern of the partial correlation coefficient ( $R_{PRE}$ ) between  $D_{LCO}$  and pre- $D_{LCO}$  total precipitation while controlling for the corresponding  $T_{min}$ . The bar chart in each panel shows the percentage of area for each interval of the partial correlation coefficient, with the coefficient value indicated by the color scale at the bottom. Non-significant correlations ( $P > 0.05$ ) are in gray.



78  
 79 **Figure S8.** Spatial pattern of the partial correlation coefficient between the timing of onset of leaf  
 80 coloration ( $D_{LCO}$ ) and pre- $D_{LCO}$  (15 days preceding the multiyear mean  $D_{LCO}$ ) mean daily minimum  
 81 temperature while controlling for the corresponding total precipitation over the period 2000–2016. The  
 82 bar chart shows the percentage of area for each interval of partial correlation coefficient, with the  
 83 coefficient value indicated by the color scale at the bottom. Non-significant correlations ( $P > 0.05$ ) are in  
 84 gray. Daily minimum temperature was extracted from the CRU-NCEP 7.2 6-hourly dataset and  
 85 determined as the minimum value of the four 6-hourly minimum temperature values for each day.  
 86



87  
88 **Figure S9.** Spatial pattern of the partial correlation coefficient between the timing of the onset of leaf  
89 coloration ( $D_{LCO}$ ) and the lowest daily minimum temperature ( $T_{min}$ ) during the 15 days before the  
90 multiyear mean  $D_{LCO}$ , with the concurrent mean  $T_{min}$  (mean of the remaining 14  $T_{min}$  values after  
91 removal of the lowest  $T_{min}$  during the period) and total precipitation as control variables over the period  
92 2000–2016. The bar chart shows the percentage of area for each interval of the partial correlation  
93 coefficient ( $P < 0.05$ ), with the coefficient indicated by the color scale at the bottom. Non-significant  
94 correlations ( $P > 0.05$ ) are in gray. Daily minimum temperature was extracted from the CRUNCEP 7.2  
95 6-hourly dataset and determined as the minimum value of the four 6-hourly minimum temperature  
96 values for each day.  
97



98

99

100

101

102

103

104

105

106

107

108

109

110

111

112

113

114

115

116

117

118

119

120

121

122

123

124

125

126

127

128

129

130

131

132

133

134

135

136

137

138

139

140

141

142

143

144

145

146

147

148

149

150

151

152

153

154

155

156

157

158

159

160

161

162

163

164

165

166

167

168

169

170

171

172

173

174

175

176

177

178

179

180

181

182

183

184

185

186

187

188

189

190

191

192

193

194

195

196

197

198

199

200

201

202

203

204

205

206

207

208

209

210

211

212

213

214

215

216

217

218

219

220

221

222

223

224

225

226

227

228

229

230

231

232

233

234

235

236

237

238

239

240

241

242

243

244

245

246

247

248

249

250

251

252

253

254

255

256

257

258

259

260

261

262

263

264

265

266

267

268

269

270

271

272

273

274

275

276

277

278

279

280

281

282

283

284

285

286

287

288

289

290

291

292

293

294

295

296

297

298

299

300

301

302

303

304

305

306

307

308

309

310

311

312

313

314

315

316

317

318

319

320

321

322

323

324

325

326

327

328

329

330

331

332

333

334

335

336

337

338

339

340

341

342

343

344

345

346

347

348

349

350

351

352

353

354

355

356

357

358

359

360

361

362

363

364

365

366

367

368

369

370

371

372

373

374

375

376

377

378

379

380

381

382

383

384

385

386

387

388

389

390

391

392

393

394

395

396

397

398

399

400

401

402

403

404

405

406

407

408

409

410

411

412

413

414

415

416

417

418

419

420

421

422

423

424

425

426

427

428

429

430

431

432

433

434

435

436

437

438

439

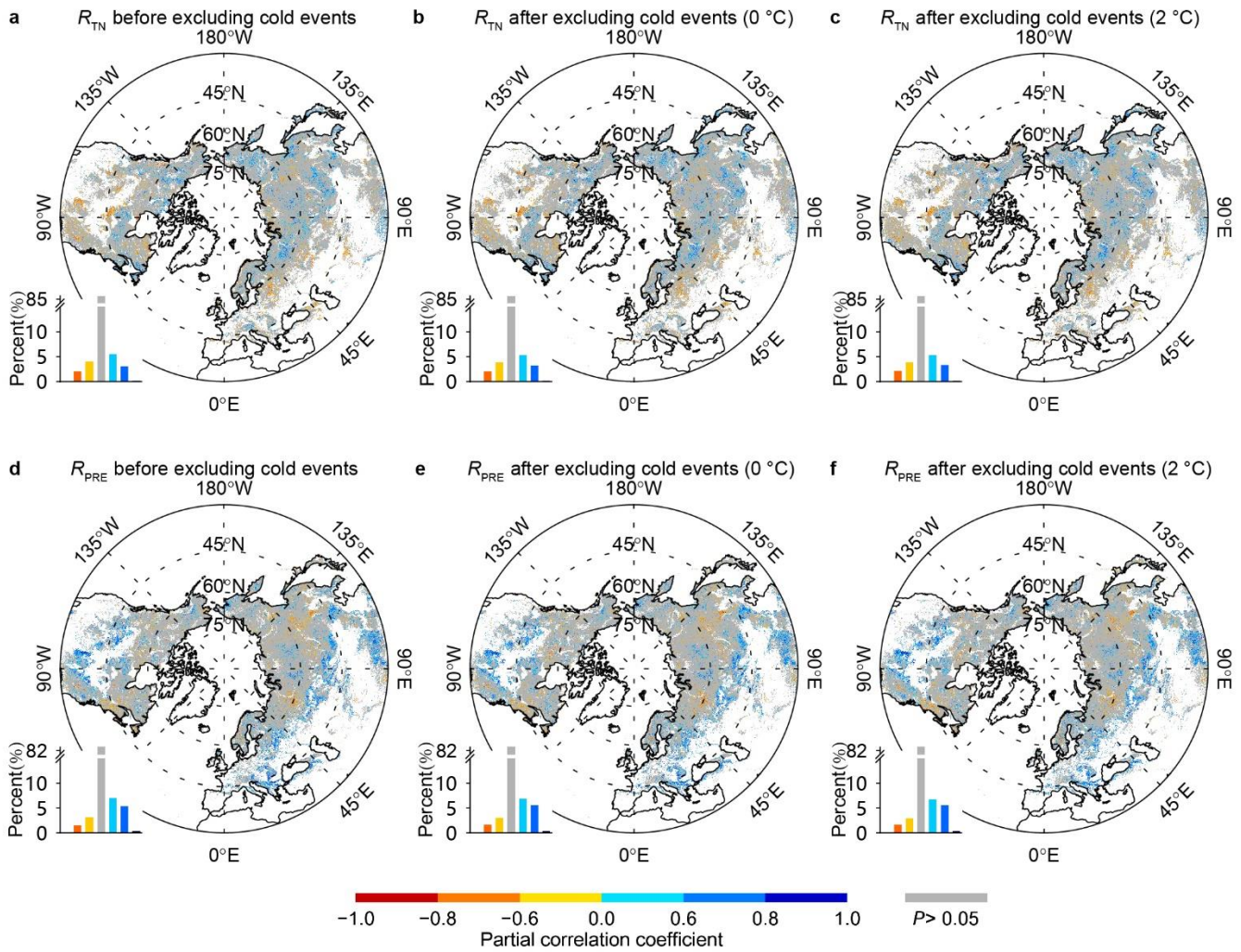
440

441

442

443

444&lt;/



109

110

111

112

113

114

115

116

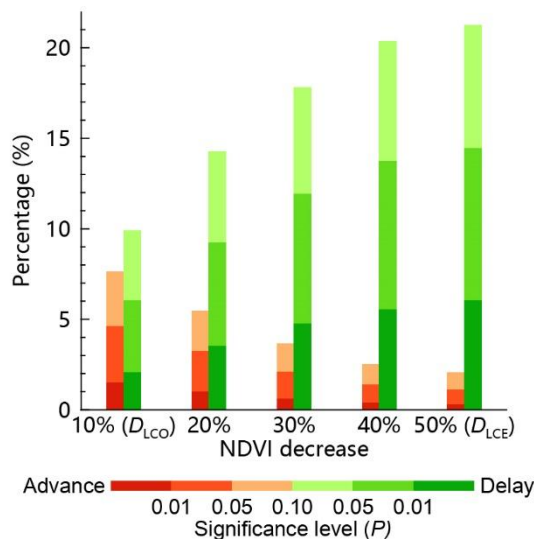
117

118

119

120

**Figure S11.** Spatial pattern of the partial correlation coefficient between the timing of onset of leaf coloration ( $D_{LCO}$ ) and pre- $D_{LCO}$  climatic factors over the period 2000–2016 before and after the exclusion of years with cold events before  $D_{LCO}$ . a–c, Spatial pattern of the partial correlation coefficient ( $R_{TN}$ ) between  $D_{LCO}$  and pre- $D_{LCO}$  mean daily minimum temperature ( $T_{min}$ ) before (a) and after (b and c) the exclusion of years with cold events. d–f, The same as (a–c), but for the partial correlation between  $D_{LCO}$  and pre- $D_{LCO}$  total precipitation ( $R_{PRE}$ ). The bar chart in each panel shows the percentage of area for each interval of the partial correlation coefficient, with the coefficient value indicated by the color scale at the bottom. Non-significant correlations ( $P > 0.05$ ) are in gray, and the percentage for each interval is provided in Table S7. Cold events were determined mainly by using a threshold-based method with a daily minimum temperature of 0 °C (b and e) or 2 °C (c and f).



121

122

123

124

125

126

127

128

129

130

131

132

133

134

135

136

137

138

139

140

141

142

143

144

145

146

147

148

149

150

151

152

153

154

155

156

157

158

159

160

161

162

163

164

165

166

167

168

169

170

171

172

173

174

175

176

177

178

179

180

181

182

183

184

185

186

187

188

189

190

191

192

193

194

195

196

197

198

199

200

201

202

203

204

205

206

207

208

209

210

211

212

213

214

215

216

217

218

219

220

221

222

223

224

225

226

227

228

229

230

231

232

233

234

235

236

237

238

239

240

241

242

243

244

245

246

247

248

249

250

251

252

253

254

255

256

257

258

259

260

261

262

263

264

265

266

267

268

269

270

271

272

273

274

275

276

277

278

279

280

281

282

283

284

285

286

287

288

289

290

291

292

293

294

295

296

297

298

299

300

301

302

303

304

305

306

307

308

309

310

311

312

313

314

315

316

317

318

319

320

321

322

323

324

325

326

327

328

329

330

331

332

333

334

335

336

337

338

339

340

341

342

343

344

345

346

347

348

349

350

351

352

353

354

355

356

357

358

359

360

361

362

363

364

365

366

367

368

369

370

371

372

373

374

375

376

377

378

379

380

381

382

383

384

385

386

387

388

389

390

391

392

393

394

395

396

397

398

399

400

401

402

403

404

405

406

407

408

409

410

411

412

413

414

415

416

417

418

419

420

421

422

423

424

425

426

427

428

429

430

431

432

433

434

435

436

437

438

439

440

441

442

443

444

445

446

447

448

449

450

451

452

453

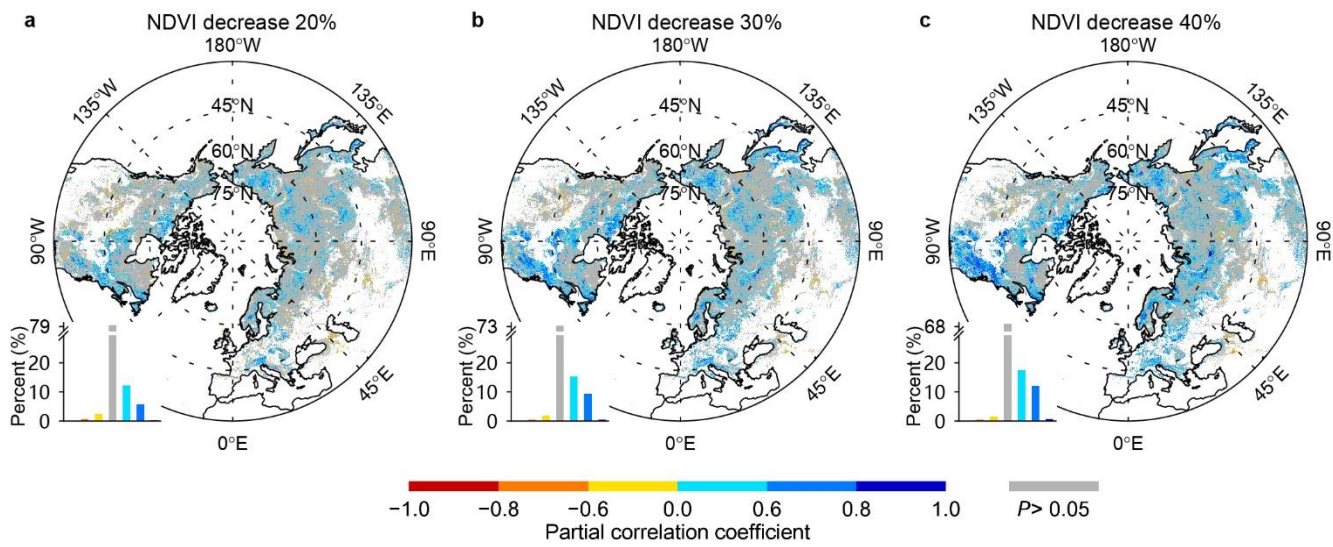
454

455

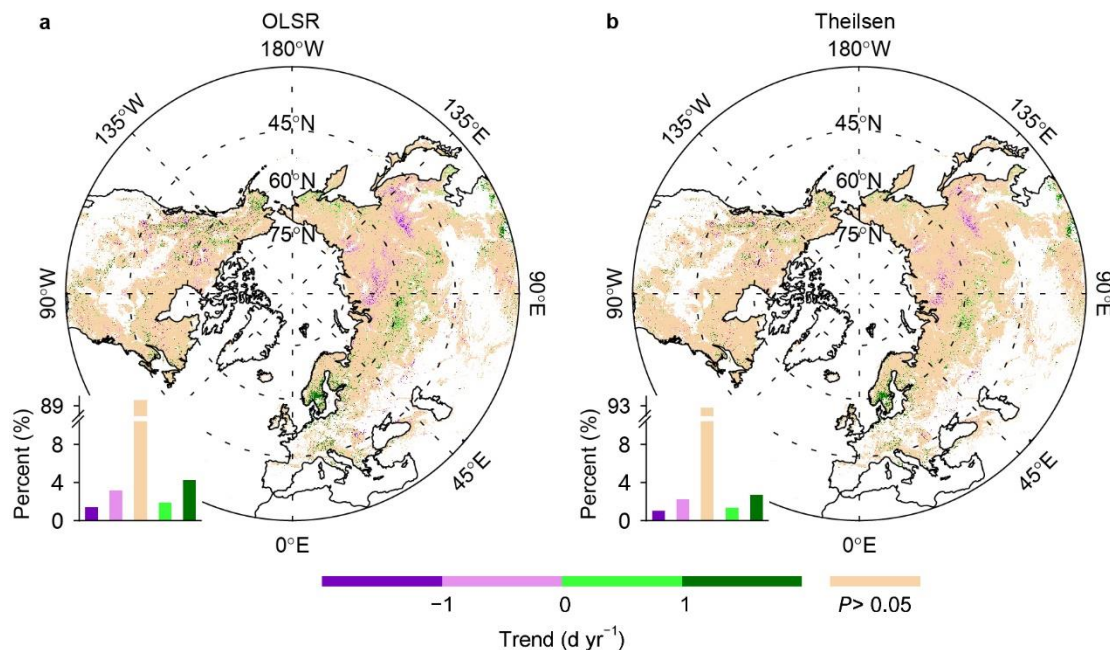
456

457

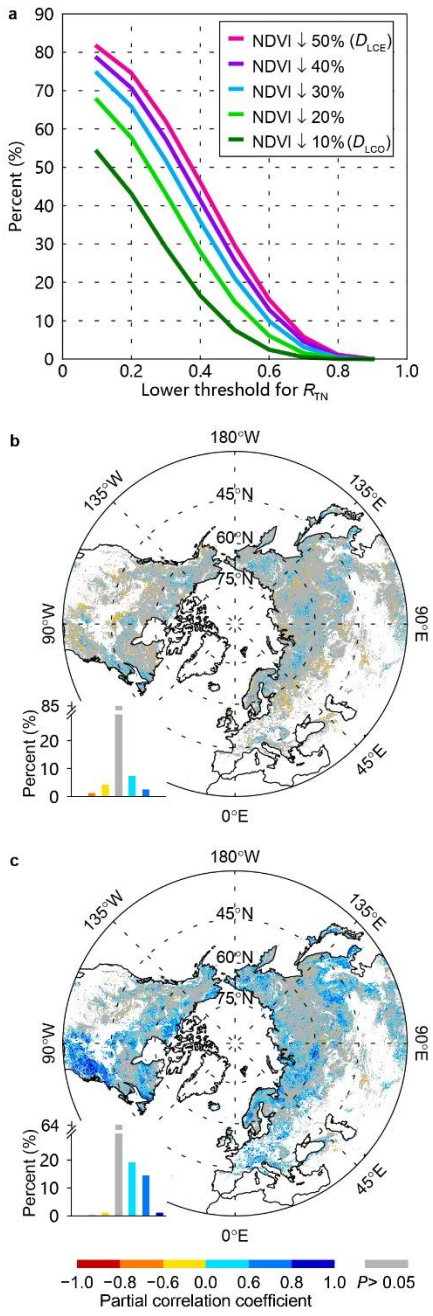
458



131 **Figure S13.** Spatial pattern of the partial correlation coefficient between the timing of different stages of  
 132 leaf coloration and the mean daily minimum temperature for an optimized period preceding each stage  
 133 for 2000–2018. The timings of different stages of leaf coloration are determined as the first dates when  
 134 NDVI decreased by 20% (a), 30% (b), or 40% (c) of its annual amplitude in autumn. The bar chart in  
 135 each panel shows the percentage of area for each interval of the partial correlation coefficient, with the  
 136 coefficient value indicated by the color scale at the bottom. Non-significant correlations ( $P > 0.05$ ) are in  
 137 gray.



141  
142 **Figure S14.** Temporal trends in the timing of onset of leaf coloration ( $D_{LCO}$ ), retrieved from satellite  
143 images for 2000–2018. The bar chart in each panel shows the percentage of area within each interval of  
144 the significant ( $P < 0.05$ ) temporal trends and the percentage of area with nonsignificant trends,  
145 indicated by the color scale at the bottom. Positive and negative trend values refer to significantly  
146 delayed and advanced  $D_{LCO}$ , respectively. For the pixels identified as deciduous broadleaved forests,  
147  $D_{LCO}$  was defined as the date when NDVI decreased by 10% of its annual amplitude from 1 August on  
148 the basis of a generalized sigmoid function fitted from the annual NDVI profile; the maximum value  
149 used to determine the annual amplitude was defined as the mean value of the upper quartile of the fitted  
150 NDVI values in August. For the other pixels,  $D_{LCO}$  was defined as the date when NDVI decreased by 10%  
151 of its annual amplitude; the maximum value of the fitted curve was used to determine the annual  
152 amplitude. In (a), significant temporal trends were determined by using *t*-tests at  $P < 0.05$  and OLSR  
153 between  $D_{LCO}$  and the respective years. In (b), significant temporal trends were determined by using  
154 Mann-Kendall tests at  $P < 0.05$  and a Theil-Sen estimator between  $D_{LCO}$  and the respective years. Pixels  
155 dominated by croplands or with low vegetation coverage, weak seasonality, or peak NDVI in October–  
156 April were discarded.



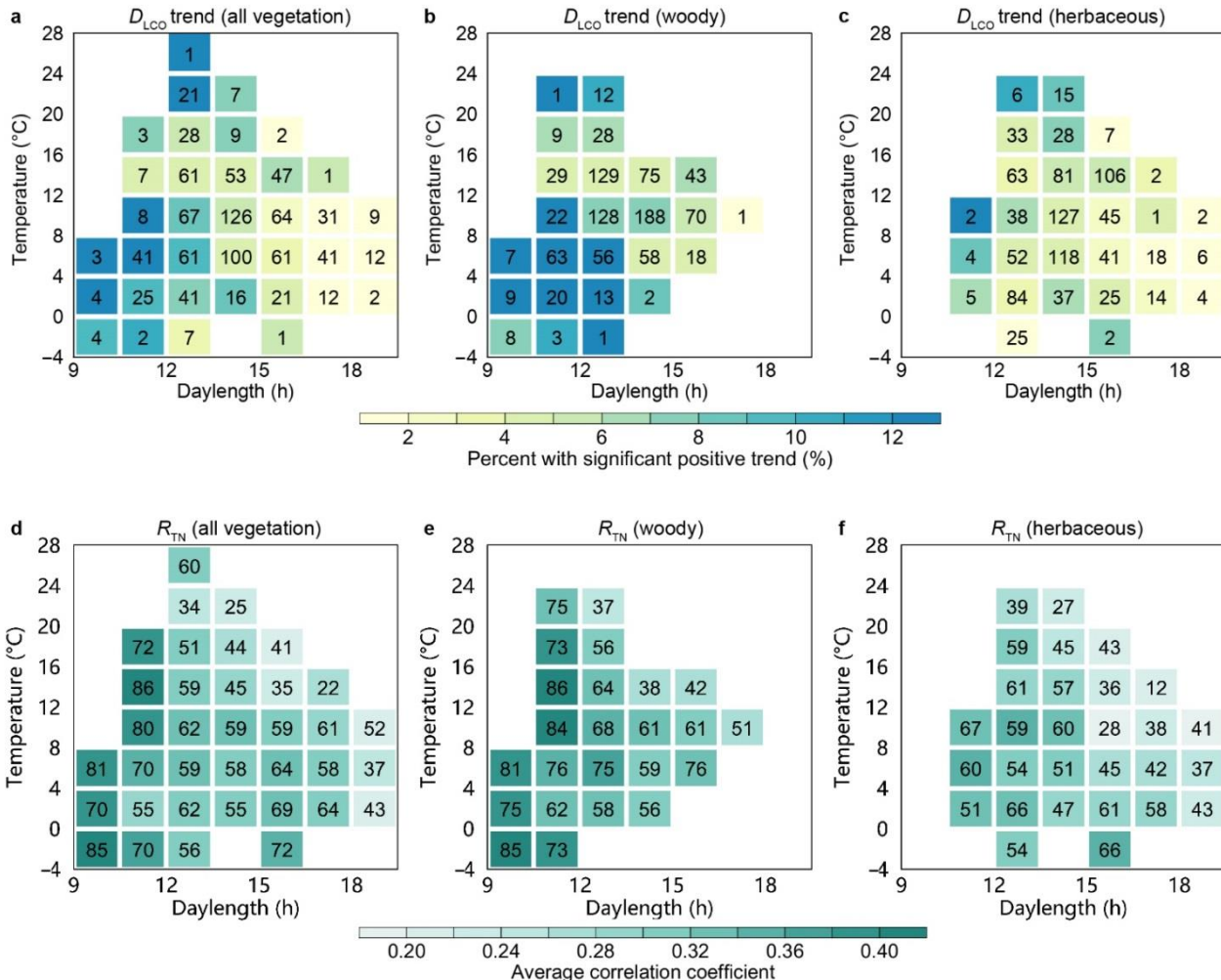
158

159

**Figure S15.** Relationships between the timing of different stages of leaf coloration, as retrieved from satellite images, and the mean daily minimum temperature ( $T_{\min}$ ) for an optimized period preceding the respective stage over the period 2000–2018. a, Percentage of area for which the partial correlation coefficient ( $R_{TN}$ ) between the timing of a certain stage of leaf coloration (defined by NDVI decrease) and  $T_{\min}$  for an optimized period preceding the stage was higher than a certain threshold indicated by the horizontal axis. For example,  $R_{TN}$  for the onset of leaf coloration ( $D_{LCO}$ , 10% decrease in NDVI) is higher than 0.2 in about 40% of the area. b, Spatial pattern of the partial correlation coefficient between

166  $D_{LCO}$  and pre- $D_{LCO} T_{\min}$ . c, Spatial pattern of the partial correlation coefficient between timing of the end  
167 of leaf coloration ( $D_{LCE}$ , 50% decrease in NDVI) and pre- $D_{LCE} T_{\min}$ . For pixels identified as deciduous  
168 broadleaved forests,  $D_{LCO}$  was defined as the date when NDVI decreased by 10% of its annual  
169 amplitude from 1 August on the basis of a generalized sigmoid function fitted from the annual NDVI  
170 profile. The maximum value used to determine the annual amplitude was defined as the mean value of  
171 the upper quartile of the fitted NDVI values in August. For the other pixels,  $D_{LCO}$  was defined as the  
172 date when NDVI decreased by 10% of its annual amplitude; the maximum value of the fitted curve was  
173 used to determine the annual amplitude. The bar charts in (b) and (c) show the percentage of area for  
174 each interval of the partial correlation coefficient ( $P < 0.05$ ), with the coefficient indicated by the color  
175 scale at the bottom. Nonsignificant correlations ( $P > 0.05$ ) are in gray. Pixels dominated by croplands or  
176 with low vegetation coverage, weak seasonality, or peak NDVI in October–April were discarded.

177

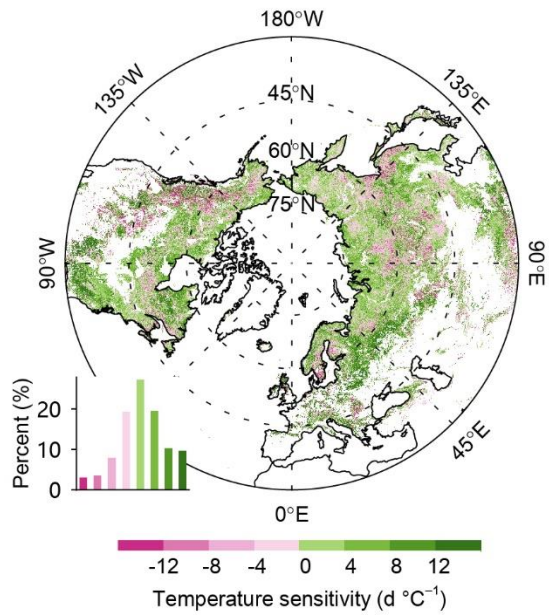


178

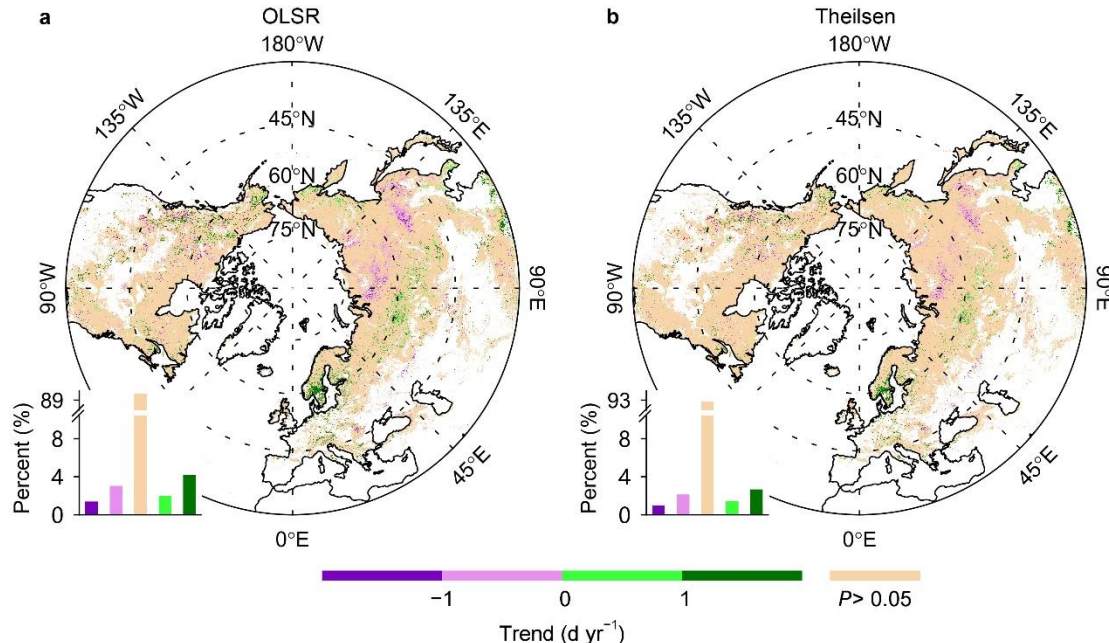
179 **Figure S16.** Dependence of temporal trends in the timing of onset of leaf coloration ( $D_{LCO}$ , a–c) and of  
 180 the partial correlation coefficient ( $R_{TN}$ , d–f) between  $D_{LCO}$  and pre- $D_{LCO}$  mean daily minimum  
 181 temperature ( $T_{min}$ ) on daylength and temperature at  $D_{LCO}$  over the period 2000–2018. Daylength  
 182 (indicated by the horizontal axis) was calculated for each pixel (location) at multiyear mean  $D_{LCO}$  over  
 183 the period 2000–2018 ( $D_{LCO\text{-MEAN}}$ ), and temperature (indicated by the vertical axis) is the mean daily  
 184 minimum temperature of the month preceding  $D_{LCO\text{-MEAN}}$ . a, Color indicates the percentage of area with  
 185 significant ( $P < 0.05$ )  $D_{LCO}$  delays in each cell (i.e., a specific temperature  $\times$  daylength combination), as  
 186 indicated by the color scale at the bottom. The number in each cell indicates the ratio (unit: %) of the  
 187 area in each cell to the total area with  $D_{LCO}$  retrieval (i.e., Northern Hemisphere from  $30^{\circ}\text{N}$ – $75^{\circ}\text{N}$ ). The  
 188 temporal trends and their significances were determined by ordinary least squares regression and  $t$ -tests.  
 189 b and c, The same as (a) but for woody and herbaceous vegetation, respectively. d, Color indicates the  
 190 average of the positive  $R_{TN}$ . The number indicates the percentage of area with a positive correlation in  
 191 each cell, as indicated by the color scale at the bottom. e and f, The same as (d) but for woody and

192 herbaceous vegetation, respectively. For the pixels identified as deciduous broadleaved forests,  $D_{LCO}$   
193 was defined as the date when NDVI decreased by 10% of its annual amplitude from 1 August on the  
194 basis of a generalized sigmoid function fitted from the annual NDVI profile. The maximum value used  
195 to determine the annual amplitude was defined as the mean value of the upper quartile of the fitted  
196 NDVI values in August. For the other pixels,  $D_{LCO}$  was defined as the date when NDVI decreased by 10%  
197 of its annual amplitude; the maximum value of the fitted curve was used to determine the annual  
198 amplitude. Each cell represents 4 °C of temperature and 1.5 h of daylength. Only cells where the ratio of  
199 the area of the cell to the total area is >1‰ are represented. Woody and herbaceous vegetation are  
200 merged from Classes 1–6 and Class 10, respectively, in the MODIS land-cover product (MCD12C1,  
201 Version 6) for 2009.

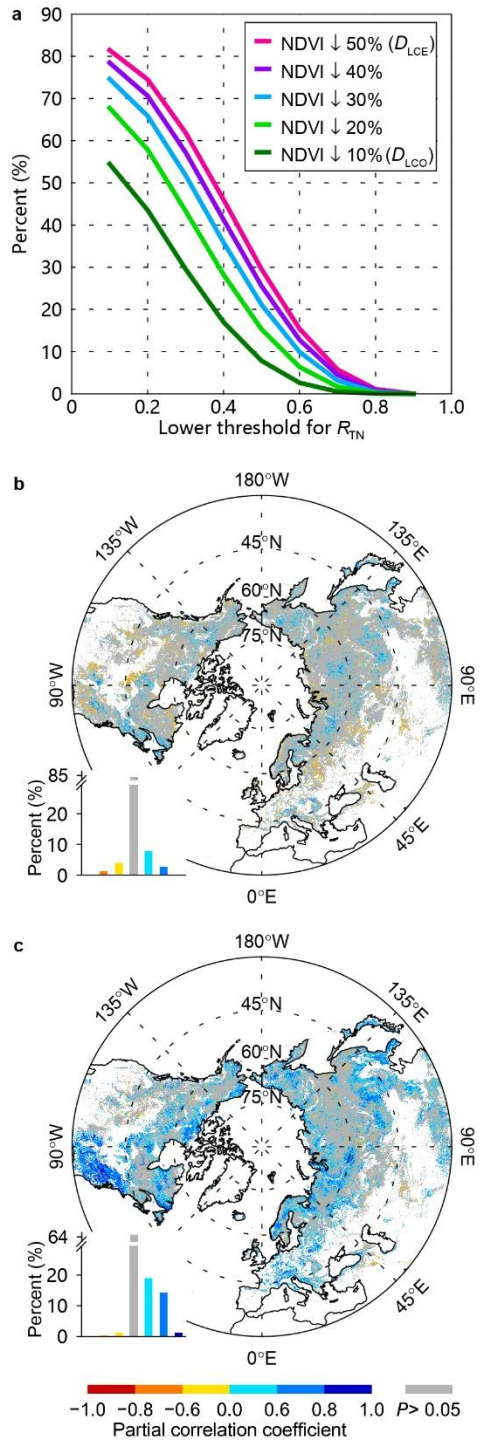
202



203  
 204 **Figure S17.** Difference in temperature sensitivity between the end and the onset of leaf coloration ( $D_{LCE}$   
 205 and  $D_{LCO}$ ) over the period 2000–2018. The temperature sensitivity of  $D_{LCO}$  was defined as the  
 206 coefficient for pre- $D_{LCO}$  mean daily minimum temperature ( $T_{min}$ ) in a linear regression in which  $D_{LCO}$   
 207 was set as the dependent variable and pre- $D_{LCO}$   $T_{min}$  and pre- $D_{LCO}$  total precipitation were independent  
 208 variables. The temperature sensitivity of  $D_{LCE}$  was calculated in a similar way.  $D_{LCO}$  and  $D_{LCE}$  were  
 209 determined as the dates when NDVI decreased by 10% and 50%, respectively, of its annual amplitude  
 210 based on a generalized sigmoid function fitted from the annual NDVI profile. For the pixels identified as  
 211 deciduous broadleaved forests,  $D_{LCO}$  was defined as the date when NDVI decreased by 10% of its  
 212 annual amplitude from 1 August, on the basis of a generalized sigmoid function fitted from the annual  
 213 NDVI profile. The maximum value used to determine the annual amplitude was defined as the mean  
 214 value of the upper quartile of the fitted NDVI values in August. For the other pixels,  $D_{LCO}$  was defined  
 215 as the date when NDVI decreased by 10% of its annual amplitude; the maximum value of the fitted  
 216 curve was used to determine the annual amplitude. The bar chart in the bottom-left corner shows the  
 217 percentage of area for each interval of the temperature sensitivity indicated by the color scale at the  
 218 bottom. Negative values (pink) indicate that  $D_{LCO}$  was more sensitive than  $D_{LCE}$  to temperature.  
 219



220  
 221 **Figure S18.** Temporal trends in the timing of onset of leaf coloration ( $D_{LCO}$ ), as retrieved from satellite  
 222 images for the period 2000–2018. The bar chart in each panel shows the percentage of area within each  
 223 interval of the significant ( $P < 0.05$ ) temporal trends and the percentage of area with nonsignificant  
 224 trends, indicated by the color scale at the bottom. Positive and negative trend values refer to significantly  
 225 delayed and advanced  $D_{LCO}$ , respectively. For the pixels identified as deciduous broadleaved forests,  
 226  $D_{LCO}$  was defined as the date when NDVI decreased by 10% of its annual amplitude from 16 August, on  
 227 the basis of a generalized sigmoid function fitted from the annual NDVI profile. The maximum value  
 228 used to determine the annual amplitude was defined as the mean value of the upper quartile of the fitted  
 229 NDVI values in the second half of August. For the other pixels,  $D_{LCO}$  was defined as the date when  
 230 NDVI decreased by 10% of its annual amplitude; the maximum value of the fitted curve was used to  
 231 determine the annual amplitude. In (a), significant temporal trends were determined by using *t*-tests at  $P$   
 232 < 0.05 and OLSR between  $D_{LCO}$  and respective years. In (b), significant temporal trends were  
 233 determined by using Mann-Kendall tests at  $P < 0.05$  and a Theil-Sen estimator between  $D_{LCO}$  and the  
 234 respective years. Pixels dominated by croplands or with low vegetation coverage, weak seasonality, or  
 235 peak NDVI in October–April were discarded.  
 236



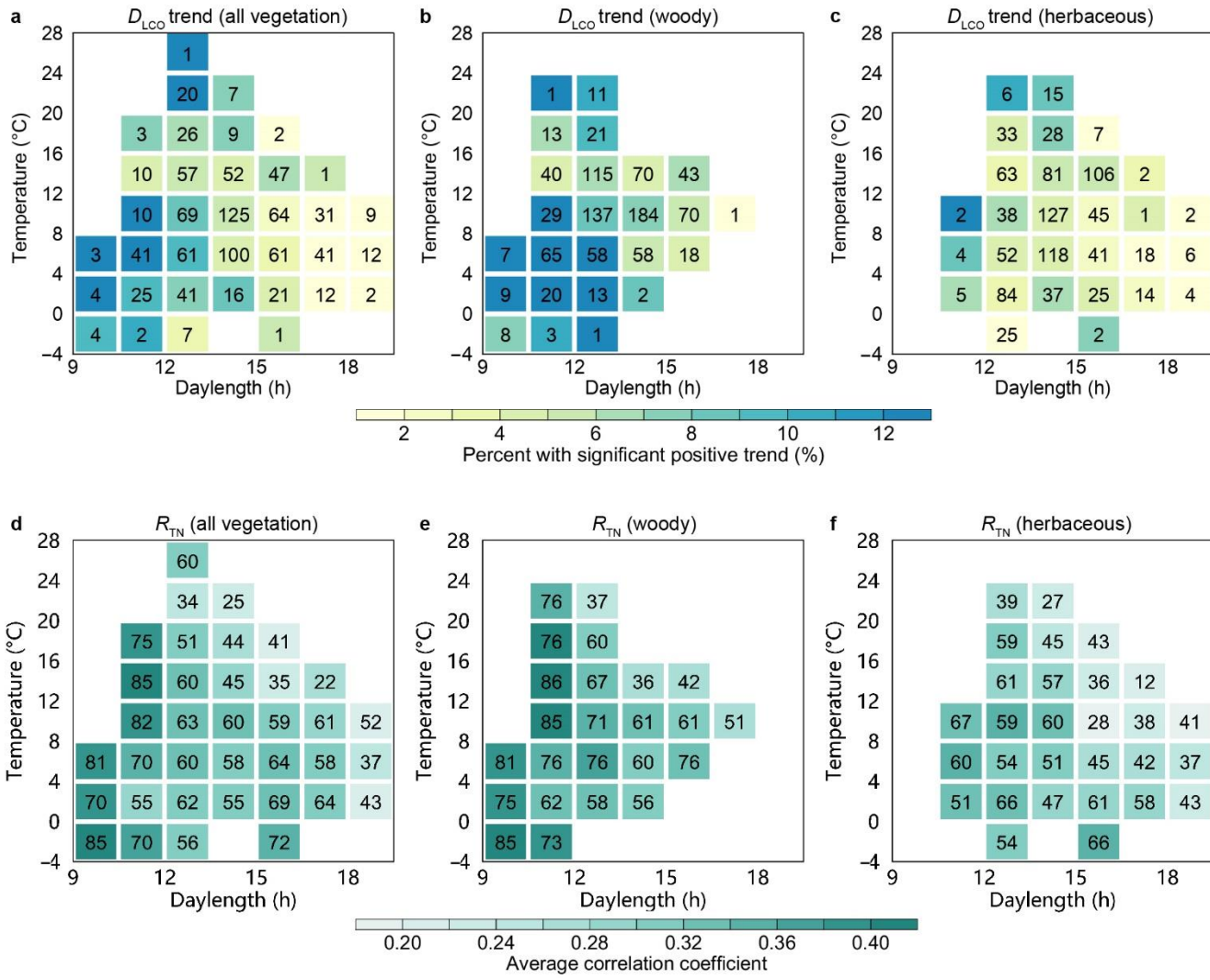
237

238

**Figure S19.** Relationships between the timing of different stages of leaf coloration, as retrieved from satellite images, and the mean daily minimum temperature ( $T_{\min}$ ) for an optimized period preceding the respective stage over the period 2000–2018. a, Percentage of area for which the partial correlation coefficient ( $R_{TN}$ ) between the timing of a given stage of leaf coloration (defined by NDVI decrease) and  $T_{\min}$  for an optimized period preceding the stage was higher than a given threshold, indicated by the

243 horizontal axis. For example,  $R_{TN}$  for the onset of leaf coloration ( $D_{LCO}$ , 10% decrease in NDVI) is  
244 higher than 0.2 in about 40% of the area. b, Spatial pattern of the partial correlation coefficient between  
245  $D_{LCO}$  and pre- $D_{LCO} T_{min}$ . c, Spatial pattern of the partial correlation coefficient between timing of the end  
246 of leaf coloration ( $D_{LCE}$ , 50% decrease in NDVI) and pre- $D_{LCE} T_{min}$ . For the pixels identified as  
247 deciduous broadleaved forests,  $D_{LCO}$  was defined as the date when NDVI decreased by 10% of its  
248 annual amplitude from 16 August, on the basis of a generalized sigmoid function fitted from the annual  
249 NDVI profile. The maximum value used to determine the annual amplitude was defined as the mean  
250 value of the upper quartile of the fitted NDVI values in the second half of August. For the other pixels,  
251  $D_{LCO}$  was defined as the date when NDVI decreased by 10% of its annual amplitude; the maximum  
252 value of the fitted curve was used to determine the annual amplitude. The bar charts in (b) and (c) show  
253 the percentage of area for each interval of the partial correlation coefficient ( $P < 0.05$ ), with the  
254 coefficient indicated by the color scale at the bottom. Non-significant correlations ( $P > 0.05$ ) are in gray.  
255 Pixels dominated by croplands or with low vegetation coverage, weak seasonality, or peak NDVI in  
256 October–April were discarded.

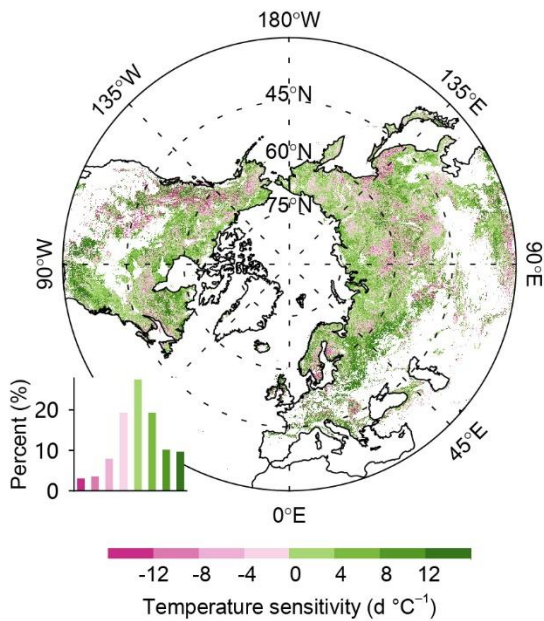
257



258  
259 **Figure S20.** Dependence of temporal trends in the timing of onset of leaf coloration ( $D_{LCO}$ , a–c) and of  
260 the partial correlation coefficient ( $R_{TN}$ , d–f) between  $D_{LCO}$  and pre- $D_{LCO}$  mean daily minimum  
261 temperature ( $T_{\min}$ ) on daylength and temperature at  $D_{LCO}$  over the period 2000–2018. Daylength  
262 (indicated by the horizontal axis) was calculated for each pixel (location) at multiyear mean  $D_{LCO}$  over  
263 the period 2000–2018 ( $D_{LCO\text{-MEAN}}$ ), and temperature (indicated by the vertical axis) is the mean daily  
264 minimum temperature of the month preceding  $D_{LCO\text{-MEAN}}$ . a, Color indicates the percentage of area with  
265 significant ( $P < 0.05$ )  $D_{LCO}$  delays in each cell (i.e., a specific temperature  $\times$  daylength combination), as  
266 indicated by the color scale at the bottom. The number in each cell indicates the ratio (unit: %) of the  
267 area in each cell to the total area with  $D_{LCO}$  retrieval (i.e., Northern Hemisphere from  $30^{\circ}\text{N}$ – $75^{\circ}\text{N}$ ). The  
268 temporal trends and their significances were determined by ordinary least squares regression and  $t$ -tests.  
269 b and c, The same as (a) but for woody and herbaceous vegetation, respectively. d, Color indicates the  
270 average of the positive  $R_{TN}$ , as indicated by the color scale at the bottom. The number indicates the

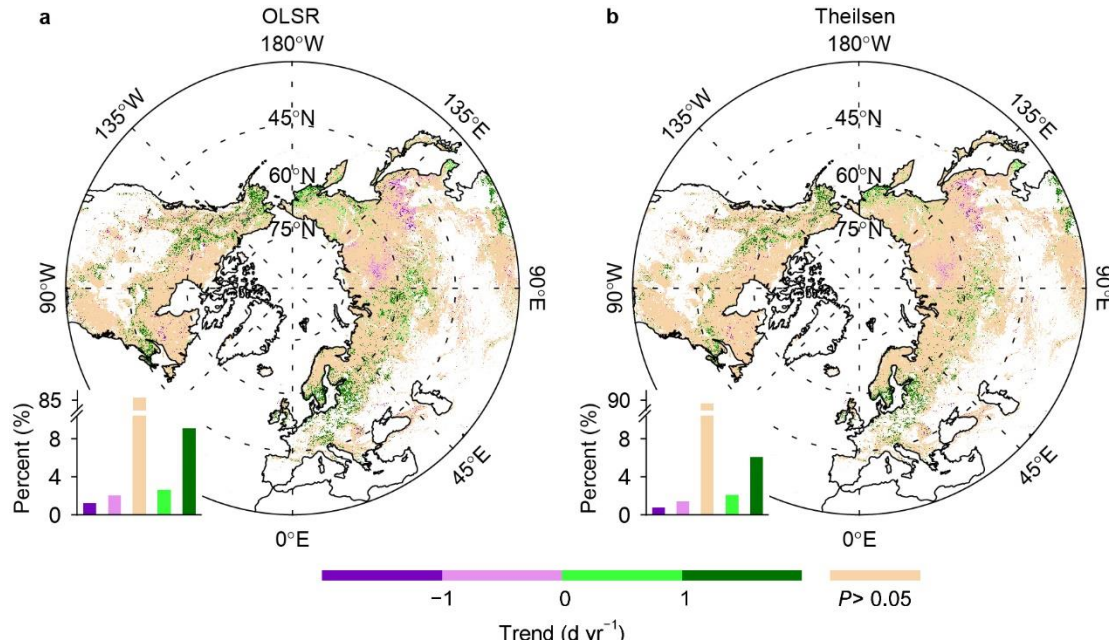
percentage of area with a positive correlation in each cell. e and f, The same as (d) but for woody and herbaceous vegetation, respectively. For the pixels identified as deciduous broadleaved forests,  $D_{LCO}$  was defined as the date when NDVI decreased by 10% of its annual amplitude from 16 August, on the basis of a generalized sigmoid function fitted from the annual NDVI profile. The maximum value used to determine the annual amplitude was defined as the mean value of the upper quartile of the fitted NDVI values in the second half of August. For the other pixels,  $D_{LCO}$  was defined as the date when NDVI decreased by 10% of its annual amplitude; the maximum value of the fitted curve was used to determine the annual amplitude. Each cell represents 4 °C of temperature and 1.5 h of daylength. Only cells where the ratio of the area of the cell to the total area is >1‰ are represented. Woody and herbaceous vegetation are merged from Classes 1–6 and Class 10, respectively, in the MODIS land-cover product (MCD12C1, Version 6) for 2009.

282  
283

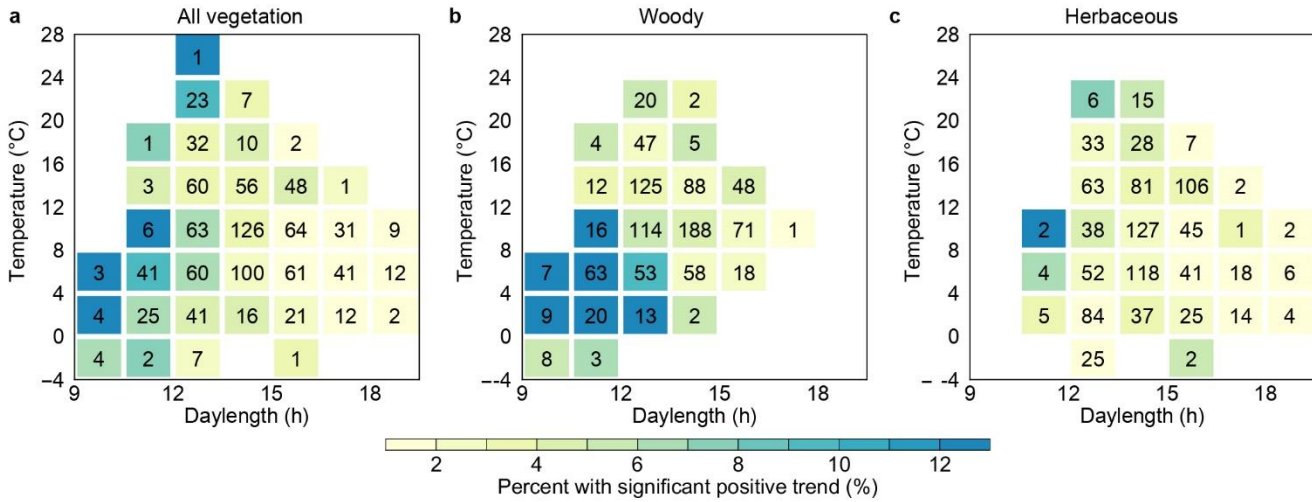


284  
 285 **Figure S21.** Difference in temperature sensitivity between the end and the onset of leaf coloration ( $D_{LCE}$   
 286 and  $D_{LCO}$ ) over the period 2000–2018. The temperature sensitivity of  $D_{LCO}$  was defined as the coefficient  
 287 for pre- $D_{LCO}$  mean daily minimum temperature ( $T_{min}$ ) in the linear regression in which  $D_{LCO}$  was set as  
 288 the dependent variable and pre- $D_{LCO}$   $T_{min}$  and pre- $D_{LCO}$  total precipitation were independent variables.  
 289 The temperature sensitivity of  $D_{LCE}$  was calculated in a similar way.  $D_{LCO}$  and  $D_{LCE}$  were determined as  
 290 the dates when NDVI decreased by 10% and 50%, respectively, of its annual amplitude, on the basis of  
 291 a generalized sigmoid function fitted from the annual NDVI profile. For the pixels identified as  
 292 deciduous broadleaved forests,  $D_{LCO}$  was defined as the date when NDVI decreased by 10% of its  
 293 annual amplitude from 16 August, on the basis of a generalized sigmoid function fitted from the annual  
 294 NDVI profile. The maximum value used to determine the annual amplitude was defined as the mean  
 295 value of the upper quartile of the fitted NDVI values in the second half of August. For the other pixels,  
 296  $D_{LCO}$  was defined as the date when NDVI decreased by 10% of its annual amplitude; the maximum  
 297 value of the fitted curve was used to determine the annual amplitude. The bar chart in the bottom-left  
 298 corner shows the percentage of area for each interval of the temperature sensitivity indicated by the  
 299 color scale at the bottom. Negative values (pink) indicate that  $D_{LCO}$  was more sensitive than  $D_{LCE}$  to  
 300 temperature.

301



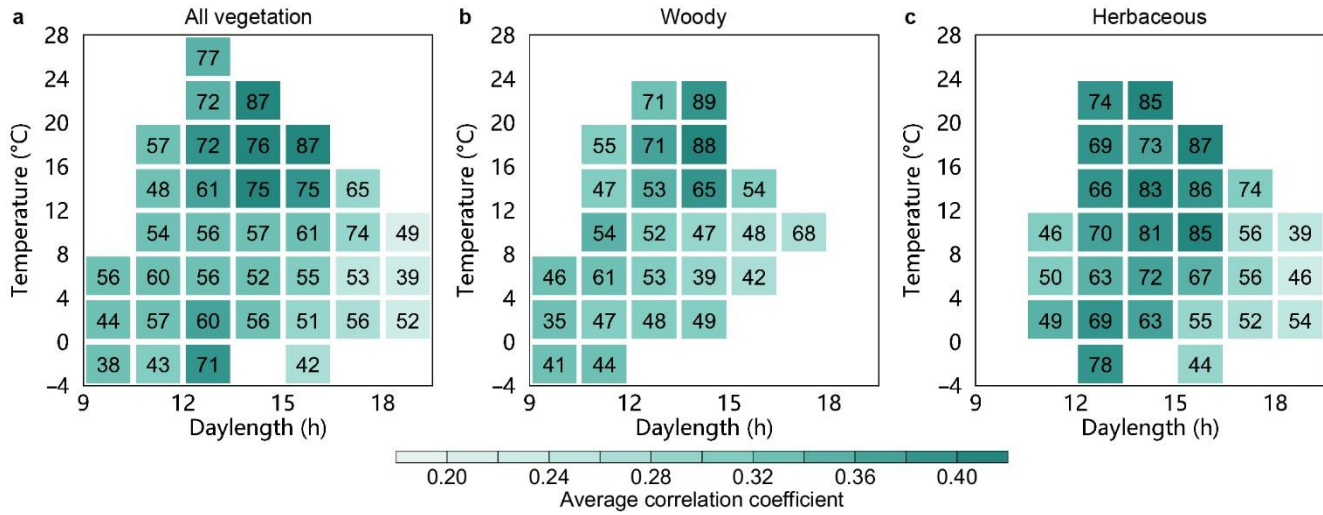
302  
303 **Figure S22.** Temporal trends in the timing of onset of leaf coloration ( $D_{LCO}$ ), as retrieved from satellite  
304 images for 2000–2018. The bar chart in each panel shows the percentage of area within each interval of  
305 the significant ( $P < 0.05$ ) temporal trends and the percentage of area with nonsignificant trends,  
306 indicated by the color scale at the bottom. Positive and negative trend values refer to significantly  
307 delayed and advanced  $D_{LCO}$ , respectively.  $D_{LCO}$  was determined as the date when the rate of change of  
308 the curvature (RCC) of the fitted NDVI curve reached its first local minimum value in the descending  
309 period. For the pixels identified as deciduous broadleaved forests, the fitting function was a modified  
310 double logistic function that considered summer NDVI green-down (Elmore *et al.*, 2012), whereas the  
311 fitting function was a double logistic function for the other pixels (Beck *et al.*, 2006). In (a), significant  
312 temporal trends were determined by using *t*-tests at  $P < 0.05$  and OLSR between  $D_{LCO}$  and the respective  
313 years. In (b), significant temporal trends were determined by using Mann-Kendall tests at  $P < 0.05$  and a  
314 Theil-Sen estimator between  $D_{LCO}$  and the respective years. Pixels dominated by croplands or with low  
315 vegetation coverage, weak seasonality, or peak NDVI in October–April were discarded.



316

**Figure S23.** Dependence of temporal trends in the timing of onset of leaf coloration ( $D_{LCO}$ ) on daylength and temperature at  $D_{LCO}$  over the period 2000–2018 for all (a), woody (b), and herbaceous (c) vegetation. The daylength (indicated by the horizontal axis) was calculated for each pixel (location) at multiyear mean  $D_{LCO}$  over the period 2000–2018 ( $D_{LCO\text{-MEAN}}$ ), and the temperature (indicated by the vertical axis) is the mean daily minimum temperature of the month preceding  $D_{LCO\text{-MEAN}}$ . a, Color indicates the percentage of area with significant ( $P < 0.05$ )  $D_{LCO}$  delays in each cell (i.e., a specific temperature  $\times$  daylength combination), as indicated by the color scale at the bottom. The number in each cell indicates the ratio (unit: %) of the area in each cell to the total area with  $D_{LCO}$  retrieval (i.e., Northern Hemisphere from  $30^{\circ}\text{N}$ – $75^{\circ}\text{N}$ ). Temporal trends and their significances were determined by using the Theil-Sen estimator and Mann-Kendall tests. b and c, The same as (a), but for woody and herbaceous vegetation, respectively. Each cell represents  $4^{\circ}\text{C}$  of temperature and 1.5 h of daylength. Only cells where the ratio of the area of the cell to the total area is  $>1\%$  are represented. Woody and herbaceous vegetation are merged from Classes 1–6 and Class 10, respectively, in the MODIS land-cover product (MCD12C1, Version 6) for 2009.

331



332

**Figure S24.** Dependence of the partial correlation coefficient ( $R_{PRE}$ ) between the timing of onset of leaf coloration ( $D_{LCO}$ ) and pre- $D_{LCO}$  total precipitation on daylength and temperature at  $D_{LCO}$  over the period 2000–2018 for all (a), woody (b), and herbaceous (c) vegetation. Daylength (indicated by the horizontal axis) was calculated for each pixel (location) at multiyear mean  $D_{LCO}$  over the period 2000–2018 ( $D_{LCO-MEAN}$ ), and temperature (indicated by the vertical axis) is the mean daily minimum temperature of the month preceding  $D_{LCO-MEAN}$ . a, Color indicates the average of the positive  $R_{PRE}$ , as indicated by the color scale at the bottom. The number indicates the percentage of area with a positive correlation in each cell (i.e., a specific temperature  $\times$  daylength combination); b and c, The same as (a), but for woody and herbaceous vegetation, respectively. Each cell represents 4 °C of temperature and 1.5 h of daylength. Only cells where the ratio of the area of the cell to the total area is  $>1\%$  are represented. Woody and herbaceous vegetation are merged from Classes 1–6, and Class 10 in the MODIS land-cover product (MCD12C1, Version 6) for 2009.

345

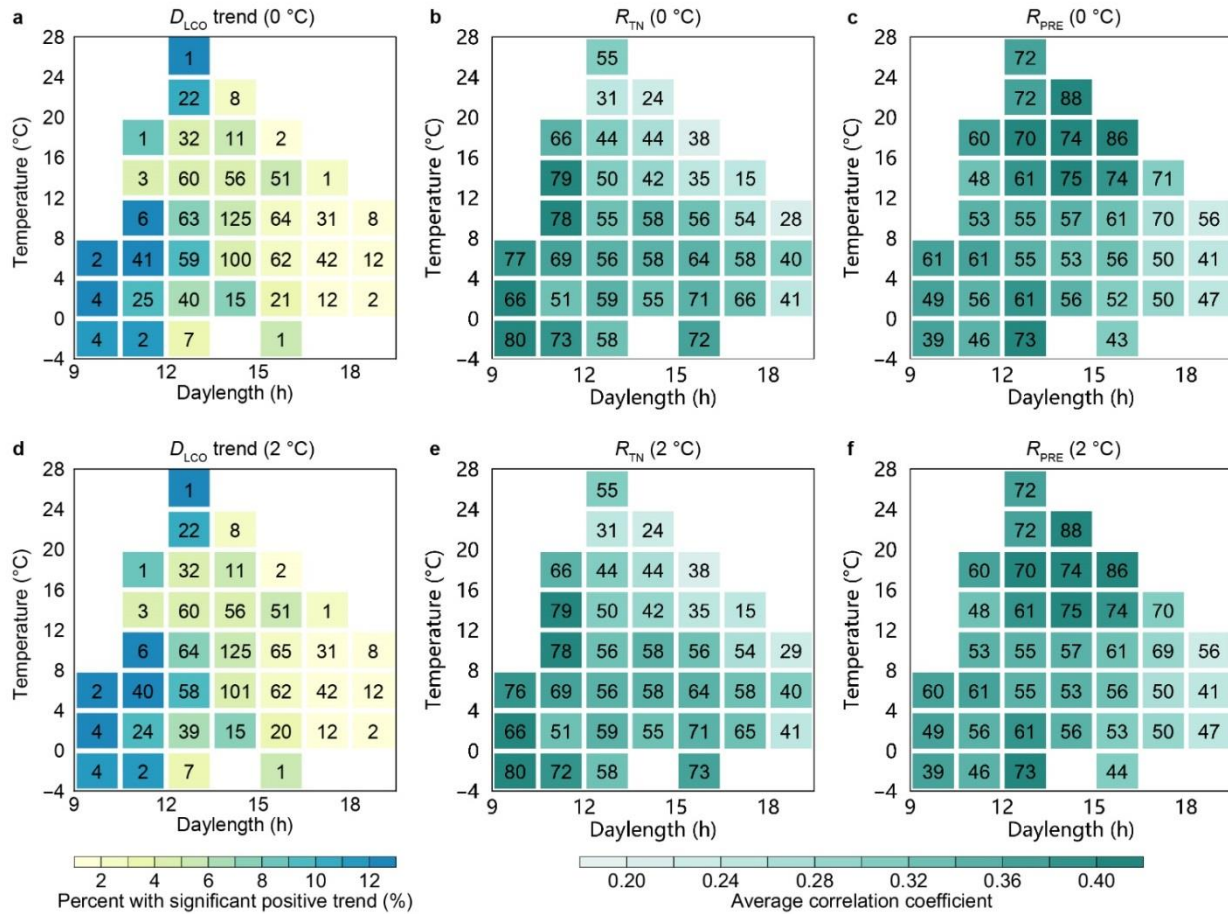


**Figure S25.** Dependence of temporal trends in the timing of onset of leaf coloration ( $D_{LCO}$ , a and d), of the partial correlation coefficient ( $R_{TN}$ , b and e) between  $D_{LCO}$  and pre- $D_{LCO}$  mean daily minimum temperature, and of the partial correlation coefficient ( $R_{PRE}$ , c and f) between  $D_{LCO}$  and pre- $D_{LCO}$  total precipitation on daylength and temperature at  $D_{LCO}$  over the period 2000–2016 after the exclusion of years with cold events before  $D_{LCO}$ . Daylength (indicated by the horizontal axis) was calculated for each pixel (location) at multiyear mean  $D_{LCO}$  over the period 2000–2016 ( $D_{LCO\text{-MEAN}}$ ), and temperature (indicated by the vertical axis) is the mean daily minimum temperature of the month preceding  $D_{LCO\text{-MEAN}}$ . Cold events were determined mainly by using a threshold-based method with a daily minimum temperature of 0 °C (a–c) or 2 °C (d–f). a and d, Color indicates the percentage of area with significant ( $P < 0.05$ )  $D_{LCO}$  delays in each cell (i.e., a specific temperature  $\times$  daylength combination), as indicated by the color scale at the bottom. The number in each cell indicates the ratio (unit: %) of the area in each cell to the total area with  $D_{LCO}$  retrieval (i.e., Northern Hemisphere from 30°N–75°N). b and e, Color indicates the average of the positive  $R_{TN}$ , as indicated by the color scale at the bottom. The number indicates the percentage of area with a positive correlation in each cell. c and f, The same as (b and e), but for the positive  $R_{PRE}$ . Each cell represents 4 °C of temperature and 1.5 h of daylength. Only cells where the ratio of the area of the cell to the total area is  $>1\%$  are represented.

363 **Supplementary Tables**

364

365 **Table S1.** Experiments on photoperiodic control of plant growth.

<b>Species</b>	<b>Life-form</b>	<b>Findings from experiments</b>	<b>Experimental setting</b>	<b>Reference</b>
<i>Acer rubrum</i> L.	Deciduous tree	Growth stopped after about four weeks of short photoperiod treatment (8 hours).	Chamber cultivating +controlled photoperiod	Downs and Borthwick (1956)
<i>Acer saccharum</i> Marsh.	Deciduous tree	Long photoperiod treatment (16 hours) resulted in delayed senescence and abscission for up to five months.	Chamber cultivating +controlled photoperiod	Olmsted (1951)
<i>Aesculus hippocastanum</i> L.	Deciduous tree	Growth stopped after about four weeks of short photoperiod treatment (8 hours).	Chamber cultivating +controlled photoperiod	Downs and Borthwick (1956)
<i>Betula mandshurica</i> [Regel] Nakai.	Deciduous tree	Growth stopped after about four weeks of short photoperiod treatment (8 hours).	Chamber cultivating +controlled photoperiod	Downs and Borthwick (1956)
<i>Betula pubescens</i> Ehrh.	Deciduous tree	Elongation growth ceased after 7–8 days of short photoperiod treatment (12 hours).	Chamber cultivating +controlled photoperiod	Rinne <i>et al.</i> (1994)
<i>Catalpa bignonioides</i> Walt.	Deciduous tree	Growth stopped after about four weeks of short photoperiod treatment (8 hours).	Chamber cultivating +controlled photoperiod	Downs and Borthwick (1956)
<i>Catalpa speciosa</i> Warder	Deciduous tree	Growth stopped after about four weeks of short photoperiod treatment (8 hours).	Chamber cultivating +controlled photoperiod	Downs and Borthwick (1956)
<i>Cornus florida</i> L.	Deciduous tree	Growth stopped after about four weeks of short photoperiod treatment (8 hours).	Chamber cultivating +controlled photoperiod	Downs and Borthwick (1956)
<i>Liquidambar styraciflua</i> L.	Deciduous tree	Growth stopped after about four weeks of short photoperiod treatment (8 hours).	Chamber cultivating +controlled photoperiod	Downs and Borthwick (1956)
<i>Liquidambar styraciflua</i> L.	Deciduous tree	The plant grew nearly all winter under a 16 hours photoperiod.	Chamber cultivating +controlled photoperiod	Kramer (1936)
<i>Liriodendron tulipifera</i> L.	Deciduous tree	Growth stopped after about ten days of short photoperiod treatment (8 hours).	Chamber cultivating +controlled photoperiod	Downs and Borthwick (1956)
<i>Liriodendron tulipifera</i> L.	Deciduous tree	The plant grew all winter under a 16 hours photoperiod.	Chamber cultivating +controlled photoperiod	Kramer (1936)
<i>Paulownia tomentosa</i> [Thunb.] Steud.	Deciduous tree	Growth stopped after about four weeks of short photoperiod treatment (8 hours).	Chamber cultivating +controlled photoperiod	Downs and Borthwick (1956)
<i>Populus trichocarpa</i> Torr, & Gray	Deciduous tree	Plant set bud after 18 days of short photoperiod treatment (13 hours), which is regulated by phytochrome.	Stem cutting + controlled photoperiod	Howe <i>et al.</i> (1996)

Species	Life-form	Findings from experiments	Experimental setting	Reference
<i>Populus tremula</i>	Deciduous tree	Shortening photoperiod was the main trigger for the initiation of autumn senescence.	Chamber cultivating +controlled photoperiod	Fracheboud <i>et al.</i> (2009)
<i>Populus tremula</i>	Deciduous tree	Photoperiod is the sole trigger for the onset of autumn senescence.	Observation under natural conditions	Keskitalo <i>et al.</i> (2005)
<i>Populus tremula x tremuloides</i>	Deciduous tree	When plants are shifted from long days (16 hours) to short days (8 hours), they respond by growth cessation and bud set after 32 days.	Chamber cultivating +controlled photoperiod	Böhlenius <i>et al.</i> (2006)
<i>Ulmus americana</i> L.	Deciduous tree	Growth stopped after about twenty weeks of short photoperiod treatment (8 hours).	Chamber cultivating +controlled photoperiod	Downs and Borthwick (1956)
<i>Picea abies</i> (L.) Karst.	Evergreen tree	Growth cessation occurred within two weeks after exposure to short photoperiods ( $\leq 15$ hours).	Chamber cultivating +controlled photoperiod	Heide (1974)
<i>Picea glauca</i> (Moench) Voss	Evergreen tree	Growth cessation occurred after five weeks of short photoperiod treatment (8 hours) under warm temperature conditions.	Chamber cultivating +controlled photoperiod	Hamilton <i>et al.</i> (2016)
<i>Pinus sylvestris</i> L.	Evergreen tree	Northern populations grown under 50°N photoperiod (shorter) stopped growth earlier than that under 60°N photoperiod (longer).	Chamber cultivating +controlled photoperiod	Oleksyn <i>et al.</i> (1992)
<i>Pinus sylvestris</i> L.	Evergreen tree	Growth stopped after about four weeks of short photoperiod treatment (8 hours).	Chamber cultivating +controlled photoperiod	Downs and Borthwick (1956)
<i>Pinus taeda</i> L.	Evergreen tree	Growth stopped after about four weeks of short photoperiod treatment (8 hours).	Chamber cultivating +controlled photoperiod	Downs and Borthwick (1956)
<i>Pinus taeda</i> L.	Evergreen tree	The plant grew all winter with a 14.5 hours photoperiod.	Chamber cultivating +controlled photoperiod	Kramer (1936)
<i>Pinus virginiana</i> Mill.	Evergreen tree	Growth stopped after about four weeks of short photoperiod treatment (8 hours).	Chamber cultivating +controlled photoperiod	Downs and Borthwick (1956)
<i>Salix pentandra</i> L.	Deciduous small tree or shrub	Short photoperiod ( $\leq 22$ hours for a northern ecotype and $\leq 15$ hours for a southern ecotype) induced apical growth cessation.	Chamber cultivating +controlled photoperiod	Junntila (1980)
<i>Salix polaris</i> L.	Deciduous small tree or shrub	Leaf abscission in the arctic ecotype was stimulated by short photoperiod when grown at 15°C.	Collected with roots + controlled photoperiod	Paus <i>et al.</i> (1986)
<i>Syringa vulgaris</i> L.	Deciduous small tree or shrub	Photosynthetic efficiency has a more consistent relationship with photoperiod than with temperature.	Observation under natural conditions	Aikio <i>et al.</i> (2019)

Species	Life-form	Findings from experiments	Experimental setting	Reference
<i>Hibiscus rosa-sinensis</i> L.	Evergreen small tree or shrub	Leaves under long photoperiod treatment (16 hours) spend ten more days to complete senescence than that under short photoperiod treatment (8 hours).	Leaves cutting + controlled photoperiod	Misra and Biswal (1973)
<i>Hibiscus syriacus</i> L.	Deciduous shrub	Short photoperiod (8 hours) induced dormancy while long photoperiod (16 hours) delayed dormancy and resulted in considerable winter injury	Chamber cultivating +controlled photoperiod	Davidson (1957)
<i>Weigela florida</i> A. DC.	Deciduous shrub	Short photoperiod (8 hours) induced dormancy while long photoperiod (16 hours) delayed dormancy and resulted in considerable winter injury.	Chamber cultivating +controlled photoperiod	Davidson (1957)
<i>Rhododendron catawbiense</i> Michx.	Evergreen shrub	Short photoperiod (8 hours) induced dormancy while long photoperiod (16 hours) delayed dormancy and resulted in considerable winter injury.	Chamber cultivating +controlled photoperiod	Davidson (1957)
<i>Cucurbita pepo</i> Linn.	Herbaceous	After three months of growth, much larger percentage of mesophyll cell death was detected in short photoperiod (9 hours) than that in long photoperiod (18 hours).	Chamber cultivating +controlled photoperiod	Wang <i>et al.</i> (2002)
<i>Sedum telephium</i> L. subsp. <i>maximum</i> (L.) Krocke	Herbaceous	After eight weeks of growth, plants in long photoperiod (24 hours) elongated rapidly while those in short photoperiod (10 hours) became dormant.	Chamber cultivating +controlled photoperiod	Heide (2001)
<i>Vitis labruscana</i> Bailey	Herbaceous	Cane elongation was less in response to short photoperiod treatments (12 or 13 hours), as compared to natural photoperiod (13.7 or 14.3 hours).	Stem cutting + controlled photoperiod	Fennell and Hoover (1991)
<i>Vitis riparia</i> Michx.	Herbaceous	Cane elongation was less in response to short photoperiod treatments (12 or 13 hours), as compared to natural photoperiod (13.7 or 14.3 hours).	Stem cutting + controlled photoperiod	Fennell and Hoover (1991)

**Table S2.** *In situ* observations in China used in this study.

Site Name	Latitude	Longitude	Species number	Start year	End year	Year length
Nunkiang	49	125	5	1975±0	1993±4	17±4
Wudalianchi	48	126	11	1976±3	1995±3	18±3
Kiamusze	47	130	6	1981±1	1996±0	16±1
Minqin	38	103	29	1981±1	1996±1	12±1
Hohhot	41	112	10	1981±2	1996±1	13±2
Mutankiang	44	130	41	1980±2	1996±2	13±2
Beijing	40	116	42	1972±1	1994±3	20±4
Chengteh	41	118	5	1983±2	1996±0	12±1
Qinhuangdao	39	119	15	1980±0	1993±0	13±1
Gaizhou	40	122	12	1979±1	1996±0	17±1
Yixian	39	115	17	1980±0	1993±0	12±1
Liaocheng	36	115	5	1974±4	1993±2	15±3
Tyan	36	117	5	1974±0	1986±0	11±0
Sian	34	109	33	1977±3	1994±3	15±3
Luoyang	35	113	27	1977±4	1996±1	18±4
Yancheng	33	120	19	1981±4	1996±0	15±3
Zhengjiang	32	119	15	1976±3	1993±2	17±3
Hefei	32	117	19	1979±1	1995±1	17±2
Wuhu	31	118	16	1982±1	1996±0	13±1

The mean  $\pm$  standard deviation of start year, end year and length of time series are provided for each site.

**Table S3.** FLUXNET2015 flux tower sites used in this study.

<b>Fluxnet ID</b>	<b>Vegetation type</b>	<b>Latitude</b>	<b>Longitude</b>	<b>Year range</b>	<b>Reference</b>
BE-Bra	Mixed Forests	51.31	4.52	1999-2002,2004-2014	Janssens (2016)
BE-Vie	Mixed Forests	50.31	6.00	1996-2014	De Ligne <i>et al.</i> (2016)
CA-Gro	Mixed Forests	48.22	-82.16	2003-2013	McCaughey (2016)
CA-Man	Evergreen Needleleaf Forest	55.88	-98.48	1994-2004,2006-2008	Amiro (2016)
CA-Oas	Mixed Forests	53.63	-106.20	1996-2010	Black (2016b)
CA-Obs	Evergreen Needleleaf Forest	53.99	-105.12	1999-2010	Black (2016a)
CA-TP3	Mixed Forests	42.71	-80.35	2003-2014	Arain (2016b)
CA-TP4	Mixed Forests	42.71	-80.36	2002-2014	Arain (2016a)
CH-Dav	Evergreen Needleleaf Forest	46.82	9.86	1997-2014	Hörtnagl <i>et al.</i> (2016b)
CH-Lae	Mixed Forests	47.48	8.37	2004-2014	Hörtnagl <i>et al.</i> (2016a)
CZ-BK1	Evergreen Needleleaf Forest	49.50	18.54	2004-2014	Šigut <i>et al.</i> (2016)
DE-Gri	Mixed Forests	50.95	13.51	2004-2014	Bernhofer <i>et al.</i> (2016b)
DE-Hai	Mixed Forests	51.08	10.45	2000-2012	Knohl <i>et al.</i> (2016)
DE-Tha	Evergreen Needleleaf Forest	50.96	13.57	1996-2014	Bernhofer <i>et al.</i> (2016a)
DK-Sor	Deciduous Broadleaf Forest	55.49	11.64	1996-2014	Ibrom and Pilegaard (2016)
DK-ZaH	Open Shrublands	74.47	-20.55	2000-2010,2012-2014	Lund <i>et al.</i> (2016)
FI-Hyy	Evergreen Needleleaf Forest	61.85	24.30	1996-2014	Mammarella <i>et al.</i> (2016)
FI-Sod	Evergreen Needleleaf Forest	67.36	26.64	2001-2014	Aurela <i>et al.</i> (2016)
FR-Fon	Deciduous Broadleaf Forest	48.48	2.78	2005-2014	Berveiller <i>et al.</i> (2016)
IT-Col	Deciduous Broadleaf Forest	41.85	13.59	1997-2002,2004-2014	Matteucci (2016)
IT-Lav	Evergreen Needleleaf Forest	45.96	11.28	2003-2014	Gianelle <i>et al.</i> (2016b)
IT-MBo	Grasslands	46.01	11.05	2003-2013	Gianelle <i>et al.</i> (2016a)
IT-Ren	Evergreen Needleleaf Forest	46.59	11.43	1999,2002-2003,2005-2013	Minerbi and Montagnani (2016)
NL-Loo	Evergreen Needleleaf Forest	52.17	5.74	1996-2014	Moors and Elbers (2016)
RU-Cok	Open Shrublands	70.83	147.49	2003-2013	Dolman <i>et al.</i> (2016)
RU-Fyo	Mixed Forests	56.46	32.92	1998-2014	Varlagin <i>et al.</i> (2016)
US-GLE	Evergreen Needleleaf Forest	41.36	-106.24	2005-2014	Massman (2016)
US-Ha1	Mixed Forests	42.54	-72.17	1992-2012	Munger (2016)
US-MMS	Deciduous Broadleaf Forest	39.32	-86.41	1999-2014	Novick and Phillips (2016)
US-Me2	Evergreen Needleleaf Forest	44.45	-121.56	2002-2014	Law (2016)
US-NR1	Evergreen Needleleaf Forest	40.03	-105.55	1999-2014	Blanken (2016)
US-Oho	Deciduous Broadleaf Forest	41.55	-83.84	2004-2013	Chen (2016)
US-PFa	Mixed Forests	45.95	-90.27	1996-2014	Desai (2016)
US-SRM	Open Shrublands	31.82	-110.87	2004-2014	Scott (2016a)
US-UMB	Deciduous Broadleaf Forest	45.56	-84.71	2000-2014	Gough <i>et al.</i> (2016)
US-Wkg	Grasslands	31.74	-109.94	2004-2014	Scott (2016b)

373 **Table S4.** Proportions of years with cold events before  $D_{LCO}$  (for satellite and *in situ* observations) and  
 374 before  $D_{PDO}$  (for FLUXNET2015).

Metrics	Satellite $D_{LCO}$ (2000–2016)	<i>in situ</i> $D_{LCO}$ China	FLUXNET2015 $D_{PDO}$
Proportion (%) of years with cold events (0 °C)	1	2	1
Proportion (%) of years with cold events (2 °C)	2	3	1

375  $D_{PDO}$ , timing of onset of the decrease in maximum canopy photosynthetic capacity in autumn;  $D_{LCO}$ , timing of onset of leaf  
 376 coloration in autumn. Cold events were determined mainly by using a threshold-based method with a daily minimum  
 377 temperature of 0 °C or 2 °C.

378

379 **Table S5.** Percentage of time series for each interval of the temporal trend in  $D_{LCO}$  before and after the  
 380 exclusion of years with cold events.

Metrics	Number of time-series	Cold events	Interval of significant temporal trend ( $\text{d y}^{-1}$ ) ( $P < 0.05$ )				$P > 0.05$
			<-1	[-1, 0)	(0, 1]	>1	
Satellite $D_{LCO}$ (2000–2016)	$2.01 \times 10^6$	Not excluded	2	2	2	4	90
		Excluded (0 °C)	2	2	2	4	90
		Excluded (2 °C)	2	2	1	5	90
<i>in situ</i> $D_{LCO}$ China	326	Not excluded	12	4	4	6	74
		Excluded (0 °C)	12	4	5	6	73
		Excluded (2 °C)	12	3	5	7	73

381  $D_{LCO}$ , timing of onset of leaf coloration in autumn. Temporal trends were determined by using the ordinary least squares  
 382 regression between  $D_{LCO}$  and the respective years, with *t*-tests. Only time series with at least 10 continuous years of data after  
 383 exclusion of years with cold events were included. Cold events were determined mainly by using a threshold-based method  
 384 with a daily minimum temperature of 0 °C or 2 °C. Data in the farthest right column indicate the percentage of area or time-  
 385 series with a non-significant trend.

386

387 **Table S6.** Percentage of time series for each interval of the temporal trend in  $D_{LCO}$ .

Metrics	Number of time-series	Interval of significant temporal trend ( $\text{d y}^{-1}$ ) ( $P < 0.05$ )				$P > 0.05$
		<-1	[-1, 0)	(0, 1]	>1	
Satellite $D_{LCO}$ (2000–2018)	$2.07 \times 10^6$	1	2	1	3	93
<i>in situ</i> $D_{LCO}$ China	332	8	2	3	3	84

388  $D_{LCO}$ , timing of the onset of leaf coloration in autumn. Temporal trends were determined by using the Theil-Sen estimator  
 389 between  $D_{LCO}$  and the respective years, with Mann-Kendall tests. Data in the farthest right column indicate the percentage of  
 390 area or time-series with a non-significant trend.

391

392 **Table S7.** Percentage of correlations between  $D_{LCO}$  or  $D_{PDO}$  and each climate factor for each interval of  
 393 the partial correlation coefficient before and after the exclusion of years with cold events.

Metrics	Climatic Factor	Cold Events	Interval of the partial correlation coefficient ( $P < 0.05$ )						$P > 0.05$
			[-1.0, -0.8]	[-0.8, -0.6]	[-0.6, 0]	(0, 0.6]	(0.6, 0.8]	(0.8, 1.0]	
Satellite $D_{LCO}$ (2000–2016)	Temperature	Not excluded	0	2	4	5	3	0	86
		Excluded (0 °C)	0	2	4	5	3	0	86
		Excluded (2 °C)	0	2	4	5	3	0	86
	Precipitation	Not excluded	0	2	3	7	5	0	83
		Excluded (0 °C)	0	2	3	7	5	0	83
		Excluded (2 °C)	0	2	3	7	5	0	83
<i>in situ</i> $D_{LCO}$ China	Temperature	Not excluded	0	2	3	4	8	1	82
		Excluded (0 °C)	0	2	2	4	9	1	82
		Excluded (2 °C)	0	2	2	4	9	1	82
	Precipitation	Not excluded	0	3	3	4	5	0	85
		Excluded (0 °C)	0	4	3	3	6	0	84
		Excluded (2 °C)	0	4	3	3	6	0	84
FLUXNET2015 $D_{PDO}$	Temperature	Not excluded	0	5	3	0	0	0	89
		Excluded (0 °C)	0	5	3	0	0	0	92
		Excluded (2 °C)	0	5	3	0	0	0	92
	Precipitation	Not excluded	0	6	0	8	3	5	78
		Excluded (0 °C)	0	6	0	8	3	5	78
		Excluded (2 °C)	0	6	0	8	3	5	78

394  $D_{PDO}$ , timing of onset of decrease in maximum canopy photosynthetic capacity in autumn;  $D_{LCO}$ , timing of onset of leaf  
 395 coloration in autumn. The relationships between  $D_{LCO}$  (or  $D_{PDO}$ ) and temperature were determined by using a partial  
 396 correlation analysis between  $D_{LCO}$  (or  $D_{PDO}$ ) and pre- $D_{LCO}$  (or pre- $D_{PDO}$ ) mean daily minimum temperature, with concurrent  
 397 total precipitation as the control variable. The relationships between  $D_{LCO}$  (or  $D_{PDO}$ ) and pre- $D_{LCO}$  (or pre- $D_{PDO}$ ) precipitation  
 398 were determined similarly. Cold events were determined mainly by using a threshold-based method with a daily minimum  
 399 temperature of 0 °C or 2 °C. Data in the farthest right column indicate the percentage of area or time-series with a non-  
 400 significant correlation.  
 401

402   **Table S8.** Percentage of correlations between  $D_{LCO}$  or  $D_{PDO}$  and each climate factor for each interval of  
 403   the partial correlation coefficient.

Climatic factor	Metrics	Interval of the partial correlation coefficient ( $P < 0.05$ )						$P > 0.05$
		[-1.0, -0.8)	[-0.8, -0.6)	[-0.6, 0)	(0, 0.6]	(0.6, 0.8]	(0.8, 1.0]	
Temperature	FLUXNET2015 $D_{PDO}$	0	7	0	0	3	0	90
	Satellite $D_{LCO}$	0	4	3	3	3	0	87
Precipitation	FLUXNET2015 $D_{PDO}$	0	7	0	0	3	7	83
	Satellite $D_{LCO}$	0	0	0	0	7	0	93

404    $D_{PDO}$ , timing of onset of decrease in maximum canopy photosynthetic capacity in autumn;  $D_{LCO}$ , timing of onset of leaf  
 405   coloration in autumn. The relationships between  $D_{LCO}$  (or  $D_{PDO}$ ) and temperature were determined by using a partial  
 406   correlation analysis between  $D_{LCO}$  (or  $D_{PDO}$ ) and pre- $D_{LCO}$  (or pre- $D_{PDO}$ ) mean daily minimum temperature, with concurrent  
 407   total precipitation as the control variable. The relationships between  $D_{LCO}$  (or  $D_{PDO}$ ) and pre- $D_{LCO}$  (or pre- $D_{PDO}$ ) precipitation  
 408   were determined similarly. Only sites with at least 10 continuous years of valid data for both  $D_{LCO}$  and  $D_{PDO}$  were included.  
 409   Data in the farthest right column indicate the percentage of area or time-series with a non-significant correlation. To make the  
 410   satellite  $D_{LCO}$  and FLUXNET2015  $D_{PDO}$  more comparable, MOD09A1 with a spatial resolution of 500 m was used for  
 411   extracting satellite  $D_{LCO}$ .

412

413 **Supplementary Methods**414 **1 Preparation of high quality 5-day NDVI time series**

415 The quality of the daily surface reflectance data from MOD09CMG was unsatisfactory owing to  
 416 cloud contamination (Vermote, 2015), so we used the 5-day maximum value composite approach  
 417 (Zhang, 2015), combined with a Savitzky-Golay filter (Cao *et al.*, 2018), to produce a high-quality  
 418 NDVI time series before determining  $D_{LCO}$ . Details of the data preprocessing are given in the following  
 419 text.

420 1) Calculating daily NDVI. We calculated the daily NDVI time series with the quality flag from  
 421 surface reflectance in the red and near-infrared bands as  $NDVI = (NIR - RED)/(NIR + RED)$ . The  
 422 quality flags for daily NDVI were derived from the two quality bands (i.e., Internal CM and State QA)  
 423 of the reflectance product MOD09CMG (Vermote *et al.*, 2015). We determined four types of conditions  
 424 that corresponded to the assigned quality flags: 1) clear, 2) uncertain, 3) snowy, and 4) cloudy (with  
 425 deteriorating data quality), according to Cao *et al.* (2018). These were subsequently used in the Savitzky-  
 426 Golay filtering (Cao *et al.*, 2018). To be precise, the quality flag was set to “cloudy” if the cloud state in  
 427 either Internal CM or State QA was labeled as “yes” or “cloudy or mixed”; the quality flag was set to  
 428 “snowy” if the snow/ice flag in State QA was labeled as “yes”; and the quality flag was set to “uncertain”  
 429 if the cloud state in State QA was not set (assumed clear). All the other data flags were set to “clear”  
 430 (see the index table below). In addition, considering that the NDVI value of a vegetation pixel ranged  
 431 from −0.2 to 1.0, NDVI data outside this range were treated as gaps in the NDVI time series.

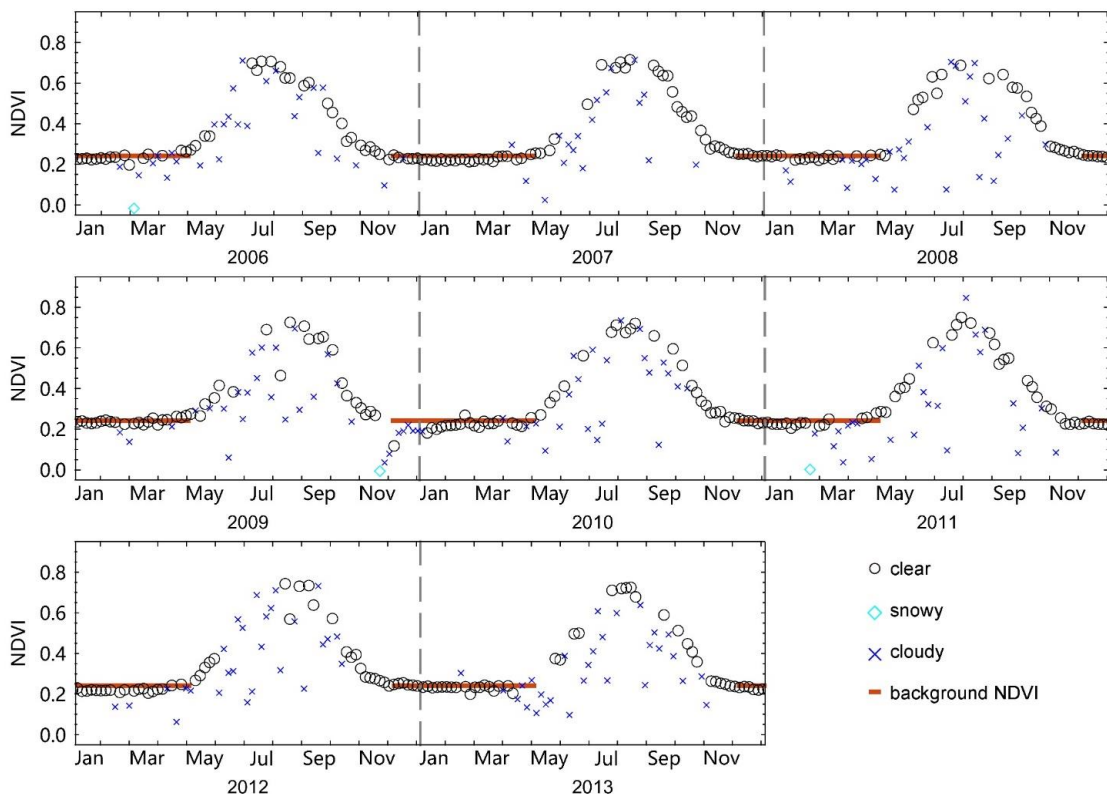
Quality flag of daily NDVI	MOD35 snow/ice flag in State QA	Cloud state in State QA	Cloud state in Internal CM
clear	no	clear	no
uncertain	no	not set (assumed clear)	no
snowy	yes	clear or not set (assumed clear)	no
cloudy	-	cloudy or mixed	-
	-	-	yes

432 “No” and “yes” in the snow/ice flag indicate absence and presence of snow or ice, respectively; “no” and “yes” in the internal  
 433 CM indicate absence and presence of cloud, respectively; “-” means no specific snow/ice or cloud state was required.

434 2) Determining the background NDVI value for each pixel. The background value represents the  
 435 annual minimum NDVI during winter (December–February), in which NDVI was expected to be stable  
 436 for winter deciduous vegetation if there was no snow/ice or cloud contamination. The background NDVI  
 437 value was calculated as the mean of high winter NDVI values, because snow/ice or cloud contamination

438 decreases NDVI owing to the uncertainties in the snow/ice and cloud flags (Beck *et al.*, 2006). To obtain  
 439 high winter NDVI values for a given pixel, we first calculated a time series of winter NDVI higher than  
 440 0.10 (snow-contaminated NDVI is usually lower than 0.10). The high winter NDVI values were  
 441 expected to be higher than the 50th percentile of this time series of winter NDVI and lower than the  
 442 mean + 2SD of this time series of winter NDVI. In some cases, there would be no winter NDVI values  
 443 higher than 0.10; for these cases the background NDVI value was set at 0.10.

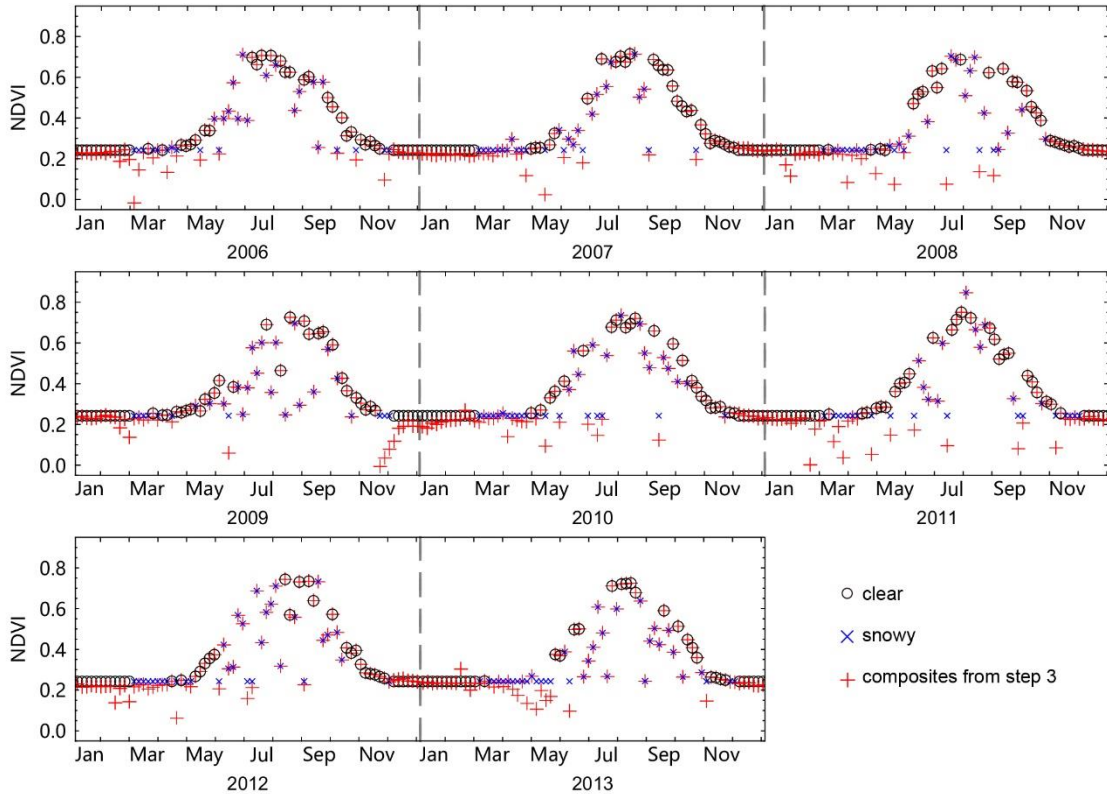
444 3) Compositing the 5-day NDVI time series from daily NDVI time series. The daily NDVI time-  
 445 series were aggregated to a 5-day composite as follows: if there were one or more NDVI values meeting  
 446 the quality level (i.e., the quality flag is “clear” in step 1) within the 5-day period, the median value was  
 447 used as the composite value to reduce noise, and the composite value was flagged as “clear”. If no  
 448 acceptable NDVI data were found in the 5-day period, the maximum value was used as the composite  
 449 value (see Figure SM1), and the composite value was flagged as the corresponding daily quality flag of  
 450 the maximum value.



451

452 **Figure SM1.** An example (31.325°N, 98.125°E) showing composite 5-day NDVI time series from  
 453 daily NDVI time series.

454        4) Eliminating snow cover contamination in NDVI data. NDVI values in winter (December–  
 455 February) were all replaced by the background NDVI value, and their flag was set to “clear”, meaning  
 456 that those NDVI values were not changed in the Savitzky-Golay filtering. In the other three seasons  
 457 (March–November), the NDVI values lower than this background NDVI value were then substituted for  
 458 the latter one (see Figure SM2) and their flag values were set to “cloudy”.



459        460 **Figure SM2.** An example showing the elimination of snow cover contamination in NDVI data.  
 461

462        5) Identifying irregularly high and low NDVI values. Disturbances in surface reflectance data,  
 463 which are caused by cloud contamination, bidirectional effects, and data transmission errors, result in  
 464 irregularly high and low NDVI values. Most of these irregular NDVI values could be marked by using  
 465 the quality flag in step 1. However, because of the uncertainty of the quality flag, there was still a sharp  
 466 increase or sudden large decrease of NDVI values flagged as “clear” in the 5-day NDVI profile from  
 467 March to November. Because vegetation growth is a continuous process without large increases or  
 468 decreases in greenness over a few days, NDVI values that showed sharp decreases or increases were  
 469 defined as irregularly low or high NDVI values, respectively, and they were identified by using the

470 shape of the NDVI curve and an outlier detection method.

471 The irregularly low NDVI values were identified by using the shape of the NDVI curve.  
472 Assuming that the 5-day NDVI increased or decreased gradually in a seasonal course, for any 5-day  
473 NDVI at time  $t$ , denoted as  $NDVI(t)$ , an  $NDVI(t)$  was identified as an irregularly low value, if there  
474 existed two positive integers  $k$  and  $m$  satisfying

$$475 \quad NDVI(t) - NDVI(t - k) \leq -k \times (0.15 \times \text{maxNDVI})$$

$$476 \quad NDVI(t) - NDVI(t + m) \leq -m \times (0.15 \times \text{maxNDVI})$$

477 where  $1 \leq k \leq 6$ ,  $1 \leq m \leq 6$ , and maxNDVI was the 75th percentile of the time series of annual maximum  
478 NDVI from 2000 to 2018. In a few cases, there may have been two consecutive irregularly low values,  
479 which were identified as follows. Two consecutive NDVI values,  $NDVI(t)$  and  $NDVI(t + 1)$ , were  
480 identified as consecutive irregularly low values if they satisfied the following inequalities:

$$481 \quad NDVI(t) - NDVI(t - 1) \leq -1 \times (0.15 \times \text{maxNDVI})$$

$$482 \quad NDVI(t + 1) - NDVI(t - 1) \leq -0.9 \times (0.15 \times \text{maxNDVI})$$

$$483 \quad NDVI(t + 1) - NDVI(t + 2) \leq -2 \times (0.15 \times \text{maxNDVI}).$$

484 The irregularly high NDVI values were identified by using the shape of the NDVI curve and an  
485 outlier detection method. The NDVI curve shape-based method included two procedures. Procedure 1  
486 was to detect non-consecutive irregularly high NDVI values. Assuming that the 5-day NDVI increased  
487 or decreased gradually in a seasonal course, an NDVI value at time  $t$ ,  $NDVI(t)$ , was identified as an  
488 irregularly high value if it satisfied

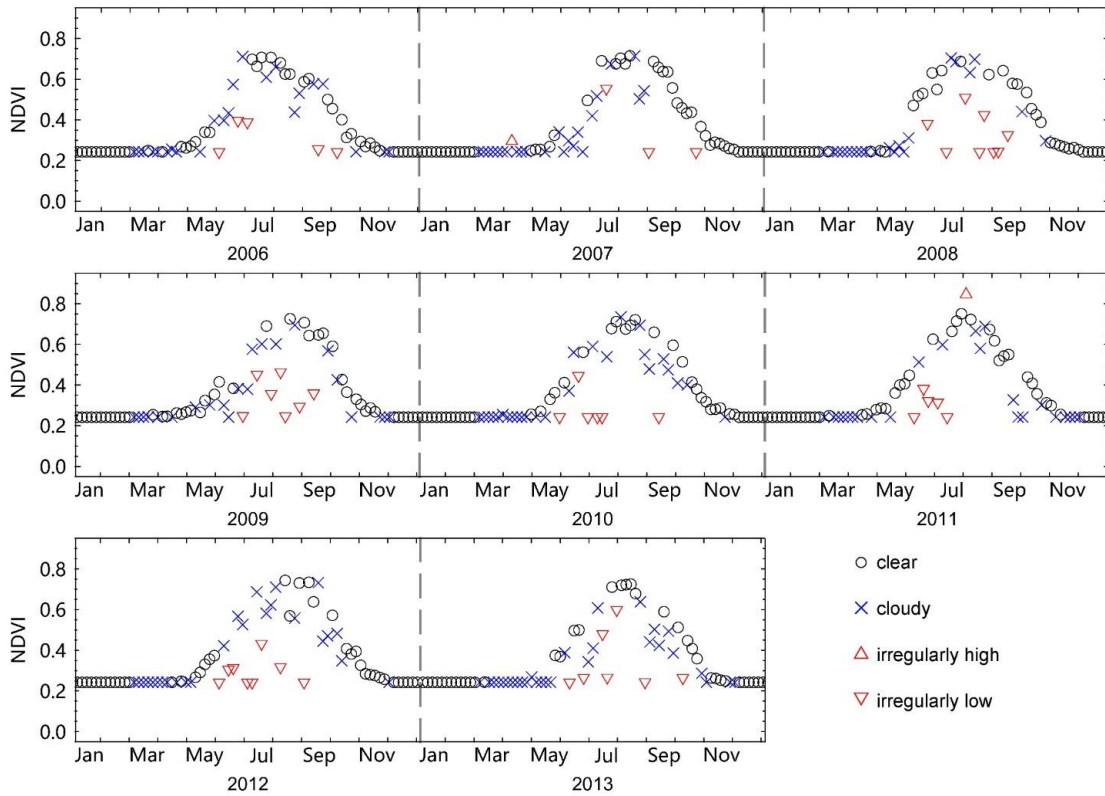
$$489 \quad NDVI(t) \geq 1.15 \times \max\{NDVI(t - 6), NDVI(t - 5), \dots, NDVI(k), \dots, NDVI(t + 6)\}$$

490 where  $t - 6 \leq k \leq t + 6$  and  $k \neq t$ .

491 In some cases, there could be two or more irregularly high NDVI values within 1 month around  
492 peak season that could not be detected by using the above algorithm. Such irregularly high NDVI values  
493 were identified in Procedure 2, which used the information of a non-consecutive irregularly high NDVI  
494 value identified in Procedure 1. We first constructed an array by selecting non-consecutive irregularly  
495 high NDVI values in Procedure 1, which were the annual maximum values (denoted as  $NDVI_{IHM}$ ). Then,  
496 the NDVI values were identified as irregularly high NDVI values if they were 15% higher than the  
497 median value of the array of  $NDVI_{IHM}$ .

498        Because the NDVI values around the peak season were essential for retrieving  $D_{LCO}$ , to be more  
 499 robust, the irregularly high NDVI values were also identified by using Grubbs's test (Grubbs, 1950). We  
 500 first composed an array by using the three highest NDVI values of each year. The outliers in this array  
 501 were then detected by using Grubbs's test at a significance level of  $\alpha = 0.05$ . Owing to inter-annual  
 502 variations in the annual maximum greenness, the outliers detected by Grubbs's test may not necessarily  
 503 have been the irregularly high NDVI values. Therefore, in a given year, only outliers that were 15%  
 504 higher than the mean of the three highest non-outlier NDVI values for that year were identified as  
 505 irregularly high NDVI values. Finally, all the irregularly high NDVI values identified above were used  
 506 as irregularly high NDVI values.

507        The figure SM3 gives examples of irregularly low and high NDVI values.



508        509 **Figure SM3.** An example showing irregularly high and low NDVI values identified in the 5-day  
 510 composed NDVI time series.

511        512 6) Processing the NDVI values flagged as “cloudy”. Because clouds are overestimated by the  
 513 cloud flag (Wilson *et al.*, 2014), there were a considerable number of high NDVI values during March–

514 November that were flagged as “cloudy” but that appeared to be reasonable in the seasonal NDVI  
515 profile. We detected these NDVI values and promoted their flags to be “uncertain” (“uncertain”  
516 indicates a quality higher than “cloudy” but lower than “clear”, see Cao *et al.* (2018) for details). First, a  
517 pixel-year was excluded from our study if each of the NDVI values from May to September was either  
518 “cloudy” or “irregular”. Second, for NDVI values lower than 90% of their annual range plus the  
519 background NDVI value, the NDVI at time  $t$ ,  $NDVI(t)$ , was flagged as “uncertain” if it satisfied the  
520 following,

$$521 \quad NDVI(t) \geq \max\{NDVI(t-2), NDVI(t-1), NDVI(t), NDVI(t+1), NDVI(t+2)\},$$

522 where  $NDVI(t)$  had been flagged as “cloudy”, and  $NDVI(t-2)$ ,  $NDVI(t-1)$ ,  $NDVI(t+1)$ , and  $NDVI(t+2)$   
523 had all been flagged as “cloudy” or “irregular”.

524 Moreover,

$$525 \quad NDVI(t) \geq 0.85 \times \max\{NDVI(t-12), NDVI(t-11), \dots, NDVI(t-1)\}$$

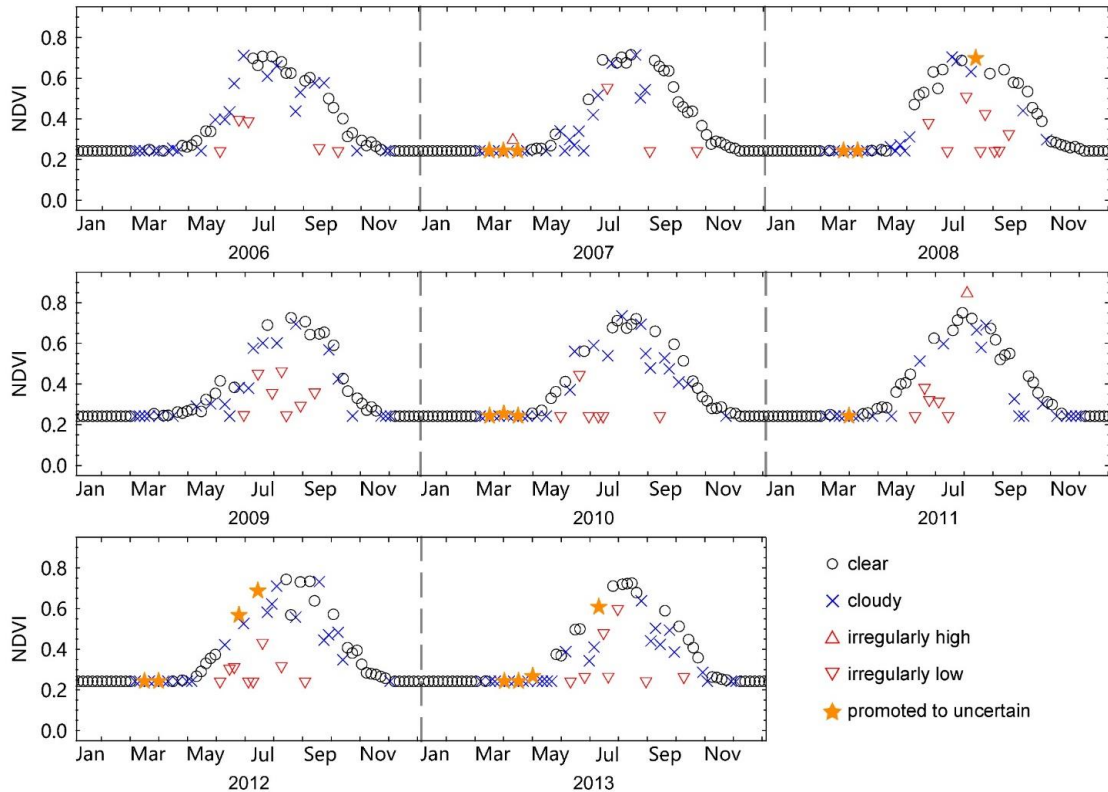
526 for  $NDVI(t)$  in an ascending period (i.e., from early March to the time of annual maximum NDVI), and

$$527 \quad NDVI(t) \geq 0.85 \times \max\{NDVI(t+1), NDVI(t+2), \dots, NDVI(t+12)\}$$

528 for  $NDVI(t)$  in a descending period (i.e., from the time of annual maximum NDVI to late November).

529 The figure SM4 gives an example of NDVI values that were promoted from “cloudy” to “uncertain”.

530

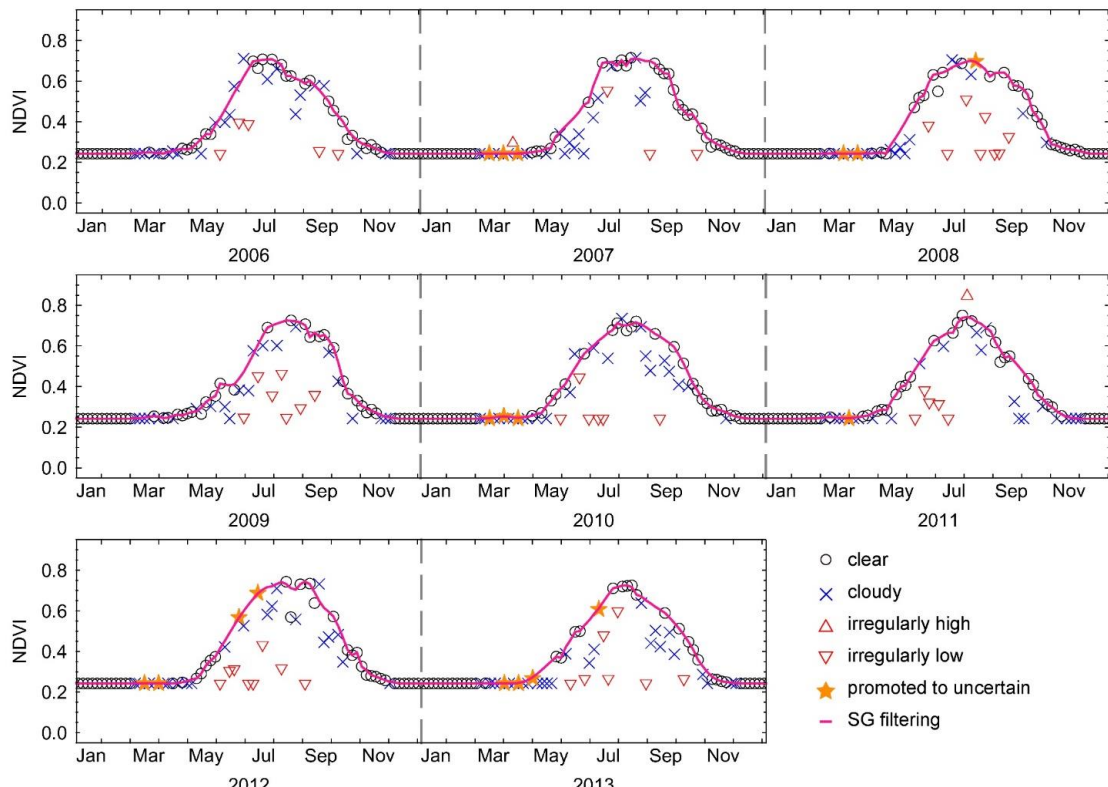


531

532 **Figure SM4.** An example showing NDVI values with flags promoted from “cloudy” to “uncertain”.

533

534 7) Reconstructing 5-day continuous high-quality NDVI time series. Because clouds and poor  
 535 atmospheric conditions contaminate NDVI values, we applied a Savitzky-Golay filter to reconstruct a  
 536 high-quality NDVI time-series as described by Cao *et al.* (2018) and Shen *et al.* (2014). The source code  
 537 of Spatial-Temporal Savitzky-Golay (STSG) is available at [https://github.com/cao-](https://github.com/cao-sre/STSG_IDL_program)  
 538 [sre/STSG\\_IDL\\_program](https://github.com/cao-sre/STSG_IDL_program) (assessed on 19 December 2018). Before we applied the filter, the “irregular”  
 539 quality flags were merged to “cloudy”. In our study, we used the same parameter setting as Cao *et al.*  
 540 (2018), except that the half width of the search window and the half width of the smoothing window  
 541 were both set to 5. The figure SM5 gives an example of the filtering.



542

543 **Figure SM5.** An example showing the output of SG filtering.

544

545

546

547 **2 Comparison between satellite  $D_{LCO}$  and  $D_{LCO}$  from PhenoCam dataset**

548 To better match the PhenoCam images, we used the satellite MOD09A1 dataset (collection 6)  
549 which has a spatial resolution of 500 m and temporal resolution of 8 days. The dataset was downloaded  
550 from <https://modis.ornl.gov/globalsubset/> on March 10, 2021. The PhenoCam dataset V2.0 was  
551 downloaded from [https://daac.ornl.gov/cgi-bin/dsviewer.pl?ds\\_id=1674](https://daac.ornl.gov/cgi-bin/dsviewer.pl?ds_id=1674) on August 29, 2020. From the  
552 high-frequency (typically, 30 minute) imagery collected over several years, the GCC (green chromatic  
553 coordinate) time series of a region-of-interest (ROI) that delineates an area of specific vegetation type  
554 was provided by the PhenoCam dataset. The VCI (vegetation contrast index) time series was calculated  
555 as the ratio of the green to the sum of the red and blue bands (Zhang *et al.*, 2018). For the comparison  
556 between satellite  $D_{LCO}$  and  $D_{LCO}$  from the PhenoCam dataset, processing steps are as follows:

557 Step 1, the sites for agricultural lands, urban areas, or heterogeneous landscape within the area of  
558 a 500 m × 500 m pixel were excluded by visually examining the images in Google Earth. Then, daily  
559 time series were created by calculating the 90th percentile of GCC or VCI for each day. After that, 5-day  
560 medium value filtering was used to smooth the short term fluctuations and noises.

561 Step 2, a time series was excluded if there was no data in any consecutive 30 days from annual  
562 maximum and to the end of year.

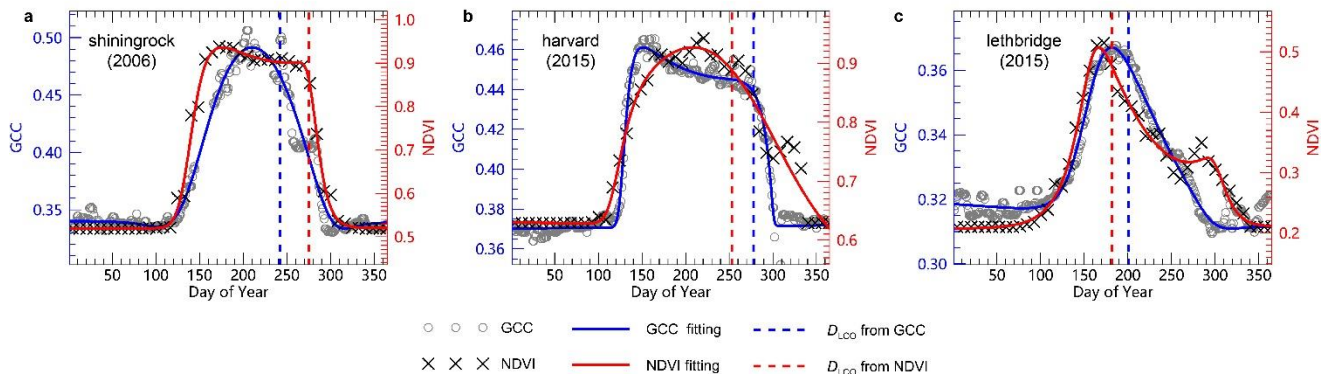
563 Step 3, the annual time series were fitted to a generalized sigmoid function (eq 7 in Klosterman et  
564 al (Klosterman *et al.*, 2014)).

565 Step 4, in many of the sites, there was considerable mismatch between the annual NDVI and GCC  
566 (or VCI) trajectories. To remove some of those mismatched annual trajectories, we excluded the site-  
567 years for which the date of annual maximum NDVI differed by more than 30 days from that of GCC (or  
568 VCI) or the Pearson's correlation coefficient between NDVI and GCC (or VCI) lower than 0.75. In this  
569 step, the date of annual maximum NDVI (or GCC, VCI) was determined using 25-day smoothed times  
570 series of the fitted curves to eliminate short time variations. The Pearson's correlation coefficient was  
571 calculated between fitted daily NDVI and GCC (or VCI) for the period from the date of annual  
572 maximum greenness and the date when greenness dropped by 60%. The period for calculating  
573 correlation coefficient was determined using the earlier one of the dates of annual maximum NDVI and  
574 GCC (or VCI) and the later one of the dates when NDVI and GCC (or VCI) dropped by 60%. This  
575 criterion was not applied to deciduous broadleaf forest, because annual maximum of GCC or VCI  
576 usually occurred in late May or early June whereas annual maximum of NDVI was usually in late July  
577 or early August. After that, we excluded the annual NDVI time series for which the mean NDVI of the

578 31 days period with annual maximum NDVI in the 16<sup>th</sup> day was less than 1.15 times the mean NDVI of  
579 December.

580 The satellite  $D_{LCO}$  explained about 80% of the variations in PhenoCam derived  $D_{LCO}$  (Fig. 2 in the  
581 main text), although the mismatch between the annual NDVI and GCC trajectories leads to large  $D_{LCO}$   
582 difference between NDVI and GCC (Figure SM6) or VCI (Figure SM7).

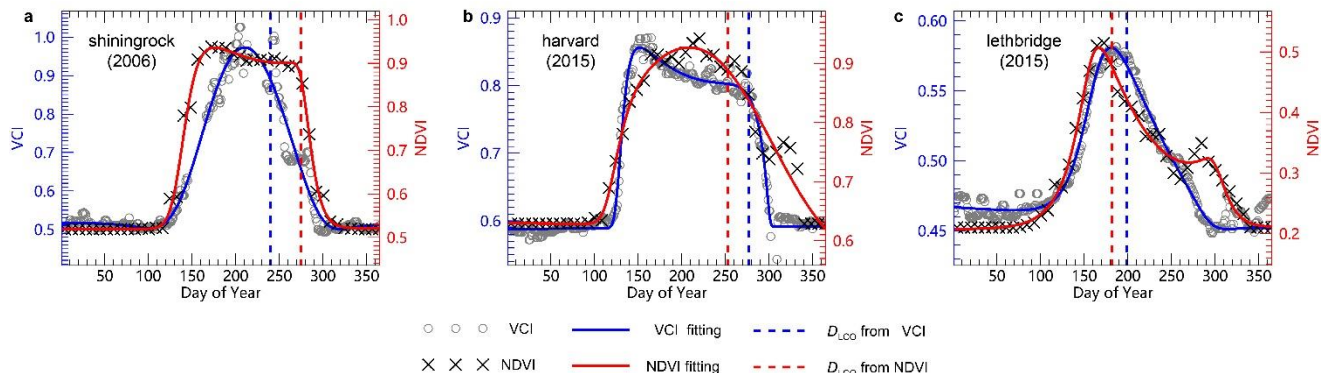
583



584

585 **Figure SM6.** Examples that mismatch between the annual NDVI and GCC trajectories leads to large  
586  $D_{LCO}$  difference between NDVI and GCC.

587



588

589 **Figure SM7.** Examples that mismatch between the annual NDVI and VCI trajectories leads to large  
590  $D_{LCO}$  difference between NDVI and VCI.

591

592

593      **Supplementary References**

- 594      Aikio, S., Taulavuori, K., Hurskainen, S., Taulavuori, E. & Tuomi, J. (2019) Contributions of day  
595      length, temperature and individual variability on the rate and timing of leaf senescence  
596      in the common lilac *Syringa vulgaris*. *Tree Physiology*, **39**, 961-970.
- 597      Amiro, B. (2016) FLUXNET2015 CA-Man Manitoba - Northern Old Black Spruce (former  
598      BOREAS Northern Study Area). In. FluxNet; University of Manitoba
- 599      Arain, M.A. (2016a) FLUXNET2015 CA-TP4 Ontario - Turkey Point 1939 Plantation White  
600      Pine. In. FluxNet; McMaster University
- 601      Arain, M.A. (2016b) FLUXNET2015 CA-TP3 Ontario - Turkey Point 1974 Plantation White  
602      Pine. In. FluxNet; McMaster University
- 603      Aurela, M., Tuovinen, J.-P., Hatakka, J., Lohila, A., Mäkelä, T., Rainne, J. & Lauria, T. (2016)  
604      FLUXNET2015 FI-Sod Sodankyla. In. FluxNet; Finnish Meteorological Institute
- 605      Beck, P.S.A., Atzberger, C., Høgda, K.A., Johansen, B. & Skidmore, A.K. (2006) Improved  
606      monitoring of vegetation dynamics at very high latitudes: A new method using MODIS  
607      NDVI. *Remote Sensing of Environment*, **100**, 321-334.
- 608      Bernhofer, C., Grünwald, T., Moderow, U., Hehn, M., Eichelmann, U. & Prasse, H. (2016a)  
609      FLUXNET2015 DE-Tha Tharandt. In. FluxNet; TU Dresden
- 610      Bernhofer, C., Grünwald, T., Moderow, U., Hehn, M., Eichelmann, U. & Prasse, H. (2016b)  
611      FLUXNET2015 DE-Gri Grillenburg. In. FluxNet; TU Dresden
- 612      Berveiller, D., Delpierre, N., Dufrêne, E., Pontailler, J.-Y., Vanbostal, L., Janvier, B., Mottet, L. &  
613      Cristinacce, K. (2016) FLUXNET2015 FR-Fon Fontainebleau-Barbeau. In. FluxNet;  
614      CNRS
- 615      Black, T.A. (2016a) FLUXNET2015 CA-Obs Saskatchewan - Western Boreal, Mature Black  
616      Spruce. In. FluxNet; The University of British Columbia
- 617      Black, T.A. (2016b) FLUXNET2015 CA-Oas Saskatchewan - Western Boreal, Mature Aspen.  
618      In. FluxNet; The University of British Columbia
- 619      Blanken, P. (2016) FLUXNET2015 US-NR1 Niwot Ridge Forest (LTER NWT1). In. FluxNet;  
620      University of Colorado
- 621      Böhlenius, H., Huang, T., Charbonnel-Campaa, L., Brunner, A.M., Jansson, S., Strauss, S.H. &  
622      Nilsson, O. (2006) CO/FT regulatory module controls timing of flowering and seasonal  
623      growth cessation in trees. *Science*, **312**, 1040-1043.
- 624      Cao, R., Chen, Y., Shen, M., Chen, J., Zhou, J., Wang, C. & Yang, W. (2018) A simple method  
625      to improve the quality of NDVI time-series data by integrating spatiotemporal  
626      information with the Savitzky-Golay filter. *Remote Sensing of Environment*, **217**, 244-  
627      257.
- 628      Chen, J. (2016) FLUXNET2015 US-Oho Oak Openings. In. FluxNet; University of Toledo /  
629      Michigan State University
- 630      Davidson, H. (1957) *Photoperiodic responses on selected woody ornamental shrubs*. Michigan  
631      State University of Agriculture and Applied Science. Department of Horticulture,
- 632      De Ligne, A., Manise, T., Heinesch, B., Aubinet, M. & Vincke, C. (2016) FLUXNET2015 BE-Vie  
633      Vielsalm. In. FluxNet; University of Liege - Gembloux Agro-Bio Tech; University catholic  
634      of Louvain-la-Neuve
- 635      Desai, A. (2016) FLUXNET2015 US-PFa Park Falls/WLEF. In. FluxNet; University of  
636      Wisconsin
- 637      Dolman, H., Van Der Molen, M., Parmentier, F.-J., Marchesini, L.B., Dean, J., Van Huissteden,  
638      K. & Maximov, T. (2016) FLUXNET2015 RU-Cok Chokurdakh. In. FluxNet; Vrije

- 639 Universiteit Amsterdam  
640 Downs, R.J. & Borthwick, H.A. (1956) Effects of photoperiod on growth of trees. *Botanical*  
641 *Gazette*, **117**, 310-326.  
642 Elmore, A.J., Guinn, S.M., Minsley, B.J. & Richardson, A.D. (2012) Landscape controls on the  
643 timing of spring, autumn, and growing season length in mid-Atlantic forests. *Global*  
644 *Change Biology*, **18**, 656-674.  
645 Fennell, A. & Hoover, E. (1991) Photoperiod influences growth, bud dormancy, and cold  
646 acclimation in *Vitis labruscana* and *V. riparia*. *Journal of the American Society for*  
647 *Horticultural Science. American Society for Horticultural Science*, **116**, 270-273.  
648 Fracheboud, Y., Luquez, V., Björkén, L., Sjödin, A., Tuominen, H. & Jansson, S. (2009) The  
649 control of autumn senescence in European aspen. *Plant Physiology*, **149**, 1982-1991.  
650 Gianelle, D., Cavagna, M., Zampedri, R. & Marcolla, B. (2016a) FLUXNET2015 IT-MBo Monte  
651 Bondone. In. FluxNet; Edmund Mach Foundation  
652 Gianelle, D., Zampedri, R., Cavagna, M. & Sottocornola, M. (2016b) FLUXNET2015 IT-Lav  
653 Lavarone. In. FluxNet; Edmund Mach Foundation  
654 Gough, C., Bohrer, G. & Curtis, P. (2016) FLUXNET2015 US-UMB Univ. of Mich. Biological  
655 Station. In. FluxNet; Ohio State University; Virginia Commonwealth University  
656 Grubbs, F.E. (1950) Sample criteria for testing outlying observations. *Annals of Mathematical*  
657 *Statistics*, **21**, 27-58.  
658 Hamilton, J.A., El, K.W., Hart, A.T., Runcie, D.E., Arango-Velez, A. & Cooke, J.E. (2016) The  
659 joint influence of photoperiod and temperature during growth cessation and  
660 development of dormancy in white spruce (*Picea glauca*). *Tree Physiology*, **36**, tpw061.  
661 Heide, O.M. (1974) Growth and Dormancy in Norway Spruce Ecotypes (*Picea abies*) I.  
662 Interaction of Photoperiod and Temperature. *Physiologia Plantarum*, **30**, 1-12.  
663 Heide, O.M. (2001) Photoperiodic control of dormancy in *Sedum telephium* and some other  
664 herbaceous perennial plants. *Physiologia Plantarum*, **113**, 332-337.  
665 Hörttnagl, L., Eugster, W., Buchmann, N., Paul-Limoges, E., Etzold, S. & Haeni, M. (2016a)  
666 FLUXNET2015 CH-Lae Laegern. In. FluxNet; ETH Zurich  
667 Hörttnagl, L., Eugster, W., Merbold, L., Buchmann, N., Etzold, S., Haesler, R. & Haeni, M.  
668 (2016b) FLUXNET2015 CH-Dav Davos. In. FluxNet; ETH Zurich  
669 Howe, G.T., Gardner GHackett, W.P. & Fournier, G.R. (1996) Phytochrome control of short-day-  
670 induced bud set in black cottonwood. *Physiologia Plantarum*, **97**, 95-103.  
671 Ibrom, A. & Pilegaard, K. (2016) FLUXNET2015 DK-Sor Soroe. In. FluxNet; Technical  
672 University of Denmark (DTU)  
673 Janssens, I. (2016) FLUXNET2015 BE-Bra Brasschaat. In. FluxNet; University of Antwerp  
674 Juntila, O. (1980) Effect of photoperiod and temperature on apical growth cessation in two  
675 ecotypes of *Salix* and *Betula*. *Physiologia Plantarum*, **48**, 347-352.  
676 Keskitalo, J., Bergquist, G., Gardeström, P. & Jansson, S. (2005) A cellular timetable of autumn  
677 senescence. *Plant Physiol*, **139**, 1635-1648.  
678 Klosterman, S.T., Hufkens, K., Gray, J.M., Melaas, E., Sonnentag, O., Lavine, I., Mitchell, L.,  
679 Norman, R., Friedl, M.A. & Richardson, A.D. (2014) Evaluating remote sensing of  
680 deciduous forest phenology at multiple spatial scales using PhenoCam imagery.  
681 *Biogeosciences*, **11**, 4305-4320.  
682 Knohl, A., Tiedemann, F., Kolle, O., Schulze, E.-D., Kutsch, W., Herbst, M. & Siebicke, L.  
683 (2016) FLUXNET2015 DE-Hai Hainich. In. FluxNet; University of Goettingen,  
684 Bioclimatology

- 685 Kramer, P.J. (1936) Effect of variation in length of day on growth and dormancy of trees. *Plant*  
686 *Physiology*, **11**, 127-137.
- 687 Law, B. (2016) FLUXNET2015 US-Me2 Metolius mature ponderosa pine. In. FluxNet; Oregon  
688 State University
- 689 Lund, M., Jackowicz-Korczynski, M. & Abermann, J. (2016) FLUXNET2015 DK-ZaH  
690 Zackenberg Heath. In. FluxNet; Aarhus University
- 691 Mammarella, I., Vesala, T., Keronen, P., Kolari, P., Launiainen, S., Pumpanen, J., Rannik, Ü.,  
692 Siivola, E., Levula, J. & Pohja, T. (2016) FLUXNET2015 FI-Hyy Hyytiala. In. FluxNet;  
693 University of Helsinki
- 694 Massman, B. (2016) FLUXNET2015 US-GLE GLEES. In. FluxNet; USDA Forest Service
- 695 Matteucci, G. (2016) FLUXNET2015 IT-Col Collelongo. In. FluxNet; Istituto di Ecologia e  
696 Idrologia Forestale CNR
- 697 McCaughey, H. (2016) FLUXNET2015 CA-Gro Ontario - Groundhog River, Boreal Mixedwood  
698 Forest. In. FluxNet; Queen's University
- 699 Minerbi, S. & Montagnani, L. (2016) FLUXNET2015 IT-Ren Renon. In. FluxNet; Autonomous  
700 Province of Bolzano, Forest Services
- 701 Misra, G. & Biswal, U.C. (1973) Factors Concerned in Leaf Senescence. I. Effects of Age,  
702 Chemicals, Petiole, and Photoperiod on Senescence in Detached Leaves of Hibiscus  
703 rosa-sinensis L. *Botanical Gazette*, **134**, 5-11.
- 704 Moors, E. & Elbers, J. (2016) FLUXNET2015 NL-Loo Loobos. In. FluxNet; ALTERRA /  
705 Wageningen Environmental Research
- 706 Munger, J.W. (2016) FLUXNET2015 US-Ha1 Harvard Forest EMS Tower (HFR1). In. FluxNet;  
707 Harvard University
- 708 Novick, K. & Phillips, R. (2016) FLUXNET2015 US-MMS Morgan Monroe State Forest. In.  
709 FluxNet; Indiana University
- 710 Oleksyn, J., Tjoelker, M.G. & Reich, P.B. (1992) Growth and biomass partitioning of  
711 populations of European Pinus sylvestris L. under simulated 50° and 60°N daylengths:  
712 evidence for photoperiodic ecotypes. *New Phytologist*, **120**, 561-574.
- 713 Olmsted, C.E. (1951) Experiments on Photoperiodism, Dormancy, and Leaf Age and  
714 Abscission in Sugar Maple. *Botanical Gazette*, **112**, 365-393.
- 715 Paus, E., Nilsen, J. & Junntila, O. (1986) Bud dormancy and vegetative growth in Salix-Polaris  
716 as affected by temperature and photoperiod. *Polar Biology*, **6**, 91-95.
- 717 Rinne, P., Saarelainen, A. & Junntila, O. (1994) Growth cessation and bud dormancy in relation  
718 to ABA level in seedlings and coppice shoots of Betula pubescens as affected by a short  
719 photoperiod, water stress and chilling. *Physiologia Plantarum*, **90**, 451-458.
- 720 Scott, R. (2016a) FLUXNET2015 US-SRM Santa Rita Mesquite. In. FluxNet; United States  
721 Department of Agriculture
- 722 Scott, R. (2016b) FLUXNET2015 US-Wkg Walnut Gulch Kendall Grasslands. In. FluxNet;  
723 United States Department of Agriculture
- 724 Shen, M., Zhang, G., Cong, N., Wang, S., Kong, W. & Piao, S. (2014) Increasing altitudinal  
725 gradient of spring vegetation phenology during the last decade on the Qinghai-Tibetan  
726 Plateau. *Agricultural and Forest Meteorology*, **189-190**, 71-80.
- 727 Šigut, L., Havrankova, K., Jocher, G., Pavelka, M. & Janouš, D. (2016) FLUXNET2015 CZ-BK1  
728 Bily Kriz forest. In. FluxNet; Global Change Research Institute CAS
- 729 Varlagin, A., Kurbatova, J. & Vygodskaya, N. (2016) FLUXNET2015 RU-Fyo Fyodorovskoye.  
730 In. FluxNet; A.N. Severtsov Institute of Ecology and Evolution

- 731 Vermote, E.F. (2015) MOD09CMG MODIS/Terra Surface Reflectance Daily L3 Global 0.05Deg  
732 CMG V006. In: *NASA EOSDIS Land Processes DAAC*
- 733 Vermote, E.F., Roger, J.C. & Ray, J.P. (2015) MODIS Surface Reflectance User's Guide,  
734 Collection 6, Version 1.4. *MODIS Land Surface Reflectance Science Computing*  
735 *Facility*,
- 736 Wang, D.Y., Hu, S., Li, Q., Cui, K.M. & Zhu, Y.X. (2002) Photoperiod control of apical bud and  
737 leaf senescence in pumpkin (*Cucurbita pepo*) strain 185. *Acta Botanica Sinica*, **44**, 55-  
738 62.
- 739 Wilson, A.M., Parmentier, B. & Jetz, W. (2014) Systematic land cover bias in Collection 5  
740 MODIS cloud mask and derived products — A global overview. *Remote Sensing of*  
741 *Environment*, **141**, 149-154.
- 742 Zhang, X. (2015) Reconstruction of a complete global time series of daily vegetation index  
743 trajectory from long-term AVHRR data. *Remote Sensing of Environment*, **156**, 457-472.
- 744 Zhang, X., Jayavelu, S., Liu, L., Friedl, M.A., Henebry, G.M., Liu, Y., Schaaf, C.B., Richardson,  
745 A.D. & Gray, J. (2018) Evaluation of land surface phenology from VIIRS data using time  
746 series of PhenoCam imagery. *Agricultural and Forest Meteorology*, **256-257**, 137-149.  
747